Microscopic Modeling of Novel Semiconductor Heterostructure Properties

Dissertation
zur
Erlangung des Doktorgrades
der Naturwissenschaften
(Dr. rer. nat.)

dem Fachbereich Physik
der Philipps-Universität Marburg
vorgelegt

von
Maria Josephine Weseloh

aus Hamburg

Marburg (Lahn), 2020

Vom Fachbereich Physik der Philipps-Universität Marburg
als Dissertation angenommen am 09.09.2020

Hochschulkennziffer: 1180

Erstgutachter: Prof. Dr. Stephan W. Koch
Zweitgutachter: Prof. Dr. Ralf Tonner

Tag der mündlichen Prüfung: 18.09.2020

Abstract

Nowadays, semiconductor-based technology is part of everyday lives of many people around the world. This is most visible in the frequent use of computers and smartphones. By using clouds, messenger services and social networks among other things, enormous amounts of data are transmitted globally. For this purpose, laser signals that propagate through fiber-optic cables are being used. At this, the wavelengths that can be used for transmission, are determined by the absorption and dispersion properties of the propagation medium [[1]]. Wavelengths in the near-infrared range of the electromagnetic spectrum are suited for this purpose.
Conventional light-emitting heterostructures that consist of nanometer-thick semiconductor layers and rely on spatially direct recombination of charge carriers in the same layer, are not ideally suited for emission in the near-infrared. This stems from Auger-losses, which increase with increasing wavelength and are significant for bandgap energies corresponding to wavelengths in the near-infrared [[2]]. Furthermore, Auger-losses increase with the charge carrier density and temperature. Hence, alternatives are needed.
Promising alternatives are provided by heterostructures that rely on spatially indirect recombination of charge carriers [[3]]. In such heterostructures, electrons and holes are confined in layers of different semiconductor materials. This allows to use semiconductor materials with comparatively large bandgaps and to still generate light with a wavelength in the near-infrared of the electromagnetic spectrum. Moreover, using two different materials for charge carrier confinement increases the number of possible designs for such structures and thus offers more flexibility.
Generally, the confinement of electrons and holes in different semiconductor layers is accompanied by lowered electron-hole wavefunction overlap in comparison to structures that rely on spatially direct charge carrier recombinations. This leads to lowered optical transition rates and can be compensated to a certain extent by careful optimization of the optical properties of these heterostructures.

This thesis presents research results that contribute to the optimization of heterostructures that rely on spatially indirect recombination of electrons and holes. For this purpose, it was focused on heterostructures where (InGa)As was used to achieve electron confinement and Ga(AsSb) was used to achieve hole confinement. At this, both materials were grown on GaAs as a substrate. Using GaAs based heterostructures allows one to use mature (AlGa)As/GaAs-distributed Bragg reflector technologies when building specific laser devices [[4]].

The results presented in this thesis are either based on calculations using the reliable many-body theory from the semiconductor Bloch and luminescence equations in combination with the **k**·**p**-theory or on density functional theory calculations. In many respects, the results gained from the calculations replace the investigative, experimental growth and subsequent experimental characterization of properties of such heterostructures. In the investigated heterostructures, charge transfer and recombination processes take place through internal interfaces. Properties of the internal interfaces can be studied using interface specific excitations. One of those is the charge-transfer exciton. This thesis presents certain results from a detailed experiment-theory investigation of the formation and decay of charge transfer excitons. The presented results are based on bandstructure calculations with the **k**·**p**-theory and the semiconductor Bloch approach.

The density functional theory calculations carried out in the framework of this thesis were used to calculate the valence band offsets between GaAs and Ga(AsSb) in strained heterostructures. This allows for drawing conclusions on the band alignment in the corresponding heterostructure. Moreover, for certain experimentally grown heterostructures, the band alignment between GaAs and Ga(AsSb) was deduced by comparing experimental results to the ones calculated with the semiconductor luminescence equations and the **k**·**p**-theory. While these results and the obtained valence band offsets are restricted to the investigated heterostructures, the valence band offsets calculated with density functional theory are not restricted to certain heterostructures. During the density functional calculations the problem appeared that the Ga(AsSb) bandgaps vanish at certain Sb concentrations in the ternary semiconductor compound. Related to this, for Sb concentrations exceeding a critical value the calculated valence band offsets diverged. These problems could be resolved by introducing the method of half-occupations [[5, 6]] to the calculations of the valence band offsets. The presented approach for the calculation of valence band offsets has the potential to be applicable for other semiconductor materials as well.

Zusammenfassung

Heutzutage gehört halbleiterbasierte Technologie weltweit zum Alltag vieler Menschen. Am sichtbarsten ist dies durch die scheinbar allgegenwärtige Nutzung von Handys und Computern. Unter anderem durch die Nutzung von Clouds, Messenger Diensten und sozialen Netzwerken werden global enorme Mengen an Daten verschickt. Übertragen werden diese Daten mittels Elektromagnetischer Wellen. Hierzu werden Lasersignale genutzt, die durch Glasfaserkabel propagieren. Dabei werden durch die Absorptions- und Dispersionseigenschaften des genutzten Propagationsmediums die zur Übertragung praktisch nutzbaren Wellenlängen festgelegt [[1]]. Gut geeignet sind hierbei Wellenlängen aus dem nahem Infrarot des elektromagnetischen Spektrums.
In konventionellen Halbleiterheterostrukturen, welche aus nanometerdicken Schichten verschiedener Halbleitermaterialien bestehen und auf der räumlich direkten strahlenden Rekombination von Ladungsträgern basieren, nehmen Auger-Verluste mit größer werdenden Wellenlängen zu und sind im Nah-Infrarotem betrachtlich [[2]]. Hinzu kommt, dass diese Verluste mit höher werdender Ladunsgträgerdichte und Tempertur zunehmen. Insgesamt limitieren Auger-Verluste somit die praktische Verwendbarkeit solcher Heterostrukturen. Deshalb sind alternative Heterostruktur Layouts für eine effiziente Emission mit Wellenlängen im nahem Infrarot vonnöten.
Vielversprechend sind hierbei Layouts, die die räumlich indirekte strahlende Rekombination von Ladungsträgern nutzen. In solchen Heterostrukturen sind die Elektronen und Löcher vor der Rekombination in unterschiedlichen Halbleiterschichten eingeschlossen, im Gegensatz zu erstgenannten Heterostrukturen, in denen Elektronen und Löcher vor der Rekombination in der gleichen Halbleiterschicht eingeschlossen sind. Dies ermöglicht die Verwendung von Halbleitermaterialien mit relativ großen Bandlücken, mit denen dennoch durch die räumlich indirekte Rekombination in der Heterostruktur Licht im Nah-Infraroten Bereich des elektromagnetischen Spektrums erzeugt wird. Die Verwendung zweier Materialien für den Landungsträgereinschluss

vergrößert die Anzahl an möglichen Gestaltungen solcher Strukturen und bietet somit mehr Flexibilität.
Nachteilig ist jedoch, dass bei solchen Heterostrukturen der durch die räumliche Trennung verringerte Wellenfunktionsüberlapp von Elektronen und Löchern, im Vergleich zu Heterostrukturen die eine räumlich direkte Rekombination von Ladungsträgern verwenden, die Wahrscheinlichkeit einer Rekombination von Elektronen und Löchern verringert. Dies kann jedoch durch die sorgfältige Optimierung der optischen Eigenschaften solcher Heterostrukturen in einem gewissen Rahmen kompensiert werden.
Diese Dissertation präsentiert Forschung, die ihren Beitrag zur Optimierung der optischen Eigenschaften von Heterostrukturen mit räumlich indirekter Ladungsträger Rekombination leistet. Dabei wurde sich bei den Schichten, in die die Löcher und Elektronen vor ihrer Rekombination relaxieren, auf die ternären Halbleiter Ga(AsSb) und (InGa)As konzentriert, welche auf GaAs gewachsen sind. Hier besteht der Vorteil, dass man für auf GaAs gewachsene lichtemittierende Schichten beim Fabrizieren eines Lasers auf ausgereifte (AlGa)As/GaAs-Bragg Spiegel-Technologien zurückgreifen kann [[4]].
Konkret wurden mit der vielfach bewährten mikroskopischen Vielteilchentheorie der Halbleiter-Bloch- und Halbleiter-Lumineszenz-Gleichungen kombiniert mit der **k·p**-Theorie bestimmte optische und elektronische Eigenschaften sowie die Potentiallandschaft solcher Heterostrukturen vorhergesagt und charakterisiert. Darüber hinaus wurde auch mithilfe von Dichtefunktionaltheorie die für den Ladungsträgereinschluss wichtige Potentiallandschaft in solchen Heterostrukturen untersucht. Die durch die Berechnungen gewonnenen Erkenntnisse ersetzen in vielerlei Hinsicht das investigative, experimentelle Wachstum und die nachfolgende Charakterisierung von Eigenschaften solcher Heterostrukturen.
Für die räumlich indirekte Rekombination der Ladungsträger sind des Weiteren auch Eigenschaften der internen Grenzflächen, durch die Ladungstransfer und Rekombination geschehen, maßgeblich für die Performanz der Laserstrukturen. Im Hinblick auf den Einfluss der internen Grenzfläche wurden die Entstehung und der Zerfall von Ladungstransfer-Exzitonen als grenzflächenspezifische Anregungen experimentell und mittels des Halbleiter-Bloch-Ansatzes in Verbindung mit **k·p**-theoretischen Berechnungen detailliert untersucht. Diese Dissertation präsentiert Ergebnisse aus dieser Studie, die in direkter Verbindung zur Berechnung der elektronischen Bandstruktur der vermessenen Heterostruktur und Absorptionseigenschaften der Ladungsträger und insbesondere der Ladungstransfer-Exzitonen stehen.
Die oben bereits erwähnten Dichtefunktionaltheorie-Berechnungen ermöglichten die Berechnung von Valenzbandoffsets zwischen verspannten Schich-

ten von Ga(AsSb) zu GaAs gänzlich ohne experimentellen Input. Mit den erhaltenen Valenzbandoffsets ist es möglich, Rückschlüße auf die Anordnung der Leitungsbandminima-Energien zwischen Ga(AsSb)- und GaAs-Schichten in Heterostrukturen zu ziehen. Dies wird in der Fachliteratur kontrovers diskutiert (siehe [[7]] und Referenzen hierein). Bei den Berechnungen verschwand jedoch bei bestimmten Sb Konzentrationen im ternären Halbleiter die Bandlücke und es war hier keine verlässliche Bestimmung der Valenzbandoffsets möglich. Beide Probleme konnten durch Einbeziehen der Methode der halben Besetzungen [[5, 6]], welche auf Slater und Johnsons $X\alpha$-Methode [[8]] basiert, behoben werden. Die so erprobte Methodik der Valenzbandoffset Berechnung hat das Potential, auch für andere Halbleitermaterialien anwendbar zu sein.

Danksagung

Ich bedanke mich herzlich bei allen bei allen die zum Gelingen dieser Arbeit beigetragen haben. An erster Stelle möchte ich mich herzlich bei Prof. Dr. Stephan Koch bedanken, der es mir ermöglichte als Teil seiner Arbeitsgruppe an spannenden Themen zu forschen. Auch danke ich Stephan Koch für seine stets gute Betreuung. Als Teil seiner Arbeitsgruppe war mit stets bewusst, dass ich mit Stephan Koch einen hoch-kompetenten Arbeitsgruppenleiter als Ansprechpartner habe.
Mein herzlicher Dank geht auch an Prof. Dr. Wolfgang Stolz, der die fruchtbare Zusammenarbeit seiner und unserer Arbeitsgruppe im Projekt B7 des SFB 1083 prägte.
Mein besonderer Dank gilt auch Prof. Dr. Ralf Tonner für die Übernahme der Rolle Zweitgutachters meiner Dissertation. Ebenso bedanke ich mich vielmals bei Prof. Dr. Florian Gebhard, der mir aus meiner Diplomzeit in guter Erinnerung bleiben wird, dafür dass er ein Teil der Prüfungskomission bei meiner Disputation ist.
Auch möchte ich Prof. Dr. Kerstin Volz und ihren Forschern für die Zusammenarbeit im Rahmen des SFB 1083 vielmals danken. Ich bedanke mich bei Allen, mit denen ich im Rahmen des SFB 1083 im Projekt B7 direkt zusammen gearbeitet habe. Allen voran bedanke ich mich bei Dr. Christian Berger, der mich mit der Forschung zum “W”-Laser bekannt machte. Auch möchte ich mich bei Dr. Christian Fuchs und Dr. Christoph Möller für die Zusammenarbeit, die gemeinsame Planung von Projekten und das Herstellen von Heterostrukturen und Lasern vielmals bedanken.
Besonderer Dank gebührt auch Dr. Jan Oliver Oelerich für eine ausgezeichnete Zusammenarbeit und Dr. Lars Bannow für das etablieren der Dichtefunktionaltheorie in unserer Arbeitsgruppe und für die hilfreichen Diskussionen zu verschiedenen Themen. Ebenfalls bedanke ich mich bei Dr. Phil Rosenow, der Lars Bannow mit der Dichtefunktionaltheorie bekannt machte und der stets ein guter Ansprechpartner für Fragen zur Dichtefunktionaltheorie war.

Zudem bedanke ich mich bei Dr. Sebastian Gies und Dr. Osmo Vänskä für die angenehme Zusammenarbeit die zu gemeinsamen Publikationen führte. Nicht minder bedanke ich mich bei der gesamten Arbeitsgruppe, inklusive ehemaliger Mitglieder, für die stets gute Gesellschaft. Insbesondere bedanke ich mich bei Dr. Osmo Vänskä und Dr. Peter Hawkins die ich sogar in Helsinki und Leeds besuchen durfte.
Mehr als danken möchte ich mich bei meinem Mann Christian Herianto, der als Wichtigstes in meinem Leben unentbehrlich ist und mich stets bestärkt.

Author's contributions

This thesis presents research results from my doctoral studies. These results contributed to the following publications.

Publications in peer-reviewed journals

2016: *Electrical injection type-II (GaIn)As/Ga AsSb)/(GaIn)As single "W"-quantum well laser at 1.2 μm*, C. Fuchs, C. Berger, C. Möller, M. Weseloh, S. Reinhard, J. Hader, J.V. Moloney, S.W. Koch, and W. Stolz, Electr. Lett. **52** (2016) 22 1875, http://mr.crossref.org/iPage?doi=10.1049%2Fel.2016.2851.

2016: *Band offset in (Ga,In)As/Ga(As,Sb) heterostructures*, S. Gies, M. J. Weseloh, C. Fuchs, W. Stolz, J. Hader, J. V. Moloney, S. W. Koch, and W. Heimbrodt, J. Appl. Phys. **120** (2016) 204303, https://aip.scitation.org/doi/10.1063/1.4968541.

2017: *Atomic structure of "W"-type quantum well heterostructures investigated by aberration-corrected STEM*, P. Kükelhan, A. Beyer, C. Fuchs, M. J. Weseloh, S. W. Koch, W. Stolz, and K. Volz, J. Microsc. **268** (2017) 259-268, https://onlinelibrary.wiley.com/doi/full/10.1111/jmi.12647. (Not discussed in the framework of this thesis.)

2018: *Dynamics of charge-transfer excitons in type-II semiconductor heterostructures*, M. Stein, C. Lammers, P.-H. Richter, C. Fuchs, W. Stolz, M. Koch, O. Vänskä, M. J. Weseloh, M. Kira, and S.W. Koch, Phys. Rev. B **97** (2018) 125306, https://journals.aps.org/prb/abstract/10.1103/PhysRevB.97.125306.

2018: *High-temperature operation of electrical injection type-II (GaIn)As/Ga(AsSb)/(GaIn)As "W"-quantum well lasers emitting at 1.3 μm*, C. Fuchs, A. Brüggemann, M. J. Weseloh, C. Berger,

C. Möller, S. Reinhard, J. Hader, J.V. Moloney, A. Bäumner, S.W. Koch, and W. Stolz, Sci. Rep. **8** (2018) 1422, https://www.nature.com/articles/s41598-018-19189-1.

2019: *Ab-initio calculation of band alignments for opto-electronic simulations*, J. O. Oelerich, M. J. Weseloh, K. Volz, and S. W. Koch, AIP Adv. **9** (2019) 055328, https://aip.scitation.org/doi/10.1063/1.5087756.

2020: *Half-occupation approach for the ab initio calculation of strained Ga(AsSb)/GaAs valence band offsets*, M. J. Weseloh, J. O. Oelerich, and S. W. Koch, AIP Adv. **10** (2020) 045207, https://doi.org/10.1063/5.0001300.

Posters and talks

- **C. Berger, M. J. Weseloh,** C. Möller, C. Fuchs, A. Ruiz Perez, J. Hader, J. V. Moloney, N. W. Rosemann, J. Valetas, S. Chatterjee, W. Heimbrodt, W. Stolz, and S. W. Koch, *Type-II quantum well structures for interface dominated lasers*, Poster presented at the ICII-2016 International Conference on Internal Interfaces in Marburg, Germany (2016).

- **M. J. Weseloh,** C. Berger, C. Möller, C. Fuchs, A. Ruiz Perez, J. Hader, J. V. Moloney, N. W. Rosemann, J. Valetas, S. Chatterjee, W. Heimbrodt, W. Stolz, and S. W. Koch, *Type-II quantum well structures for interface dominated lasers*, Poster presented at the Visit of the Young Research Delegation from India and Thailand in Marburg, Germany (2016).

- **M. J. Weseloh,** C. Berger, C. Möller, C. Fuchs, J. Hader, J. V. Moloney, W. Stolz, and S. W. Koch, *Interface-Dominated Semiconductor Laser Structures*, Contributed talk at the SFB 1083 Winter School 2017 in Rauischholzhausen, Germany (2017).

- **M. J. Weseloh,** C. Berger, A. Bäumner, C. Möller, C. Fuchs, S. Gies, P. Kükelhan, A. Beyer, K. Volz, W. Heimbrodt, W. Stolz, and S. W. Koch, *Microscopic Modelling of GaInAs/GaAsSb "W"-Quantum Well Heterostructures*, Poster presented at the Materialforschungstag Mittelhessen 2017 in Gießen, Germany (2017).

- **M. J. Weseloh,** J. O. Olerich, A. Bäumner, C. Fuchs, S. W. Koch, and W. Stolz, *Microscopic Modelling and Theoretical Characterization of GaInAs/GaAsSb "W" Quantum-Well Heterostructures in Semiconductor Quantum-Well Lasers*, Poster presented at the Materialforschungstag Mittelhessen 2018 in Marburg, Germany (2018).

- **M. J. Weseloh,** J. O. Olerich, C. Berger, A. Bäumner, C. Fuchs, C. Möller, A. Brüggemann,, J. Hader, J. V. Moloney, W. Stolz, and S. W. Koch, *Microscopic Modelling of InGaAs/GaAsSb "W"-Laser Structures*, Contributed talk at the GRK & SFB 1083 2nd Joint Seminar in Volkenroda, Germany (2018).

- **M. J. Weseloh,** J. O. Oelerich, L. C. Bannow, A. Bäumner, W. Stolz, K. Volz and S. W. Koch, *Theoretical Investigations on III-V Laser Materials*, Poster presented at Materialforschungstag Mittelhessen 2019 in Gießen, Germany (2019).

Original contributions

The studies presented in this thesis are the result of frequent discussions in group meetings and with research partners and other forms of correspondence with my supervisor S. W. Koch, which altogether led to the planning of the next steps.
My doctoral studies were dedicated to investigations of interface-dominated quantum well laser structures with emission wavelengths in the near-infrared. For this purpose, I used different theoretical approaches to characterize relevant properties of such heterostructures.
Section 3.1 deals with the design of type-II "W"-heterostructures with regards to the optimization of their optical properties. At this, the presented studies benefited from results which C. Berger had already obtained and we had a close cooperation designing 1200 nm "W"-heterostructures.
My first project was devoted to the design of quantum well heterostructures with emission wavelength at 1200 nm. Here, C. Berger and me worked in cooperation with C. Fuchs and C. Möller from the research group of W. Stolz, who experimentally realized the light-emitting structures and measured their optical properties. Calculations of C. Berger and the design studies from Section 3.1.1 that I carried out supported the successful realization of an electrical injection laser with emission wavelength around 1200 nm [[9]].
To allow for strong emission properties, different designs for the light-emitting region were studied and subsequently the emission wavelength was extended

towards an emission wavelength around 1300 nm. Based on the results from my design studies and further calculation of A. Bäumner, an electrical injection laser with emission wavelength around 1300 nm was experimentally realized in the group of W. Stolz.
Section 3.2 presents results from the optical and terahertz characterization of excitons in type-II heterostructures, which have been published in [[10]]. For this publications I contributed with the calculation of the energy levels of the heterostructure, the bandstructure, the confinement wavefunctions and the dipole matrix elements that were needed for further calculations. The main part of the calculations has been carried out by O. Vänskä and M. Stein and C. Lammers carried out the experimental characterization of the excitons. C. Fuchs grew the sample.
Chapter 4 focuses on the band offsets between GaAs and Ga(AsSb), which determine the band alignment of these semiconductors.
In Section 4.1, comparisons of measured Photoluminescence spectra from GaAs, Ga(AsSb) and (InGa)As based heterostructures to the calculated Photoluminescence spectra were used to deduce the band alignment between GaAs and Ga(AsSb) [[11]]. The samples were grown by C. Fuchs, the spectra were measured by S. Gies the research group of W. Heimbrodt and were theoretically calculated by me. Furthermore, I contributed to the paper by writing the theory part.
The studies presented in Section 4.2 result from frequent discussions with J. O. Oelerich, L. C. Bannow and K. Jandieri under supervision of S. W. Koch. The first part of Section 4.2 deals with the method which has been presented in [[12]] and extends the results from the publication. To this publication, I contributed with calculations of the valence band offsets between GaAs and Ga(AsSb) as well as GaAs and (InGa)As. Moreover I carried out Photoluminescence calculations for a heterostructure from Section 4.1 with the valence band offsets from the presented calculations and compared the Photoluminescence to the measured one. I also contributed in writing the related parts of the manuscript.
In the second part of Section 4.2, I modified the VBO calculation to correct erroneous results from the first part of this section. These results have been published in [[13]], where I contributed by performing all presented calculations, writing the manuscript and submitting it.

Contents

Chapter 1

Introduction

Nowadays, large parts of everyday life are influenced by semiconductor-based technologies, like smartphones or computers, and digitalization is continuing to progress. Increasingly, people network via the internet. Moreover, this is currently being reinforced by the pandemic. All this leads to an increasing amount of data which is transferred via fiber-optics. For the transmission of the data, semiconductor lasers are a highly suited light source [[1]]. However, the used lasers must emit at specific wavelengths in the near-infrared region of the electromagnetic spectrum. This stems from the dispersion and transmission properties of the used optical fibers.
In case of established laser structures that rely on the spatially direct recombination of electron-hole pairs, non-radiative recombination processes limit their applicability at these emission wavelengths. Hence, alternatives were needed and research was devoted to heterostructures that rely on the spatially indirect recombination of electron-hole pairs [[2, 3]].
Generally, the spatial separation of electrons and holes results in a reduction of the optical transition probability, resulting in lower output powers (see [[14]] for example). Therefore, further optimization is necessary.
The research presented in this thesis is devoted to the optimization of the optical properties of laser heterostructures that rely on spatially indirect recombination and emit in the near-infrared. The investigations are carried out either by direct calculations of the optical properties of heterostructures or by investigation of properties that are relevant for the indirect recombination. For this purpose, nanometer-thick layers of suited III-V semiconductors grown on GaAs substrates were considered. Such structures are called *quantum well heterostructures*. The growth of GaAs-based laser structures has the advantage that mature growth techniques for (AlGa)As-GaAs

distributed Bragg reflectors are available [[4]]. Moreover, the investigated (InGa)As, Ga(AsSb) and GaAs based laser structures operate at room temperature and do not need to be cooled down to cryogenic temperatures. Large parts of the presented research was dedicated to the investigation of Ga(AsSb)-layers grown on GaAs. The reason for this is that there generally is no consensus on the potential landscape in strained quantum well heterostructures made of these materials.
For the calculation and prediction of the optical properties of these materials the semiconductor Bloch and semiconductor luminescence equations [[15, 16]] in combination with $\mathbf{k}\cdot\mathbf{p}$-calculations were used. In addition to these approaches, density functional theory calculations were used to study the valence band offsets between GaAs and Ga(AsSb) in strained quantum well heterostructures. With the results conclusions can be drawn on the band alignment of these materials in such structures. During the calculations, up from a critical Sb concentration the Kohn Sham-bandgaps of Ga(AsSb) vanished. Connected to this, the valence offset results diverged up from a critical Sb concentration. The problems could be overcome by introducing the half-occupation technique to the calculations.
In the following chapter, the theoretical methods that were used for the results presented in this thesis will be shortly introduced. Chapter 3 presents theoretical and experimental results for light-emitting heterostructures. All presented heterostructures rely on the spatially indirect electron-hole recombination. While the first part of this chapter deals with calculations for the optimization of these heterostructures, the second part investigates an interface specific excitation. The subject of Chapter 4 is the determination of the potential landscape of heterostructures. For this, two fundamentally different approaches were used. Firstly, results from an approach that utilizes the comparison of calculated and experimental spectra are presented. Subsequently, an approach independent of experimental results will be introduced and results are presented. In Chapter 5 the results are summarized and an outlook is given.

Chapter 2

Theoretical framework

A fundamental concept used for the description of the optical and electronic properties of semiconductors is the bandstructure. Among the methods for the calculation of a solid's bandstructure, the two methods used in the framework of this thesis will be briefly introduced in Section 2.1 and Section 2.3. By names, these are the **k·p**-theory and the density functional theory (DFT). In the context of theoretically characterizing quantum well heterostructures, the necessary modifications to the theory from Section 2.1 are briefly introduced in Section 2.2. The possible band alignments in such heterostructures are introduced in this section as well.
The methods from Section 2.1 and Section 2.3 differ significantly in their approach. While the **k·p**-theory represents a perturbative approach which relies on experimental input, DFT is a so-called *ab initio* or *first principles* method which means that no experimental input parameters are required.
However, once the eigenenergies, wavefunctions, dipole matrix elements and coulomb matrix elements of a system have been obtained, these quantities can be used to calculate the system's optical properties. In Section 2.4.1 and Section 2.4.2 the microscopic many-body equations used for the calculation of a quantum well heterostructure's absorption and photoluminescence will be introduced.

2.1 k·p-theory

The motion of an electron in a crystal lattice can be described by the corresponding Schrödinger equation. For a semiconductor, this equation represents a demanding many-body problem and because of this, approximations are used. One of these is the Born-Oppenheimer approximation. In the

Born-Oppenheimer approximation, the motion of the valence electrons is separated from the much slower motion of the ions. Ions are nuclei together with their tightly bound core electrons. This separation is based on the much larger mass of an ion and the resulting considerably slower time scale of its motion. In the sense of a mean-field approach we assume that the impact of the nuclei and the other electrons on any single valence electron can be expressed as an effective periodic lattice potential [[16]]. Under these approximations, the one-electron Schrödinger equation is defined by the action of the Hamiltonian H on the electron's wavefunction $\psi_{n,\mathbf{k}}$:

$$H\psi_{n,\mathbf{k}}\left(\mathbf{r}\right) = \left(\frac{\mathbf{p}^2}{2m_0} + V(\mathbf{r})\right)\psi_{n,\mathbf{k}}(\mathbf{r}) = \epsilon^n_{\mathbf{k}}\,\psi_{n,\mathbf{k}}\left(\mathbf{r}\right)\,. \tag{2.1}$$

H consists of two terms: The first represents the kinetic energy with the particle's momentum $\mathbf{p}$ and the free electron mass m_0, and the second represents the periodic mean-field potential of the lattice felt by the electron. $\mathbf{r}$ is the positional vector in real space and n and $\mathbf{k}$ label the eigenstates parameterized by their energy band n and wavevector (or crystal momentum) $\mathbf{k}$. The electron's wavevector is a vector in the crystal's reciprocal lattice where the primitive cell is called the *Brillouin zone* (see [[16]] for example). The single-particle energy spectrum $\epsilon^n_{\mathbf{k}}$ defines the single-particle bandstructure of the solid. In general, the band energies and eigenstates are also parameterized by their spin quantum number. For simplicity, this is not explicitly addressed in this thesis. For a perfectly periodic solid, Bloch's theorem [[17]] can be used for the description of the electronic wavefunctions:

$$\psi_{n,\mathbf{k}}\left(\mathbf{r}\right) = \frac{e^{i\mathbf{k}\cdot\mathbf{r}}}{L^{3/2}}\,u_{n,\mathbf{k}}\left(\mathbf{r}\right)\,, \tag{2.2}$$

where L is the crystal's length. Thus, the wavefunction of a crystal electron can be represented by a plane wave modulated by a lattice periodic function $u_{n,\mathbf{k}}$.

Solving Eq.(2.1) for solids is in generally highly non-trivial and different approaches have been applied (e.g. [[18, 19]]). One such approach is the mentioned $\mathbf{k}\cdot\mathbf{p}$-theory which is particularly useful in the description of direct semiconductors.

2.1.1 Bulk semiconductors

The basic idea behind $\mathbf{k}\cdot\mathbf{p}$ bandstructure calculations is to use the fact that the bandstructure problem has been solved at a point with high symmetry, $\mathbf{k}_0$, and to calculate the bandstructure in its vicinity with the help of these

solutions. Since the III-V semiconductors considered in this thesis have a direct bandgap located at the Γ-point of the Brillouin zone, the point of high symmetry considered here is exactly this point, $\mathbf{k}_0 = (0, 0, 0)$.
By inserting Eq. (2.2) into Eq. (2.1) and with $\mathbf{p} = -i\hbar\nabla$, Eq. (2.1) can be rearranged to

$$\left(H_0 + \frac{\hbar}{m_0}\,\mathbf{k}\cdot\mathbf{p}\right) u_{n,\mathbf{k}}(\mathbf{r}) = \mathscr{E}^n_{\mathbf{k}} u_{n,\mathbf{k}}(\mathbf{r})\,. \tag{2.3}$$

Here $H_0 = \left(-\frac{\hbar}{2m_0}\,\nabla^2 + V(\mathbf{r})\right)$ and $\mathscr{E}^n_{\mathbf{k}} = \left(\epsilon^n_{\mathbf{k}} - \frac{\hbar^2\mathbf{k}^2}{2m_0}\right)$ has been used.
Eq. (2.3) is the starting point for **k·p**-calculations where the term proportional to $\mathbf{k}\cdot\mathbf{p}$ is treated as a small perturbation.
The eigenstates $u_{n,\mathbf{k}}(\mathbf{r})$ and eigenvalues in the vicinity of $\mathbf{k}_0$ are built by non-degenerate perturbation theory [[16]] and the expansion is performed up to the lowest non-trivial order. Due to parity, the first order energy correction vanishes [[16]]. Hence, for the energy the first non-trivial correction is the second order correction.
For simplicity, in the following, states will be written in Dirac notation $|n\,\mathbf{k}\rangle$, and $\mathbf{k}$ will be dropped from the notation for brevity when $\mathbf{k} = \mathbf{k}_0$. The real space representation of the Bloch-functions is obtained by the scalar product $\langle\mathbf{r}|n\,\mathbf{k}\rangle = u_{n,\mathbf{k}}(\mathbf{r})$.
The energy corrections are:

$$\epsilon^n_{\mathbf{k}} = \epsilon^n_{\mathbf{k}_0} + \frac{\hbar^2k^2}{2m_0} + \frac{\hbar^2}{m_0^2}\sum_{m\neq n}\frac{\left(\mathbf{k}\cdot\langle n|\mathbf{p}|m\rangle\right)\left(\mathbf{k}\cdot\langle m|\mathbf{p}|n\rangle\right)}{\epsilon^n_{\mathbf{k}_0} - \epsilon^m_{\mathbf{k}_0}} + O(\mathbf{k}^3)\,. \tag{2.4}$$

For the states, the first order corrections are non-vanishing:

$$|n\,\mathbf{k}\rangle = |n\rangle + \frac{\hbar}{m_0}\sum_{m\neq n}\frac{\mathbf{k}\cdot\langle m|\mathbf{p}|n\rangle}{\epsilon^n_{\mathbf{k}_0} - \epsilon^m_{\mathbf{k}_0}}\,|m\rangle + O(\mathbf{k}^2) = \sum_m c^{n,m}_{\mathbf{k}}\,|n\rangle + O(\mathbf{k}^2)\,. \tag{2.5}$$

Here the expansion coefficients $c^{n,m}_{\mathbf{k}}$ are given by

$$c^{n,m}_{\mathbf{k}} = \delta_{m,n} + (1-\delta_{m,n})\frac{\hbar}{m_0}\frac{\mathbf{k}\cdot\langle m|\mathbf{p}|n\rangle}{\epsilon^n_{\mathbf{k}_0} - \epsilon^m_{\mathbf{k}_0}}\,|m\rangle\,. \tag{2.6}$$

Since Eqs. (2.4)-(2.6) require knowledge of the bandgap (in the respective denominator) and dipole matrix elements (in the respective numerator), these values are usually obtained from experiments.

The energy dispersion from Eq. (2.4) allows for the introduction of the effective mass [[20]]

$$\frac{1}{m_{eff}} = \frac{1}{m_0} + \frac{2}{m_0^2 \mathbf{k}^2} \sum_{m \neq n} \frac{|\langle n|\mathbf{k}\cdot\mathbf{p}|m\rangle|^2}{\epsilon^n_{\mathbf{k}_0} - \epsilon^m_{\mathbf{k}_0}} + O(\mathbf{k}^3)\,. \tag{2.7}$$

Identifying the effective mass in Eq. (2.4) we can rewrite this equation as

$$\epsilon^n_{\mathbf{k}} = \epsilon^n_{\mathbf{k}_0} + \frac{\hbar^2 \mathbf{k}^2}{2\, m_{eff}}\,. \tag{2.8}$$

Not included in the given brief introduction into $\mathbf{k}\cdot\mathbf{p}$-theory is the case of degeneracy. The topmost valence bands in bulk zincblende semiconductors are degenerate at the Γ-point. In such cases, degenerate perturbation theory needs to be applied, which can be found in various solid state theory textbooks (e.g. [[16, 20]]).
Furthermore, in order to properly describe the bandstructure of bulk zincblende crystals, spin-orbit interaction needs to enter. Spin-orbit interaction leads to a twice spin degenerated spin-orbit split-off valence band [[16]].
Additionally, for zincblende crystals solely taking into account the valence and conduction bands, stemming from the sp3-hybridized orbitals, leads to a positive curvature of the valence bands and thus positive effective masses. This is contrary to experimental findings. Therefore, the influence of other bands need to be taken into account as well.
Luttinger derived a Hamiltonian that solves these problems [[21]] using empirical data. Luttinger introduced the so-called *Luttinger parameters* into this phenomenological Hamiltonian. The Luttinger parameters are connected to the effective masses and ensure correct curvatures of the bands. The lift of degeneracy by spin-orbit interaction is taken into account by the introduction of the spin-orbit split-off energy. This energy is usually taken from experiments.
For the results presented in this thesis, the highest three valence bands and the lowest conduction band are considered for each spin. The corresponding bulk 8×8-Hamiltonian can be found in Table II in [[22]]. Löwdin renormalization (see [[23]]) was applied to the Luttinger parameters to include coupling to remote bands which were not explicitly included.

2.2 Bandstructure of quantum well structures

Nowadays, many opto-electronic devices are constructed by the growth of different nanometer-thick semiconductor layers in such a way that a quantum well heterostructure is formed. A common way to describe the bandstructure of quantum well heterostructures is to use the *envelope function approximation* [[24]]. An advantage of this approach is that within a plane of a layer the bulk bandstructure of the corresponding material is used. To obtain the continuous bandstructure of a heterostructure, the individual bandstructures of the layers are connected at the interface. This results in different types of *band offsets* between the layers. Band offsets specify how the bandgap difference of two semiconductor materials is divided between the locations of the valence band maxima and the conduction band minima of the corresponding bulk materials. This will be illustrated later in the text.
In Section 2.2.1, the envelope function approximation for quantum well heterostructures will be briefly introduced and the necessary modifications to the bulk $\mathbf{k}\cdot\mathbf{p}$-Hamiltonian for the description of quantum well structures will be discussed. In Section 2.2.2, different types of band offsets will be introduced.

2.2.1 Envelope function approximation

In the following, the case of a perfectly abrupt change in quantum well composition and quantum well potential, leading to rectangular potential landscapes, is assumed. In comparison to bulk materials, the confinement potential in quantum well heterostructures leads to the quantization of quasi-continuous energy states along the growth direction. Thereby, multiple subbands and confinement levels (or confinement energies) are introduced.[[15]]. This affects the transition energies. In this thesis mostly studies are presented where a focus is put on the fundamental transitions of heterostructures. Here, the confinement levels cause the corresponding transition energies to be shifted upwards in comparison to the differences of bulk valence band and bulk conduction band maxima.
In this thesis, the x- and y-coordinates are assigned to the layer's in-plane direction and the z-coordinate is assigned to the growth direction. While the motion of charge carriers is restricted in the z-direction by the potential landscape, in in-plane directions the carriers can move freely.
To take into account the modifications to the wavefunctions caused by the confinement potential, the plane wave envelope function in z-direction is

replaced by a quantized standing wave $\zeta_\lambda(z)$, called the *confinement function*. Here, λ labels the quantum well's state. Overall, the *confinement wavefunctions* can be written down as

$$\psi_{\lambda,\mathbf{k}_{||}}(\mathbf{r}) \;=\; \zeta_\lambda(z)\,\frac{e^{i\mathbf{k}_{||}\cdot\mathbf{r}_{||}}}{\sqrt{\mathcal{S}}}\,u_{\lambda,\mathbf{k}_{||}}(\mathbf{r}) \;=\; \frac{e^{i\mathbf{k}_{||}\cdot\mathbf{r}_{||}}}{\sqrt{\mathcal{S}}}\sum_n \zeta^{n,\lambda}_{\mathbf{k}_{||}}(z)\;u_{n,\mathbf{k}_0}(\mathbf{r})\,, \quad (2.9)$$

where n is the bulk band index, $\mathcal{S}$ is the quantization area, $\mathbf{k}_{||}$ is the carrier momentum in the quantum well-plane and $\mathbf{r}_{||}$ is the spatial coordinate in the quantum well-plane. $\zeta^{n,\lambda}_{\mathbf{k}_{||}}$ are expansion coefficients, analogous as in Eq. (2.5), and are often called confinement functions as well.
In order to calculate a quantum well heterostructure's bandstructure and confinement wavefunctions by $\mathbf{k}\cdot\mathbf{p}$-theory, the heterostructure's $\mathbf{k}\cdot\mathbf{p}$-matrix is obtained from the modified bulk one. For this purpose, the confinement potential is added to the diagonal of the Hamiltonian and k_z is replaced by $-i\partial_z = -i\frac{\partial}{\partial_z}$. This is done in the following way and results in a Hermitian Hamiltonian [[25]]:

$$k_z\,A \to \frac{1}{2}\left\{(-i\partial_z)\,A(z) + A(z)\,(-i\partial_z)\right\} \quad (2.10)$$

$$A\,k_z^2 \to (-i\partial_z)\,A(z)\,(-i\partial_z)\;. \quad (2.11)$$

Here, A represents any bandstructure parameter. In this way, all bandstructure parameters become dependent on z.
Subsequently, the eigenvalue problem of the heterostructure's Hamiltonian is solved to obtain the single-particle energies and confinement wavefunctions [[25]].
In the description of the emission or absorption of light, the probability of an optical transition can be described by its oscillator strength. The oscillator strength can be calculated from the corresponding dipole matrix element. Once the confinement wavefunctions have been calculated, a quantum well's dipole matrix element can be calculated as[1]

$$d^{\lambda\nu}_{\mathbf{k}_{||}} = \frac{i\hbar\,e}{m_0(\epsilon^\lambda_{\mathbf{k}_{||}} - \epsilon^\nu_{\mathbf{k}_{||}})\,\mathcal{S}}\sum_{n,m}\int\left(\zeta^{n,\lambda}_{\mathbf{k}_{||}}(z)\right)^*\,\zeta^{m,\nu}_{\mathbf{k}_{||}}(z)\,\mathbf{e}_p\cdot\mathbf{P}_{n,m}\,dz\,, \quad (2.12)$$

where e is the elementary charge, $\mathbf{P}_{n,m} = \langle n|\mathbf{p}|m\rangle$ is the bulk dipole matrix element and $\mathbf{e}_p$ is the polarization direction of the light. Moreover, the

[1] A more general discussion can be found in [[27]] section 6.4.

confinement wavefunctions enable one to calculate the Coulomb matrix elements as

$$V_{|\mathbf{k}_{||}|}^{\lambda_1,\lambda_2,\lambda_3,\lambda_4} = \frac{2\pi e^2}{\mathcal{S}\,\epsilon_0\,\epsilon_{BG}} \sum_{n,m} \int \left(\zeta_{\mathbf{k}_{||}}^{n,\lambda_1}(z)\,\zeta_{\mathbf{k}_{||}}^{m,\lambda_2}(z')\right)^* \frac{\mathrm{e}^{-|\mathbf{k}_{||}||z-z'|}}{|\mathbf{k}_{||}|} \cdot \zeta_{\mathbf{k}_{||}}^{m,\lambda_3}(z')\,\zeta_{\mathbf{k}_{||}}^{n,\lambda_4}(z)\,dzdz' \,. \quad (2.13)$$

Here, ϵ_0 is the vacuum permittivity and ϵ_{BG} is the dielectric constant.
Both, the Coulomb matrix elements and the dipole matrix elements are necessary during the calculation of the optical properties of a heterostructure as can be seen later on.
In general, quantum confinement not only introduces subbands but also leads to a lift of degeneracy for the topmost valence bands [[16]]. Additionally, the energetic location of the valence band maxima can be influenced by strained growth of semiconductor layers on a substrate with a differing lattice constant. In general, strained growth of semiconductor layers with different optical properties opens up a wide range of possibilities for heterostructure designs.
In the framework of this thesis, strain was taken into account by using the Pikus-Bir-formalism [[26, 27]] within the $\mathbf{k}\cdot\mathbf{p}$-formalism. The temperature dependence of the bandgaps was taken into account by the use of the Varshni-formula [[28]]. For ternary materials all used parameters were linearly interpolated from the corresponding binary materials if not stated otherwise. An exception is the bandgap where bowing enters with the material dependent bowing coefficient. All material parameters and coefficients are taken from [[29]].
Moreover, since the spatially separated electrons and holes generate an electric field, the confinement potential is modified in comparison to the potential in absence of this field. In the calculations, this is taken into account by self-consistently solving the Poisson equation when calculating the confinement wavefunctions, as in [[30]]. Hence, at first, the confinement wavefunctions are calculated without the consideration of the attraction between separated electrons and holes. Subsequently, the charge density distributions of the electrons and holes are calculated and the Poisson equation is set up and solved for the attractive Coulomb potential. This potential is then used to calculate the confinement wavefunctions once more. Thereafter, the new and old solutions are compared and it is decided whether another iteration is necessary.

2.2.2 Band alignment

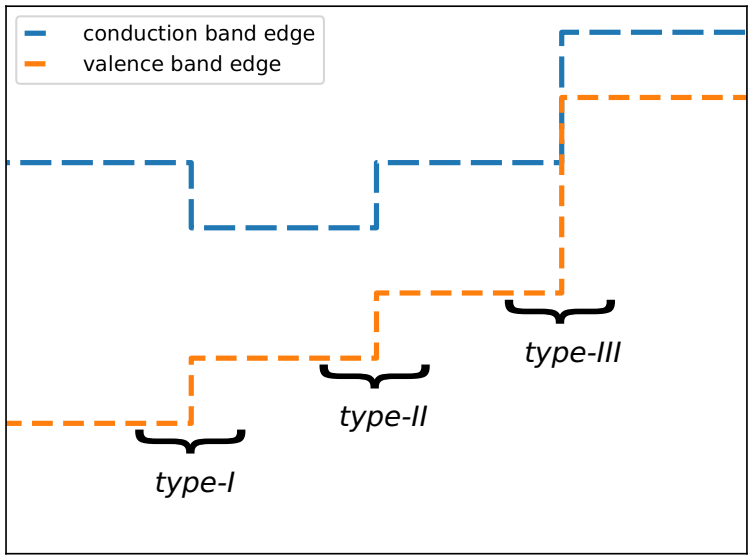

Figure 2.1: Visualization of different types of band offsets between pairs of different semiconductor layers. The labeling (type-I, type-II or type-III) refers to the pairs indicated by the brackets, respectively.

As mentioned before, the bandstructures of the individual layers of a heterostructure are connected at their interfaces assuming certain band offsets. This results in the alignment of the band edges of the layers. The valence band edge is defined as the bulk material's valence band maximum, and similarly the conduction band edge is defined as the bulk material's conduction band minimum. Below, a brief introduction of the different types of band offsets, which are illustrated in Fig 2.1, is given.

Type-I: straddling gap. The type-I band alignment between two semiconductor materials is characterized by the fact that the bandgap of one semiconductor material is enclosed by the bandgap of the other one. Conse-

quently, in a heterostructure made of such a pair of semiconductor materials the valence band maximum and the conduction band minimum of the structure belong to the same material.

Type-II: staggered gap. In the type-II band alignment the valence and conduction band edges of one semiconductor material are shifted in the same direction towards the valence and conduction band edges of the other material. In a heterostructure made of a pair of such materials, the valence band maximum and the conduction band minimum of the structure do not belong to the same material.

Type-III: broken gap. If the valence band edge of one semiconductor material is situated higher in energy than the conduction band edge of the other semiconductor material, the two materials have a type-III band alignment. A heterostructure made of a pair of materials with type-III band alignment has no effective bandgap.

2.3 Density functional theory

As mentioned in the introduction of Chapter 2, another approach to calculate the electronic structure of solids is DFT. DFT enables the calculation of ground state properties for many-body systems with an emphasis on the ground-state density. In general, DFT is not only applicable for solids, but since they are relevant for this thesis, this discussion focuses on them. Since DFT has the advantage of being independent from experimental input parameters, it is called an *ab initio* (or *first principles*) method. In practice, DFT is able to produce qualitatively good results while having a reasonable computational effort. Therefore, it has been widely applied to a broad range of problems (e.g. [[31–33]]). While the theorems of Hohenberg and Kohn [[34]] provided the key idea for DFT, the approach of Kohn and Sham [[35]] paved the way for practical DFT calculations. Since there is numerous literature available on DFT (for example [[36]]), it will only be briefly introduced.

2.3.1 Hohenberg-Kohn theorems

A solid represents a demanding many-body system that can be fully described by its many-body wavefunction $\Psi(\mathbf{r}_1, \mathbf{r}_2, \ldots, \mathbf{r}_N)$ where $\mathbf{r}_i$ are the position vectors of the N electrons. The many-body wavefunction is the solution of the the system's many-body Schrödinger equation

$$H\,\Psi(\mathbf{r}_1, \ldots, \mathbf{r}_N) = E\,\Psi(\mathbf{r}_1, \ldots, \mathbf{r}_N)\ . \tag{2.14}$$

Here, different contributions enter in H: $H = \mathcal{T} + \mathcal{U} + \mathcal{V}$, where $\mathcal{T}$ is the kinetic energy, $\mathcal{U}$ describes the electron-electron interaction and $\mathcal{V}$ is the external potential that contains contributions from the potential of the ions as well as potentially other external potentials. The different contributions to the system's energy will be revisited later in the text. H can be divided in a universal part comprising $\mathcal{T}+\mathcal{U}$, which can be used for the description of any electron system with the same number of electrons, and a system dependent part $\mathcal{V}$, which distinguishes one system from another.
The complexity of the underlying many-body problem generally prevents the analytic solution of Eq. (2.14). However, a big step towards an efficient numerical solution of complex many-body problems was made by Hohenberg and Kohn [[34]] who mapped the ground state wavefunction of the system onto its ground state density $\rho_0(\mathbf{r})$. This allows for a reduction of $3N$ coordinates to three. For systems with a non-degenerate ground state, the

justification for the use of the ground state density instead of the ground state wavefunction is summarized in the Hohenberg-Kohn theorems [[34]]:

1st Hohenberg-Kohn theorem: The ground state density $\rho_0(\mathbf{r})$ unambiguously determines the external potential besides a trivial additive constant.

2nd Hohenberg-Kohn theorem: The ground state density minimizes the system's total energy.

Both theorems can be proven by *reductio ad absurdum*.
From the first theorem it follows that the ground state density unambiguously determines H through the determination of the external potential. Consequently, the ground state energy is given as a functional of the ground state density:

$$E_0[\rho_0] = \langle \Psi | \mathcal{U} + \mathcal{T} + \mathcal{V} | \Psi \rangle = F[\rho_0] + V[\rho_0] \,, \tag{2.15}$$

where

$$F[\rho_0] = \langle \Psi | \mathcal{U} + \mathcal{T} | \Psi \rangle \tag{2.16}$$

is the universal part and

$$V[\rho_0] = \int \rho_0(\mathbf{r})\, \mathcal{V}(\mathbf{r})\, d^3r = \langle \Psi | \mathcal{V} | \Psi \rangle \tag{2.17}$$

is the system dependent part with the external potential $\mathcal{V}(\mathbf{r})$.
The second theorem allows for a variational principle to be applied for the determination of the ground state density that minimizes $E[\rho]$. While the dimensionality of the underlying problem is reduced, a new problem arises which is to determine the universal functional $F[\rho]$ for the interacting many-body system. Therefore, the formulation of the problem up to this point does not constitute a way of actually solving it.

2.3.2 Kohn-Sham equations

One year after Hohenberg and Kohn's groundbreaking publication [[34]], Kohn and Sham reformulated the problem [[35]] and thereby paved the way for practical applications. This was done by dividing the energy functional of Eq. (2.15) into a non-interacting part and a part which contains all unknown many-body contributions. The energy functional will be revisited later.
Important in their approach is the introduction of auxiliary non-interacting

single-electron orbitals $\psi_i(\mathbf{r})$ called the *Kohn-Sham orbitals* (KS-orbitals), which are used to map the system of interacting electrons onto the auxiliary system of non-interacting electrons. This auxiliary system belongs to the same ground state density as the actual interacting electron system. The electron density can be calculated with the KS-orbitals as

$$\rho(\mathbf{r}) = \sum_{i=1}^{N} n_i \mid \psi_i(\mathbf{r}) \mid^2, \tag{2.18}$$

where n_i is the occupation of orbital i. Using the KS-orbitals, we can separate the kinetic energy functional $T[\rho] = \langle \Psi \mid \mathcal{T} \mid \Psi \rangle$ into a single-particle, T_s, and a correlation part, T_c:

$$T[\rho] = T_s[\rho] + T_c[\rho] = \frac{-\hbar^2}{2m_0} \sum_{i=1}^{N} \int \psi_i^*(\mathbf{r}) \nabla^2 \psi_i(\mathbf{r}) \, d^3r + T_c[\rho]. \tag{2.19}$$

Here, T_c takes into account the difference between the true many-body problem's kinetic energy and the kinetic energy T_s of the non-interacting electrons. Strictly speaking, instead of a functional of the density, T_s is a functional of the KS-orbitals which are in turn functionals of the density. In this way T_s is implicitly a functional of the density. Likewise, we can divide the electron-electron interaction energy functional $U[\rho] = \langle \Psi \mid \mathcal{U} \mid \Psi \rangle$ in a Hartree part, U_H, and an exchange (or more general: non-classical) part, U_x:

$$U[\rho] = U_H[\rho] + U_x[\rho] = \frac{e^2}{8\pi\epsilon_0} \int \int \frac{\rho(\mathbf{r}) \rho(\mathbf{r}')}{|\mathbf{r} - \mathbf{r}'|} d^3r d^3r' + U_x[\rho]. \tag{2.20}$$

Whereas T_s and U_H are known, the remaining terms constitute the exchange-correlation energy:

$$E_{xc}[\rho] = T_c[\rho] + U_x[\rho]. \tag{2.21}$$

Everything unknown is in here. How this functional can be approximated will be mentioned in Section 2.3.3. The total energy of the system can be written down as the functional

$$E[\rho] = T_s[\rho] + U_H[\rho] + E_{xc}[\rho] + V[\rho]. \tag{2.22}$$

The ground state energy is obtained by variation of Eq. (2.22):

$$0 = \frac{\delta E[\rho]}{\delta \rho(\mathbf{r})} = \frac{\delta T_s[\rho]}{\delta \rho(\mathbf{r})} + \mathcal{U}_H(\mathbf{r}) + \mathcal{V}_{xc}(\mathbf{r}) + \mathcal{V}(\mathbf{r}), \tag{2.23}$$

where the Hartree-potential

$$\mathcal{U}_H(\mathbf{r}) = \frac{e^2}{4\pi\epsilon_0}\int \frac{\rho(\mathbf{r}')}{|\mathbf{r}-\mathbf{r}'|}d^3r' \tag{2.24}$$

and the exchange-correlation potential

$$\mathcal{V}_{xc}(\mathbf{r}) = \frac{\delta E_{xc}[\rho]}{\delta\rho(\mathbf{r})} \tag{2.25}$$

have been used.
By applying the method of Lagrange multipliers when minimizing the total energy, we obtain the Kohn-Sham equations [[35]]:

$$\left(\frac{-\hbar^2}{2m_0}\nabla^2 + \mathcal{U}_H(\mathbf{r}) + \mathcal{V}_{xc}(\mathbf{r}) + \mathcal{V}(\mathbf{r})\right)\psi_i(\mathbf{r}) = \epsilon_i\,\psi(\mathbf{r})\ . \tag{2.26}$$

Where ϵ_i are the Kohn-Sham eigenvalues (KS-energy eigenvalues).
Consequently, when calculating the total energy of a system we can solve N single-particle equations instead of a N-particle Schrödinger equation.

2.3.3 Exchange-correlation functionals

The introduction of the exchange-correlation potential allows for the usage of the non-interacting KS-orbitals. Still, the problem of how to explicitly express the unknown exchange-correlation potential remains. For this, different approaches have been made (see [[35, 37, 38]] for examples). Subsequently, two important exchange-correlation functional classes will be briefly introduced.
The first common approximation to the exchange-correlation energy, which provided the basis for all other approaches, was introduced with the local density approximation (LDA) [[35]]. In the LDA description of E_{xc}, the exchange-correlation energy per electron $\epsilon_{xc}(\rho(\mathbf{r}))$ of a homogeneous electron gas is used which belongs to the same local density as is found locally in the examined system:

$$E_{xc}[\rho(\mathbf{r})] = \int \epsilon_{xc}^{LDA}(\rho(\mathbf{r}))\,\rho(\mathbf{r})\,d^3r\,. \tag{2.27}$$

While LDA is the numerically least demanding approach, it produces qualitatively good results for different kinds of systems (e.g. [[39, 40]]). It is remarkable that although LDA makes use of the exchange-correlation energy of a homogeneous electron gas, it has proven to be useful for inhomogeneous

systems as well. However, when applying LDA for semiconductors, lattice constants [[41]] and bandgaps are often significantly underestimated [[42]]. In order to better take into account the non-uniform character of a given electron density, the generalized gradient approximations (GGAs) were introduced (see [[37, 43]] for examples). Here, the exchange-correlation energy is formulated as a semi-local functional of the electron density and its gradient:

$$E_{xc}[\rho(\mathbf{r})] = \int \epsilon_{xc}^{GGA}(\rho(\mathbf{r}), \nabla\rho(\mathbf{r}))\,\rho(\mathbf{r})\,d^3r\,. \tag{2.28}$$

Such a functional has been used for the results presented in this thesis. More specifically, the functional PBEsol [[44]] has been used which is based on the functional PBE [[37]] but has been parametrized for solids. For solids, PBEsol is known to improve the accuracy of calculated lattice constants in comparison to LDA and PBE [[44]] as well.

Nevertheless, for certain Sb concentrations in Ga(AsSb), the problem of vanishing Kohn Sham-bandgaps (KS-bandgaps) occurs during electronic structure calculations with PBEsol. Since such concentrations were considered for the research that will be presented in Section 4.2.2, this problem needed to be addressed. The so-called technique of *half-occupations* [[5, 6, 8, 45]] provides an approach for addressing this problem. Since this technique was used for the results that will be presented in Section 4.2.2, it will be introduced below.

2.3.4 DFT-1/2

The technique of half occupations relates back to a publication of Slater and Johnson in the 1970s [[8]], in which the authors present their $X\alpha$-method. This method enables the calculation of ionization energies that agree well with experimental values even for systems where calculations with the Hartree-Fock method were numerically too expensive at that time. Slater and Johnson introduced the so-called *transition state* ([[8]] and references therein). The transition state refers to a state in which the occupation is halfway between the occupation of the ground state and the excited state for which the corresponding transition energy can be computed as the energy eigenvalue of this transition state. Hence, this method is often called the the *half-occupation technique*.
Some years later, Janak proved that this transition-state technique can be applied in DFT calculations as well [[45]].
Decades later, Ferreira *et al.* [[5, 46]] applied the half-occupation technique

for correcting the energy of valence band states in electronic structure calculations within DFT. In their publications, they compared results from LDA-DFT calculations with and without the use of the half-occupation technique and labeled the use of this technique with LDA-1/2. Applying LDA-1/2, Ferreira *et al.* [[5]] obtained atomic ionization energies that agree well with experimental results and bandgaps that agree with experimental bandgaps, even when the corresponding bandgaps from LDA calculations significantly differ from the experimental ones [[5, 46]]. In a subsequent publication it was shown that their method can be applied in combination with the GGA functional PBE as well [[46]].
Below, the necessary concepts for using the method of half occupations within DFT will be briefly introduced. In doing so, the notation of Ferreira *et al.* will be followed, and cgs units are used.
Based on Janak's results, Ferreira *et al.* proceeded from the KS-energy eigenvalue ϵ_i in its differential form:

$$\epsilon_i(n_i) = \frac{\partial E}{\partial n_i}\,, \tag{2.29}$$

where E is the total energy of the system studied and n_i is the occupation of state i.
The energy eigenvalue of the half ionized state i can be obtained from the difference of the ground state's energy and the ion's energy. For this purpose, Eq.(2.29) is integrated and the KS-energy eigenvalue is assumed to depend linearly on the occupation [[46]]:

$$E\,(0) - E\,(-1) = \int_{-1}^{0} \frac{\partial E}{\partial n_i}\, dn_i = \int_{-1}^{0} \epsilon_i(n_i)\, dn_i = \epsilon_i\,(-1/2)\ . \tag{2.30}$$

Here, $\epsilon_i\,(-1/2)$ is the half ionized state's KS-energy eigenvalue and $E\,(0)$ is the ground state's total energy while $E\,(-1)$ is the total energy of the system with a single electron removed.
Taking the derivative of the KS-energy eigenvalue with respect to the occupation yields [[6, 46]]

$$\begin{aligned}\frac{\partial \epsilon_i}{\partial n_i} = \int\int d^3r\; d^3r' \rho_i(\mathbf{r}) \Bigg[\frac{\rho_i(\mathbf{r}')}{\mid \mathbf{r} - \mathbf{r}' \mid} + \frac{1}{\mid \mathbf{r} - \mathbf{r}' \mid} \sum_{j \neq i} n_j \frac{\partial \rho_j(\mathbf{r}')}{\partial n_i} \\ + \frac{\delta^2 E_{xc}}{\delta\rho(\mathbf{r})\delta\rho(\mathbf{r}')}\rho_i(\mathbf{r}') + \frac{\delta^2 E_{xc}}{\delta\rho(\mathbf{r})\delta\rho(\mathbf{r}')} \sum_{j \neq i} n_j \frac{\partial \rho_j(\mathbf{r}')}{\partial n_i} \Bigg]\,.\end{aligned} \tag{2.31}$$

Because of the self-energy character of the first term on the right hand side of Eq. (2.31), Ferreira *et al.* introduced the *self-energy* S_i, which is used for the correction of state i's energy, as

$$S_i = \frac{1}{2}\frac{\partial \epsilon_i}{\partial n_i}\,. \tag{2.32}$$

The self-energy is related to the self-energy potential V_S by

$$S_i = \int d^3r\, \rho_i\left(\mathbf{r}\right) V_S\left(\mathbf{r}\right) \tag{2.33}$$

with

$$\begin{aligned} V_S\left(\mathbf{r}\right) = \frac{1}{2}\int d^3r' \Bigg[& \frac{\rho_i(\mathbf{r}')}{\mid \mathbf{r}-\mathbf{r}' \mid} + \frac{1}{\mid \mathbf{r}-\mathbf{r}' \mid}\sum_{j\neq i} n_j \frac{\partial \rho_j(\mathbf{r}')}{\partial n_i} \\ & + \frac{\delta^2 E_{xc}}{\delta\rho(\mathbf{r})\delta\rho(\mathbf{r}')}\rho_i(\mathbf{r}') + \frac{\delta^2 E_{xc}}{\delta\rho(\mathbf{r})\delta\rho(\mathbf{r}')}\sum_{j\neq i} n_j \frac{\partial \rho_j(\mathbf{r}')}{\partial n_i} \Bigg]\,. \end{aligned} \tag{2.34}$$

Applying the self-energy correction to atoms, a much simpler expression for V_S than Eq. (2.34) can be used [[5, 46]]:

$$V_S(r) = V(0,r) - V(-1/2,r)\,. \tag{2.35}$$

In Eq. (2.35), $V(0,r)$ is the Kohn-Sham potential of the atom in its ground state and $V(-1/2,r)$ the Kohn-Sham potential of the half ion.
Eq. (2.35) can be used for solids as well. Important for this is that the wavefunction of the utilized state of the solid does not substantially differ from that of the corresponding atom. The applicability of this Eq. (2.35) favored by the strong localization of the charge carriers in the valence band of a semiconductor.
In practical applications, the self-energy potentials from Eq. (2.35) can be calculated by using the ATOM code [[47]] which produces atomic pseudopotentials that can be used regardless of the chosen DFT code package. ATOM enables partial ionization of the atomic orbitals that form the top-most valence band when the atoms form the semiconductor. After generating them, the self-energy potentials can be added as external potentials to the pseudopotentials of the corresponding atoms and subsequently these can be used to generate the pseudopotential of the semiconductor. This needs to be done in a suitable manner and will be discussed below.
Furthermore, in the case of covalent bonds, the bonding electrons are shared and one must be careful with the amount of charges that are stripped off.

Incorporating the self-energy potentials of each atom that is part of the covalent bond into the pseudopotential of the solid leads to a double counting of the correction. Therefore, in such cases 1/4 charges are stripped off [[5, 6]].
Still, one problem remains when the pseudopotentials of the atoms that were corrected by adding V_S to them are joined to form the pseudopotential of the solid, namely that the self-energy potential's tails from the atoms overlap with each other and thereby numerical divergence is caused. Hence, V_S needs to be suitably truncated. For this purpose, Ferreira *et al.* introduced a cut-off function for a sphere-like trimming:

$$\theta(r) = \begin{cases} \left[1 - \left(\frac{r}{r_{cut}}\right)^n\right]^3 & \text{for } r \leq r_{cut} \ . \\ 0 & \text{for } r > r_{cut} \end{cases} \tag{2.36}$$

Here n should be even and as large as numerically possible to guarantee a sharp cut-off.
Physically, the idea behind this truncation is that the self-energy potential should be applied only in regions where the wavefunction of the respective state is not negligible [[5, 13]]. As presented in [[5]], the parameter r_{cut} from Eq. (2.36) is obtained from bandgap maximization of the examined semiconductor or insulator. For this, the trimmed self-energy potentials are joined into the pseudopotentials of the atoms from which the pseudopotenial of the solid is then generated. After this, the bandgap of the solid is calculated within DFT. This is repeated for different radii. Finally, for each considered element the radius that maximized the bandgap of the corresponding solid is chosen. The number of different elements to which the self-energy correction is applied depends on the solid and the type of chemical bond in it [[5, 6]]. Ferreira *et al.* applied the correction scheme to elementary insulators and semiconductors as well as to binary compounds [[5, 46]]. For the calculations that are presented in Section 4.2.2, it has been applied to binary and ternary semiconductors. If the correction is applied to two elements, at first one cut-off radius is obtained by bandgap maximization. Subsequently, the resulting trimmed pseudopotential is used to find the second cut-off radius. If three cut-off radii are needed for a ternary semiconductor, bandgap maximization of two suitable binary semiconductors provides the optimized radii for all elements.
Ferreira *et al.* state that for fixed atom and bonding type r_{cut} weakly depends on the chemical environment [[5]]. Because of this, they applied the same r_{cut} to the same anion in different binary semiconductors.

However, a spherical trimming scheme for the self-energy potential can lead to an erroneous downward shift in energy of conduction band states. This is for example the case when the hole resides along the bonds and conduction band states near the core overlap with $\theta(\mathbf{r})\, V_S(\mathbf{r})$. As a solution, Xue *et al.* [[6]] introduced an improved cut-off function which allows for a trimming in form of a spherical-shell:

$$\theta_{sh}(r) = \begin{cases} 0 & \text{for } r < r_{in} \\ \left[1 - \left(\dfrac{2\,(r - r_{in})}{r_{out} - r_{in}} - 1\right)^{n}\right]^{3} & \text{for } r_{in} \leq r \leq r_{out}\ . \\ 0 & \text{for } r > r_{out} \end{cases} \tag{2.37}$$

Here, inner and outer cut-off radii r_{in} and r_{out} are necessary and, as before, n should be even and as large as numerically possible. Again, the radii are obtained from bandgap maximization. For the results presented in this thesis, $n = 20$ was used for each cut-off function.
While Eq. (2.37) was used to produce the results presented in Section 4.2.2, the effect of using Eq. (2.36) on the valence band offset results is tested in this chapter as well.

2.4 Calculation of optical properties

Subsequently, the microscopic many-body theory from which the absorption (or gain) and photoluminescence (PL) of quantum well heterostructures can be calculated will be introduced. While Section 2.4.1 introduces the semiconductor Bloch equations (SBEs) for the calculation of the absorption, Section 2.4.2 introduces the semiconductor luminescence equations (SLEs) for the calculation of the PL.
For this purpose, the second quantization will be used in the following sections. In the second quantization formalism, the fermionic creation and annihilation operators $a^{\dagger}_{\mu,\mathbf{k}_{||}}$ and $a_{\mu,\mathbf{k}_{||}}$ create or annihilate an electron in subband state μ with in-plane momentum $\mathbf{k}_{||}$.
For the description of an interacting system's time dependence, the Heisenberg picture will be used. For simplicity, the time dependence of the operators will usually not be explicitly noted (e.g. O instead of $O(t)$). In the Heisenberg picture, the temporal evolution of an operator that acts on a system is connected to the system's Hamiltonian H via the Heisenberg's equation of motion:

$$i\hbar \frac{\partial}{\partial t} O = [O, H] \ . \tag{2.38}$$

Therefore, the dynamics of an observable can be obtained by taking the expectation value of Eq. (2.38):

$$i\hbar \frac{\partial}{\partial t} \langle O \rangle = \langle [O, H] \rangle \, . \tag{2.39}$$

Applying this technique for an N-particle operator, the interaction terms in H cause coupling to $(N+1)$-particle operators on the right hand side of Eq. (2.38) (or equivalent Eq. (2.39)). The dynamics of the newly introduced operators are in turn determined by Eq. (2.38) and couple to $(N+2)$-particle operators. In this way, the so-called *infinite hierarchy* problem is caused, given by the coupled set of differential equations obtained from the use of Eq. (2.38). For a many-body problem, the set of coupled differential equations can not be solved analytically. In order to overcome this, a systematic truncation needs to be applied. The so-called *cluster expansion* (for more details see [[15]] and references therein) is a formalism that allows one to carry out a systematic truncation while preserving physically relevant information.
In the cluster expansion, a N-particle quantity is systematically decomposed into combinations of single-particle quantities and higher-order-particle quantities and correlations [[15]]. For an underlying physical problem, the cluster

expansion is truncated at the lowest possible level such that all relevant effects are still included but the numerical effort is reduced.
During the calculations that were carried out for this thesis, higher order contributions were factorized into expectation values of single-particle quantities, applying the Hartree-Fock approximation [[15]]. The scattering terms were treated at the level of the second-Born scattering approximation [[15, 16]] which was generally used in the Markov-limit. The latter refers to omitting memory effects.

2.4.1 Semiconductor Bloch equations

The optical response of a quantum well heterostructure can be determined from the macroscopic polarization $P(t)$. The macroscopic polarization can be calculated from the microscopic polarizations $p^{\nu\lambda}_{\mathbf{k}_{||}} = \langle a^{\dagger}_{\lambda,\mathbf{k}_{||}} a_{\nu,\mathbf{k}_{||}} \rangle$ as

$$P(t) = \frac{1}{\sqrt{\mathcal{S}}} \sum_{\lambda,\nu,\mathbf{k}_{||}} \left(\left(d^{\lambda\nu}_{\mathbf{k}_{||}} \right)^{*} p^{\nu\lambda}_{\mathbf{k}_{||}} + d^{\lambda\nu}_{\mathbf{k}_{||}} \left(p^{\nu\lambda}_{\mathbf{k}_{||}} \right)^{*} \right). \tag{2.40}$$

Here, λ and ν label the conduction and valence band states in the heterostructure, respectively. The dynamics of the microscopic polarizations are calculated using Eq. (2.39), which leads to the SBEs. The SBEs are a coupled set of differential equations for $p^{\nu\lambda}_{\mathbf{k}_{||}}$ and the electron $f^{\lambda}_{\mathbf{k}_{||}} = \langle a^{\dagger}_{\lambda,\mathbf{k}_{||}} a_{\lambda,\mathbf{k}_{||}} \rangle$ and hole occupations $f^{\nu}_{\mathbf{k}_{||}} = 1 - \langle a^{\dagger}_{\nu,\mathbf{k}_{||}} a_{\nu,\mathbf{k}_{||}} \rangle$.
In Eq. (2.39), the many-particle system's Hamiltonian

$$H = H_0 + H_C + H_D + H_P \tag{2.41}$$

is inserted. Here, $H_0 = H^e_0 + H^p_0$ describes the non-interacting contributions from electrons,

$$H^e_0 = \sum_{\mu,\mathbf{k}_{||}} \epsilon^{\mu}_{\mathbf{k}_{||}} a^{\dagger}_{\mu,\mathbf{k}_{||}} a_{\mu,\mathbf{k}_{||}}, \tag{2.42}$$

and phonons,

$$H^p_0 = \sum_{\beta,\mathbf{p}_{||},p_{\perp}} \hbar\,\Omega^{\beta}_{\mathbf{p}_{||},p_{\perp}} \left(D^{\beta\dagger}_{\mathbf{p}_{||},p_{\perp}} D^{\beta}_{\mathbf{p}_{||},p_{\perp}} + \frac{1}{2} \right), \tag{2.43}$$

where $D^{\beta\dagger}_{\mathbf{p}_{||},p_{\perp}}$ ($D^{\beta}_{\mathbf{p}_{||},p_{\perp}}$) is the bosonic phonon creation (annihilation) operator, $\hbar\,\Omega^{\beta}_{\mathbf{p}_{||},p_{\perp}}$ the phonon energy and β the phonon type. $\mathbf{p} = (\mathbf{p}_{||}, p_{\perp})$ is

the phonon wavevector with the in-plane coordinates denoted by $\mathbf{p}_{||}$ and the coordinate in growth direction is denoted by $p_\perp$.
The remaining contributions in Eq. (2.41) describe many-body interactions. Here, the Coulomb interaction among carriers is described by

$$H_C = \frac{1}{2}\sum_{\mu,\mu'}\sum_{\mathbf{k}_{||},\mathbf{k}'_{||},\mathbf{q}_{||}\neq\mathbf{0}} V^{\mu\,\mu'\mu'\mu}_{|\mathbf{q}_{||}|}\, a^\dagger_{\mu,\mathbf{k}_{||}+\mathbf{q}_{||}} a^\dagger_{\mu',\mathbf{k}'_{||}-\mathbf{q}_{||}} a_{\mu',\mathbf{k}'_{||}} a_{\mu,\mathbf{k}_{||}}\,. \tag{2.44}$$

The interaction of charge carriers with phonons is described by

$$H_P = \hbar\sum_{\beta,\mu}\sum_{\mathbf{p}_{||},p_\perp,\mathbf{k}_{||}} G^\mu_{\mathbf{p}_{||},p_\perp}\left(D^\beta_{\mathbf{p}_{||},p_\perp} + \left(D^\beta_{-\mathbf{p}_{||},p_\perp}\right)^\dagger\right) a^\dagger_{\mu,\mathbf{k}_{||}} a_{\mu,\mathbf{k}_{||}-\mathbf{p}_{||}} \tag{2.45}$$

where $G^\mu_{\mathbf{p}_{||},p_\perp}$ is the Fröhlich matrix element [[15, 48]]
In the Hamiltonian from Eq. (2.41), the light field can be described classically to obtain the SBEs. As a result, the light-matter interaction is described semi-classically. This stems from the fact that the light field generated by an ideal, coherent laser is as close as possible to classical light [[15]]. The corresponding Hamiltonian, which is labeled with D since it describes dipole transitions between bands, is given by

$$H_D = -E(t)\sum_{\lambda,\nu,\mathbf{k}_{||}}\left(\; d^{\lambda\nu}_{\mathbf{k}_{||}} a^\dagger_{\lambda,\mathbf{k}_{||}} a_{\nu,\mathbf{k}_{||}} + \text{ c.c. }\right). \tag{2.46}$$

Here, $E(t)$ is the classical light field. When the system's Hamiltonian is used in Eq. (2.39) to obtain the dynamics of $p^{\nu\lambda}_{\mathbf{k}_{||}}$, one finds that the resulting equation couples to $f^\lambda_{\mathbf{k}_{||}}$ and $f^\nu_{\mathbf{k}_{||}}$. The dynamics of the distribution functions can in turn be determined using Eq. (2.39). Altogether, this leads to the SBEs:

$$\begin{aligned}\frac{\partial}{\partial t}p^{\nu\lambda}_{\mathbf{k}_{||}} = {}& \frac{1}{i\hbar}\sum_{\nu',\lambda'}\left(\epsilon^{\nu\nu'}_{\mathbf{k}_{||}}\delta_{\lambda,\lambda'} + \epsilon^{\lambda\lambda'}_{\mathbf{k}_{||}}\delta_{\nu,\nu'}\right) p^{\nu'\lambda'}_{\mathbf{k}_{||}} \\ & -(1-f^\lambda_{\mathbf{k}_{||}}-f^\nu_{\mathbf{k}_{||}})\frac{1}{i}\Omega^{\lambda\nu}_{\mathbf{k}_{||}} + \frac{\partial}{\partial t}p^{\nu\lambda}_{\mathbf{k}_{||}}\Big|_{scatt}\end{aligned} \tag{2.47}$$

$$\frac{\partial}{\partial t}f^\lambda_{\mathbf{k}_{||}} = -2\,\mathrm{Im}\left(\sum_\nu \Omega^{\lambda\nu}_{\mathbf{k}_{||}}\left(p^{\nu\lambda}_{\mathbf{k}_{||}}\right)^*\right) + \frac{\partial}{\partial t}f^\lambda_{\mathbf{k}_{||}}\Big|_{scatt} \tag{2.48}$$

$$\frac{\partial}{\partial t}f^\nu_{\mathbf{k}_{||}} = -2\,\mathrm{Im}\left(\sum_\lambda \Omega^{\lambda\nu}_{\mathbf{k}_{||}}\left(p^{\nu\lambda}_{\mathbf{k}_{||}}\right)^*\right) + \frac{\partial}{\partial t}f^\nu_{\mathbf{k}_{||}}\Big|_{scatt}. \tag{2.49}$$

Into the SBEs (Eqs. (2.47)-(2.49)), the renormalized single-particle energies

$$\epsilon^{\lambda\lambda'}_{\mathbf{k}_{||}} = \epsilon^{\lambda}_{\mathbf{k}_{||}}\,\delta_{\lambda,\lambda'} - \sum_{\lambda'',\mathbf{q}_{||}} V^{\lambda\lambda''\lambda'\lambda''}_{|\mathbf{k}_{||}-\mathbf{q}_{||}|}\, f^{\lambda''}_{\mathbf{q}_{||}} \tag{2.50}$$

and

$$\epsilon^{\nu\nu'}_{\mathbf{k}_{||}} = \epsilon^{\nu}_{\mathbf{k}_{||}}\,\delta_{\nu,\nu'} - \sum_{\nu'',\mathbf{q}_{||}} V^{\nu'\nu''\nu\nu''}_{|\mathbf{k}_{||}-\mathbf{q}_{||}|}\, f^{\nu''}_{\mathbf{q}_{||}} \tag{2.51}$$

enter, and

$$\Omega^{\lambda\nu}_{\mathbf{k}_{||}} = \frac{d^{\lambda\nu}_{\mathbf{k}_{||}}\,E\,(t)}{\hbar} + \frac{1}{\hbar}\sum_{\lambda',\nu',\mathbf{q}_{||}} V^{\lambda\nu'\nu\lambda'}_{|\mathbf{k}_{||}-\mathbf{q}_{||}|} p^{\nu'\lambda'}_{\mathbf{q}_{||}} \tag{2.52}$$

is the renormalized Rabi frequency. Eq. (2.52) shows that the charge carriers react to an effective field which consists of the applied field $E\,(t)$ weighted with $d^{\lambda\nu}_{\mathbf{k}_{||}}$ in the first term and the internal dipole field of the excited charge carriers in the second term [[16]].
The subscript *scatt* marks the scattering terms from electron-electron and electron-phonon scattering processes, which are treated at the level of the second-Born approximation [[49, 50]].
Since for this thesis situations were considered where high charge carrier densities that show no major temporal changes are present, instead of solving Eq. (2.48) and Eq. (2.49), Fermi-Dirac distributions were used in Eq. (2.47).
From the microscopic polarizations, the macroscopic polarization $P(t)$ can be calculated according to Eq. (2.40). By Fourier transformation of $P(t)$ into frequency space, the frequency dependent absorption $\alpha(\omega)$ is calculated as

$$\alpha(\omega) = \frac{\omega}{c\,n_{BG}\,\epsilon_0}\mathrm{Im}\left(\frac{P(\omega)}{E(\omega)}\right). \tag{2.53}$$

Here, c is the speed of light in vacuum and n_{BG} is the background refractive index.
Since negative absorption represents light-emission, it is called *gain* due to the enhancement of the incident light-field. By convolution of the gain spectrum with a Gaussian distribution, the spectrum can be inhomogeneously broadened to take fluctuations of quantum well widths and compositions into account.

2.4.2 Semiconductor luminescence equations

While the coherent polarizations decay on a picosecond time scale, the characteristic lifetime of the incoherent carrier densities is in the nanoseconds

range [[15]]. As long as population inversion is present, luminescence can be generated by spontaneous recombination of electron-hole pairs. The light field generated by this quantum mechanical process cannot be described classically. Hence, to obtain the SLEs and calculate the PL from these, the bosonic photon creation and annihilation operators $\left(B^{\beta}_{\mathbf{q}_{||},q_\perp}\right)^\dagger$ and $B^{\beta}_{\mathbf{q}_{||},q_\perp}$ are introduced into the system's Hamiltonian. Here, β is the light polarization and $\mathbf{q}_{||}$ and $q_\perp$ are the in-plane components and the component in growth direction of the photon wavevector $\mathbf{q}$, respectively.
The quantized light-field causes the modification of Eq. (2.41) to

$$H = H_0 + H_C + H_P + H_{LM}\,, \tag{2.54}$$

where $H_0 = H_0^e + H_0^p + H_0^l$. Here, the free-photon Hamiltonian H_0^l is defined as

$$H_0^l = \sum_{\beta,\mathbf{q}_{||},q_\perp} \hbar\,\omega_{\mathbf{q}_{||},q_\perp} \left(\left(B^{\beta}_{\mathbf{q}_{||},q_\perp}\right)^\dagger B^{\beta}_{\mathbf{q}_{||},q_\perp} + \frac{1}{2}\right). \tag{2.55}$$

H_{LM} is the fully quantized light-matter interaction Hamiltonian

$$H_{LM} = -i\hbar \sum_{\beta,\lambda} \sum_{\mathbf{q}_{||},q_\perp,\mathbf{k}_{||}} \left(\mathcal{F}^{\lambda\nu}_{\mathbf{k}_{||}\mathbf{q}_{||},q_\perp}\, B^{\beta}_{\mathbf{q}_{||},q_\perp}\, a^\dagger_{\lambda,\mathbf{k}_{||}+\mathbf{q}_{||}} a_{\nu,\mathbf{k}_{||}} + c.c.\right), \tag{2.56}$$

which replaces H_D in Eq. (2.41). $\mathcal{F}^{\lambda\nu}_{\mathbf{k}_{||}\mathbf{q}_{||},q_\perp} = d^{\lambda\nu}_{\mathbf{k}_{||}}\,\mathcal{E}_{\mathbf{q}_{||},q_\perp} u^{\beta}_{\mathbf{q}_{||},q_\perp}/\hbar$ is the light-matter coupling matrix element where $\mathcal{E}_{\mathbf{q}_{||},q_\perp} = \sqrt{\left(\hbar\,\omega_{\mathbf{q}_{||},q_\perp}\right)/\left(2\varepsilon_0\right)}$ is the vacuum field amplitude and $u^{\beta}_{\mathbf{q}_{||},q_\perp}$ is the effective mode function [[15]].
For the purpose of calculating PL spectra, the dynamics of the photon-number-like correlations $\Delta\langle\,(B^{\beta}_{\mathbf{q}_{||},q_\perp})^\dagger B^{\beta}_{\mathbf{q}_{||},q'_\perp}\,\rangle$ are used. More specifically, the PL can be obtained from the resonant part $\Delta\langle\,(B^{\beta}_{\mathbf{q}_{||},q_\perp})^\dagger B^{\beta}_{\mathbf{q}_{||},q_\perp}\,\rangle$, since it is proportional to the temporal change of the photon number for photons with energy $\hbar\,\omega_{\mathbf{q}_{||},q_\perp}$. The dynamics of $\Delta\langle\,(B^{\beta}_{\mathbf{q}_{||},q_\perp})^\dagger B^{\beta}_{\mathbf{q}_{||},q_\perp{}'}\,\rangle$ are obtained using Eq. (2.39):

$$\begin{aligned}\frac{\partial}{\partial t}\Delta\langle\,(B^{\beta}_{\mathbf{q}_{||},q_\perp})^\dagger B^{\beta}_{\mathbf{q}_{||},q_\perp{}'}\,\rangle &= i\left(\omega_{\mathbf{q}_{||},q_\perp} - \omega_{\mathbf{q}_{||},q_\perp{}'}\right)\Delta\langle\,(B^{\beta}_{\mathbf{q}_{||},q_\perp})^\dagger B^{\beta}_{\mathbf{q}_{||},q_\perp{}'}\,\rangle \\ &+ \sum_{\lambda,\nu,\mathbf{k}_{||}} \left(\mathcal{F}^{\lambda\nu}_{\mathbf{k}_{||}\mathbf{q}_{||},q_\perp}\left(\Pi^{\lambda,\nu}_{\mathbf{k}_{||},\mathbf{q}_{||},q_\perp{}'}\right)^* + \left(\mathcal{F}^{\lambda\nu}_{\mathbf{k}_{||}\mathbf{q}_{||},q_\perp{}'}\right)^* \Pi^{\lambda,\nu}_{\mathbf{k}_{||},\mathbf{q}_{||},q_\perp}\right).\end{aligned} \tag{2.57}$$

This equation couples to the photon-assisted polarization

$$\Pi^{\lambda,\nu}_{\mathbf{k}_{||},\mathbf{q}_{||},q_\perp} = \Delta\langle\, (B^{\beta}_{\mathbf{q}_{||},q_\perp})^\dagger\, a^\dagger_{\nu,\mathbf{k}_{||}-\mathbf{q}} a_{\lambda,\mathbf{k}_{||}}\,\rangle\,, \tag{2.58}$$

whose equation of motion is in turn determined using Eq. (2.39) [[15, 48]]

$$\begin{aligned}
&i\hbar\frac{\partial}{\partial t}\Pi^{\lambda,\nu}_{\mathbf{k}_{||},\mathbf{q}_{||},q_\perp} = \left(\epsilon^{\lambda}_{\mathbf{k}_{||}} - \epsilon^{\nu}_{\mathbf{k}_{||}-\mathbf{q}_{||}} - \hbar\omega_{\mathbf{q}_{||},q_\perp}\right)\Pi^{\lambda,\nu}_{\mathbf{k}_{||},\mathbf{q}_{||},q_\perp} \\
&- \sum_{\lambda'}\Pi^{\lambda',\nu}_{\mathbf{k}_{||},\mathbf{q}_{||},q_\perp}\sum_{\lambda'',\mathbf{k}'_{||}} V^{\lambda\lambda''\lambda'\lambda''}_{|\mathbf{k}_{||}-\mathbf{k}'_{||}|} f^{\lambda''}_{\mathbf{k}'_{||}} - \sum_{\nu'}\Pi^{\lambda,\nu'}_{\mathbf{k}_{||},\mathbf{q}_{||},q_\perp}\sum_{\nu'',\mathbf{k}'_{||}} V^{\nu'\nu''\nu\nu''}_{|\mathbf{k}_{||}-\mathbf{q}_{||}-\mathbf{k}'_{||}|} f^{\nu''}_{\mathbf{k}'_{||}} \\
&+ f^{\lambda}_{\mathbf{k}_{||}} f^{\nu}_{\mathbf{k}_{||}-\mathbf{q}_{||}}\, i\hbar\,\mathcal{F}^{\lambda,\nu}_{\mathbf{k}_{||},\mathbf{q}_{||},q_\perp} + \sum_{\lambda',\nu',\mathbf{k}_{||}{}'} i\hbar\,\mathcal{F}^{\lambda',\nu'}_{\mathbf{k}'_{||},\mathbf{q}_{||},q_\perp}\Delta\langle a^\dagger_{\lambda',\mathbf{k}'_{||}} a^\dagger_{\nu,\mathbf{k}_{||}-\mathbf{q}_{||}} a_{\lambda,\mathbf{k}_{||}} a_{\nu',\mathbf{k}'_{||}-\mathbf{q}_{||}}\rangle \\
&- \left(1 - f^{\lambda}_{\mathbf{k}_{||}} - f^{\nu}_{\mathbf{k}_{||}-\mathbf{q}_{||}}\right) \\
&\cdot \left(i\hbar \sum_{q'_\perp}\mathcal{F}^{\lambda,\nu}_{\mathbf{k}_{||},\mathbf{q}_{||},q'_\perp}\Delta\langle\, (B^{\beta}_{\mathbf{q}_{||},q_\perp})^\dagger B^{\beta}_{\mathbf{q}_{||},q'_\perp}\,\rangle + \sum_{\mathbf{k}_{||}{}',\lambda',\nu'} V^{\lambda\nu'\nu\lambda'}_{|\mathbf{k}_{||}{}'-\mathbf{k}_{||}|}\Pi^{\lambda',\nu'}_{\mathbf{k}_{||}{}',\mathbf{q}_{||},q_\perp}\right) \\
&+ \frac{\partial}{\partial t}\Pi^{\lambda,\nu}_{\mathbf{k}_{||},\mathbf{q}_{||},q_\perp}\big|_{corr}\,.
\end{aligned} \tag{2.59}$$

Analogous to the SBEs, the single-particle energies $\epsilon^{\lambda}_{\mathbf{k}_{||}}$ and $\epsilon^{\nu}_{\mathbf{k}_{||}-\mathbf{q}_{||}}$ on the right hand side of the first line are renormalized by the corresponding terms in the second line.

The third line contains the spontaneous emission source term. In the first part of the spontaneous emission source term, $f^{\lambda}_{\mathbf{k}_{||}} f^{\nu}_{\mathbf{k}_{||}-\mathbf{q}_{||}}$ yields the condition that allows for photon-assisted polarizations to build up. To be more specific, this is possible when a hole and an electron exist simultaneously at wavevectors $\mathbf{k}_{||}$ and $\mathbf{k}_{||}-\mathbf{q}_{||}$. The second part of line three contains excitonic correlations $\Delta\langle a^\dagger_{\lambda',\mathbf{k}'_{||}} a^\dagger_{\nu,\mathbf{k}_{||}-\mathbf{q}_{||}} a_{\lambda,\mathbf{k}_{||}} a_{\nu',\mathbf{k}'_{||}-\mathbf{q}_{||}}\rangle$. This part is necessary to ensure the right lineshape of the luminescence spectrum and leads to an underestimation of the luminescence amplitudes if it is neglected. Hence, it is necessary to set up the equation of motion for the excitonic correlations and use a suitable truncation. This equation of motion and a discussion of the truncation, resulting in a treatment at the level of the second-Born Markov approximation, can be found in [[48]]. Line three of Eq. (2.59) shows that the onset of spontaneous emission takes place regardless of interactions with a light-field. Instead, it is dependent on the presence of excited charge carriers.

In the fifth line, the generalized photon-assisted Rabi frequency can be identified in the brackets which is multiplied by the phase-space filling factor given by the fourth line. The first term in the brackets in line five describes the stimulated emission contributions. These contributions are not negligible if strong fields are present, i.e. caused by optical microcavities.
In the sixth line, $\frac{\partial}{\partial t}\Pi^{\lambda,\nu}_{\mathbf{k}_{||},\mathbf{q}_{||},q_\perp}\big|_{corr}$ summarizes higher-order correlations from electron-electron and electron-phonon scattering processes. These are treated at the level of the second Born-Markov approximation .
The temporal evolution of the occupations is given by

$$\frac{\partial}{\partial t} f^{\lambda}_{\mathbf{k}_{||}} = -2Re\left(\sum_{\mathbf{q}_{||},q_\perp}\left(\mathcal{F}^{\lambda\nu}_{\mathbf{k}_{||}\mathbf{q}_{||},q_\perp}\right)^{*}\Pi^{\lambda,\nu}_{\mathbf{k}_{||},\mathbf{q}_{||},q_\perp}\right) \tag{2.60}$$

and

$$\frac{\partial}{\partial t} f^{\nu}_{\mathbf{k}_{||}} = -2Re\left(\sum_{\mathbf{q}_{||},q_\perp}\left(\mathcal{F}^{\lambda\nu}_{\mathbf{k}_{||}\mathbf{q}_{||},q_\perp}\right)^{*}\Pi^{\lambda,\nu}_{\mathbf{k}_{||}+\mathbf{q}_{||},q_\perp,\mathbf{q}_{||},q_\perp}\right). \tag{2.61}$$

When calculating the luminescence spectra presented in this thesis thermalized charge carriers were assumed. Because of this, Fermi-Dirac distributions were used instead solving Eq. (2.60) and Eq. (2.61).
Eqs. (2.57), (2.59), (2.60) and (2.61) represent the SLEs. The PL $S(\omega_{\mathbf{q}_{||},q_\perp})$ is obtained from the resonant part of the SLEs:

$$\begin{aligned} S(\omega_{\mathbf{q}_{||},q_\perp}) &= \frac{\partial}{\partial t}\Delta\langle\,(B^{\beta}_{\mathbf{q}_{||},q_\perp})^{\dagger}B^{\beta}_{\mathbf{q}_{||},q_\perp}\,\rangle \\ &= 2\,\mathrm{Re}\left(\sum_{\lambda,\nu,\mathbf{k}_{||}}\mathcal{F}^{\lambda\nu}_{\mathbf{k}_{||}\mathbf{q}_{||},q_\perp}\left(\Pi^{\lambda,\nu}_{\mathbf{k}_{||},\mathbf{q}_{||},q_\perp}\right)^{*}\right). \end{aligned} \tag{2.62}$$

As in case of the gain spectrum, fluctuations in quantum well widths and compositions can be taken into account by convolution of the PL spectrum with a Gaussian distribution.

2.5 Implementations

For the calculations framework of this thesis, the lowest conduction band, the heavy hole, light hole, and spin-orbit split-off hole band were explicitly considered. Since each band is twice-spin degenerate, this results in an 8×8 **k**·**p**-Hamiltonian. The heterostructures **k**·**p**-Hamiltonian has been obtained as described in Section 2.2.1. Necessary input are the layer compositions, layer widths and band offsets. Subsequently, the resulting eigenvalue problem is solved and the confinement wavefunctions and single-particle energies are calculated. The results are used to calculate the heterostructure's dipole and coulomb matrix elements. These matrix elements and the single-particle energies are input to the SBEs (Eq. (2.47)) and SLEs (Eq. (2.57) and Eq. (2.59)). From these, the absorption and PL are calculated via Eq. (2.53) and Eq. (2.62), respectively.
Further information can be found in the Appendix, where also typical parameters that were used for the **k**·**p**-calculations, the calculations of the optical properties and the DFT calculations are given.
All presented results obtained with DFT were calculated with the *Vienna Ab initio Simulation Package* (VASP) [[51–54]]. This package supplies various exchange-correlation functionals and makes use of the projector-augmented-wave method [[55, 56]].

Chapter 3

Ga(AsSb)/(InGa)As type-II structures

Laser emission from semiconductor heterostructures with type-II band alignment is of technological interest in different areas, e.g. for medical applications [[57]] or optical communication [[1]], and these structures have proven their usefulness in fundamental research [[10, 11]] as well. Modern society is particularly dependent on telecommunication. In modern telecommunication, internet communication and television and telephone signals are transmitted using optical fiber as waveguides (see [[58]] and references therein for examples). Fiber-optical communication requires emission wavelengths in the near-infrared where minima of absorption and dispersion of the used fiber-optic materials can be found around different wavelengths [[59]]. This causes different transmission windows to be used. One of these windows is given by the wavelength range of 1260 nm until 1360 nm and is called the *O-band* [[59]]. The research presented below mainly deals with wavelengths in the vicinity of the O-band.

As mentioned, the more established type-I heterostructures with bandgaps small enough for emission in the near-infrared suffer from significant Auger-losses as the wavelength increases [[2]]. Therefore, Auger recombination is a dominant loss mechanism in many of these heterostructures [[60]].

An alternative to type-I heterostructures is offered by type-II heterostructures. Type-II heterostructures are composed of nm-thick layers of different semiconductor materials grown on top of a substrate material. By suitably choosing a material combination, the electrons and holes are confined in different layers and light is emitted from electron-hole recombination across an internal interface. The layer into which excited charge carriers of the same

sign relax represents a sink in the potential to the carriers and is referred to as a *well*. The electron and hole well layers constitute the light emitting region, called the *active region*. The active region is embedded in barrier material, which can be utilized to guarantee confinement of the charge carriers and for other purposes, e.g. to avoid coupling between confined carriers from different active regions in the case of structures with multiple active regions.
In type-II structures, the spatial separation of electrons and holes leads to reduced electron-hole wavefunction overlap in comparison to type-I structures and thereby to reduced dipole strengths of optical transitions. The latter can be addressed by thoroughly optimizing the active regions of type-II heterostructures with regard to their optical properties.
In Section 3.1.1, type-II heterostructure design studies for laser emission close to 1200 nm will be discussed with a focus on the wells while in Section 3.1.2 the influence of the barrier material on the optical properties will be studied. In Section 3.1.3, type-II designs for an emission wavelength in the vicinity of 1300 nm will be studied.
Section 3.2 will present an experiment-theory investigation of the optical and terahertz (THz) properties of charge-transfer excitons in type-II heterostructures. Charge-transfer excitons are promising for the study of the internal interfaces properties in type-II heterostructures on a microscopic level.
The optical properties presented in this chapter were calculated with the microscopic theory presented in Section 2.4 and Section 2.2.

3.1 Design and optical characterization

As mentioned in Section 2.2.1, the confinement potential, which is described by the alignment of the valence band and conduction band edges from the different layers, causes the formation of confinement levels and subbands. In quantum well heterostructures, the transition energy of the fundamental transition depends on the energies of the lowest electron and lowest hole confinement levels, which can be influenced by the heterostructure design. This will be considered later.
As an example, Fig 3.1 shows the confinement potential at room temperature of a type-II heterostructure with (InGa)As electron wells and Ga(AsSb) hole wells and GaAs barriers for two different sheet carrier densities. Dashed black lines show the confinement potential for a sheet carrier density of $3.0{\cdot}10^{12}/\mathrm{cm}^2$, whereas the colored lines show the confinement potential for

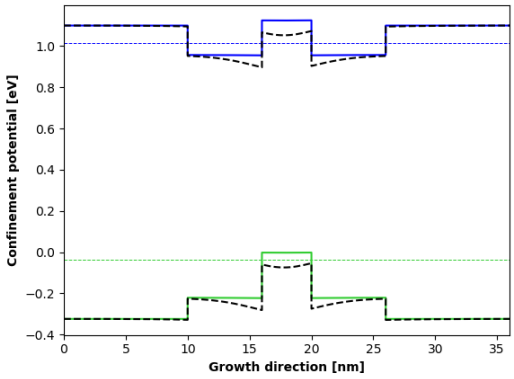

Figure 3.1: Confinement potential in growth direction at 300 K of a $GaAs_{0.8}Sb_{0.2}/In_{0.2}Ga_{0.8}As$ heterostructure with 10 nm GaAs barriers and 6 nm and 4 nm $In_{0.2}Ga_{0.8}As$ and $GaAs_{0.8}Sb_{0.2}$ wells, respectively. The solid blue line and solid green line give the conduction band and valence band edges, respectively, at a sheet carrier density of $0.1{\cdot}10^{12}/cm^2$. The dashed black lines give the band edges at a carrier density of $3{\cdot}10^{12}/cm^2$. The energies of the lowest confinement levels at a sheet carrier density of $0.1{\cdot}10^{12}/cm^2$ are given by the horizontal dashed colored lines.

a sheet carrier density of $0.1{\cdot}10^{12}/cm^2$. The dashed colored lines give the energetic locations of the lowest (or first) electron (blue) and lowest hole (green) confinement levels at a sheet carrier density of $0.1{\cdot}10^{12}/cm^2$.
In contrast to the confinement potential at the lower sheet carrier density, it can be seen from Fig 3.1 that the confinement potential at a sheet carrier density of $3.0{\cdot}10^{12}/cm^2$ is significantly deformed by the Coulomb attraction of the spatially separated electrons and holes. As a result, at high sheet carrier densities the electron-hole wavefunction overlap is increased in comparison to low sheet carrier densities.

3.1.1 Heterostructure design for emission around 1200 nm

Besides the emission wavelength, the temperature at which reliable laser operation is possible can in practice set limits to the application area of a laser.
For near-infrared laser applications at room temperature, (InGa)As and Ga(AsSb) based type-II heterostructures have proven to be promising [[14,

61]]. Nevertheless, realized laser structures exhibited disadvantageously low optical output powers of 140 mW per facet [[14]] or even lasing from a type-I transition instead of type-II [[61]]. This indicated the need for further optimization.

Optimizations that increase the wavefunction overlap of the first electron and first hole state in type-II structures aim to increase the type-II transition strength. For a structure composed of (InGa)As and Ga(AsSb) wells, an efficient possibility to achieve this is the addition of another (InGa)As well instead of using a bi-layer structure. This is done in such a way that the (InGa)As wells surround the Ga(AsSb) well. Structures using such a design are called *"W"-structures* since the conduction band edge alignment looks like a stylized W, as can be seen in Fig. 3.1 (solid blue line).

"W"-heterostructures with (InGa)As and Ga(AsSb) wells are the objects of investigation in this chapter. For all presented calculations of the optical properties in this thesis, the charge carrier capture was not modeled but a certain sheet carrier density in the wells was used instead.

In the context of optimizing the optical emission properties of (InGa)As and Ga(AsSb) based "W"-heterostructures, structures with either equal electron and hole well widths or unequal well widths were studied. In each case, In and Sb concentrations of 20% were used which results in emission wavelengths close to the O-band and 10 nm GaAs barriers were used to guarantee a proper decay of the charge carrier wavefunctions within these.

Fig. 3.2 shows the calculated PL and gain (absorption) spectra for these structures while the corresponding emission wavelengths and the increased emission strength are given in Table 3.1. At this, the emission strength of the structure from the first row is considered to be 100%. The labeling of the structures refers to the well width as explained later. Sheet carrier densities of $0.1{\cdot}10^{12}/\mathrm{cm}^2$ and $3.0{\cdot}10^{12}/\mathrm{cm}^2$ were used to calculate the low-density PL spectra at 300 K and high-density gain (absorption) spectra at 300 K (solid lines) and 350 K (dashed lines).

Within this thesis, the absorption spectra are generally referred to as gain in the text since negative absorption constitutes gain which yields the laser light. Nevertheless, in figures the absorption is presented as it has been obtained from the calculations and not the gain as the negative of the absorption.

The labeling of the structures in Fig. 3.2 and Table 3.1 was done in the following way: a number 'X' followed by 'nm' labels structures with equal well widths while 'In' or 'Sb' followed by 'X nm' labels the width of the $In_{0.2}Ga_{0.8}As$ or $GaAs_{0.8}Sb_{0.2}$ well. In cases where only one well width is addressed, the wells that do not have a specified width have widths of 6 nm

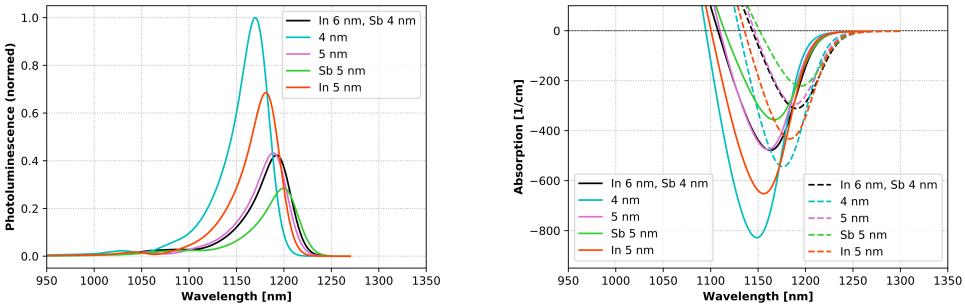

Figure 3.2: PL (left) and absorption (right) spectra of the structures labeled in the legends. The labeling is explained in the text. A sheet carrier density of $0.1{\cdot}10^{12}/\mathrm{cm}^2$ was used for calculations of the 300 K PL spectra. The PL spectra are normed to the maximum of the PL from structure '4 nm'. For calculations of the 300 K (solid lines) and 350 K (dashed lines) absorption spectra, a sheet carrier density of $3.0{\cdot}10^{12}/\mathrm{cm}^2$ was used.

Structure	$\lambda_{\mathbf{PL}}^{\mathbf{300\,K}}$ [nm], **increase**	$\lambda_{\mathbf{gain}}^{\mathbf{350\,K}}$ [nm], **increase**	$\lambda_{\mathbf{gain}}^{\mathbf{300\,K}}$ [nm], **increase**
Sb 5 nm	1199.6, +0%	1194.7, +0%	1167.2, +0%
In 6 nm, Sb 4 nm	1192.4, +49%	1190.4, +40%	1162.8, +34%
5 nm	1188.7, +52%	1188.4, +33%	1160.6, +34%
In 5 nm	1181.1, +141%	1183.5, +95%	1156.0, +83%
4 nm	1169.9, +251%	1176.2, +145%	1148.8, +132%

Table 3.1: Emission wavelengths and increase of the emission strengths of "W"-heterostructures with $In_{0.2}Ga_{0.8}As$ and $GaAs_{0.8}Sb_{0.2}$ wells of different width and 10 nm GaAs barriers. The labeling of the structures is explained in the text. The increase in emission strength is given relative to 'structure Sb 5 nm', the emission of which is considered to be 100%.

in case of an $In_{0.2}Ga_{0.8}As$ well or 4 nm in case of a $GaAs_{0.8}Sb_{0.2}$ well. Among the investigated structures, the lowest PL and gain emission strengths were calculated for structure 'Sb 5 nm' (green curves) where two 6 nm $In_{0.2}Ga_{0.8}As$ electron wells and a 5 nm $GaAs_{0.8}Sb_{0.2}$ hole well were used. Since this is the structure with the widest electron and hole wells, this was expected because wider wells lead to lower electron-hole wavefunction overlap and consequently to lower transition probabilities. Moreover, the wide wells of this structure cause the confinement levels to be comparatively low in energy. This results in the longest PL and gain emission wavelengths among the considered structures. On the other hand, the strongest gain

and PL emission has been calculated for structure '4 nm', which is the structure with the thinnest wells. Since thinner wells cause energetically higher confinement levels, this leads to a blue-shifted emission compared to the emission of structure 'Sb 5 nm'. For example, the wavelengths of the PL peak of structure '4 nm' is blue-shifted by 29.7 nm in comparison to the PL peak of structure 'Sb 5 nm'. Structure 'In 5 nm' with 5 nm $In_{0.2}Ga_{0.8}As$ wells and a 4 nm $GaAs_{0.8}Sb_{0.2}$ well yields the second strongest emission and has a blue-shifted PL peak by 18.5 nm relative to that of structure 'Sb 5 nm'. Very similar optical properties were obtained for the structures '5 nm' and 'In 6 nm, Sb 4 nm'. While the structure '5 nm' yields a slightly stronger low-density PL emission, at high charge carrier densities the structures yield approximately equally strong gain emissions at 300 K. However, at 350 K the gain emission of structure 'In 6 nm, Sb 4 nm' slightly exceeds that of structure 'Sb 5 nm'. Here, the gain spectra of structure '5 nm' are blue-shifted by 2 nm compared to that of structure 'In 6 nm, Sb 4 nm'.
Overall, thinner wells cause a considerably stronger emission as well as a blue-shift of the emission. The latter needs to be balanced by adjusting the Sb and In concentrations. The structures 'In 6 nm, Sb 4 nm' and '5 nm' represent good compromises for the well widths with regards to emission strengths and emission wavelengths close to 1200 nm.
The minor shifts of the emission wavelengths that were observed for the calculated 300 K PL spectra and 350 K gain spectra (see Table 3.1) can be advantageous for the following reason. In general, PL measurements can be used to monitor the successful growth of the active region. For optically pumped laser devices, like vertical-external-cavity surface-emitting lasers (VECSELs[1]), it is reasonable to expect a heating up by 50 K during room temperature operation due to the optical excitation [[63]]. In case of a minor shift between the 300 K PL and 350 K gain emission wavelengths, monitoring the successful growth of the active region by PL measurements allows for a direct conclusion on the lasing wavelength.

The collaboration of our group with the experimental physics group of W. Stolz resulted in successful realizations of type-II laser structures. An example for this is a 930 μm long single "W"-quantum well electrical injection laser using the layout of structure 'In 6 nm, 4 nm' for the active region. To be more specific: a 4 nm wide $GaAs_{0.8}Sb_{0.2}$ hole well embedded between two 6 nm wide $In_{0.2}Ga_{0.8}As$ electron wells were used which were adjacent to GaAs barriers [[9]].

[1] An introduction to the physics of VECSELs can for example be found in [[62]].

For this laser structure, room temperature measurements of the optical output pulse power per facet as a function of the current density (Fig.1 in [[9]]) revealed a low threshold current density of 0.4 kA/cm^2. At the threshold current density the losses are exactly balanced by the gain and above it laser operation takes place. The 930 μm long laser structure was optically

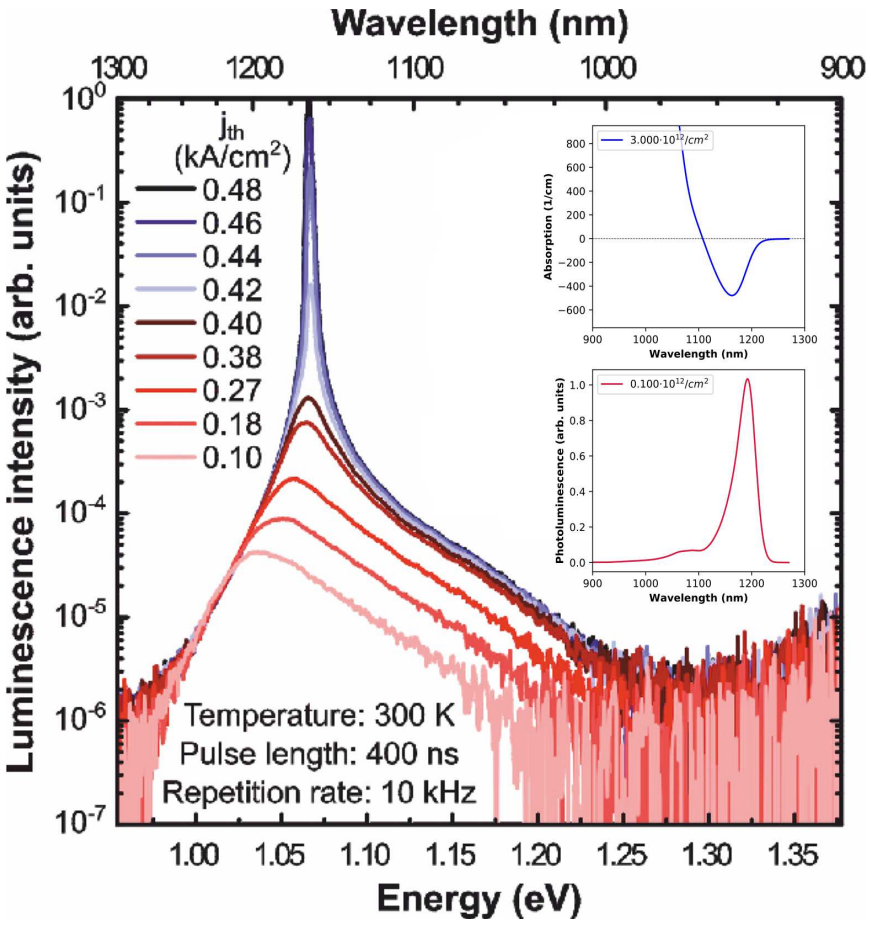

Figure 3.3: Measured electroluminescence spectra of a 930 μm long laser bar, with the active region that is specified in the text, at room temperature. The insets show the calculated room temperature absorption spectrum at a sheet carrier density of $3.0{\cdot}10^{12}$/cm^2 (upper picture) and PL spectrum at a sheet carrier density of $0.1{\cdot}10^{12}$/cm^2 (lower picture). This figure is based on Fig. 2 in [[9]].

characterized by electroluminescence (EL) spectroscopy. Here, the radiative recombination of injected charge carriers causes light-emission. Whereas at low current densities that are well below the threshold current density the EL spectra dominantly stem from spontaneous emission, at current densities that are above the threshold current density the spectra dominantly stem from stimulated emission. Hence, at low injection current densities the EL emission wavelength is expected to agree with the emission wavelength calculated for the 300 K PL at low sheet carrier densities, whereas at injection current densities above the threshold current density the EL emission wavelength is expected to agree with the calculated emission wavelength of the 300 K gain at high sheet carrier densities.
Fig. 3.3 shows the laser structure's EL spectra dependent on the color coded injection current density along with the calculated PL and gain spectra for sheet carrier densities of $0.1{\cdot}10^{12}/\mathrm{cm}^2$ (red curve) and $3.0{\cdot}10^{12}/\mathrm{cm}^2$ (blue curve), respectively, in the insets. As can be seen from Fig. 3.3, the theoretically predicted 300 K PL emission wavelength of 1192.4 nm (see Table. 3.1, 'In 6 nm, 4 nm') is in agreement with the EL emission wavelengths at low injection current densities of 0.10 $\mathrm{kA/cm}^2$ and 0.18 $\mathrm{kA/cm}^2$. Above the threshold current density of 0.4 $\mathrm{kA/cm}^2$, the EL emission wavelengths are in agreement with the theoretically predicted 300 K gain emission wavelength of 1162.8 nm (see Table. 3.1, 'In 6 nm, 4 nm'). At all current densities, no indication of lasing from a type-I transition was observed.
Besides the above mentioned low threshold current density of 0.4 $\mathrm{kA/cm}^2$, the 930 μm long laser structure exhibited a high differential efficiency of 66%, pump-limited maximum optical output powers of 1.4 W per facet, and low internal losses of 1.9 cm^{-1} [[9]]. These results demonstrate the suitability of (InGa)As/Ga(AsSb) "W"-structures for near-infrared laser applications at room temperature.

3.1.2 Impact of the barrier material

To further optimize the optical properties of (InGa)As and Ga(AsSb) based "W"-structures the impact of the barrier material was investigated, since the barriers impose localization to the charge carriers. For this purpose, the active region constructed of 6 nm $\mathrm{In_{0.2}Ga_{0.8}As}$ and 4 nm $\mathrm{GaAs_{0.8}Sb_{0.2}}$ wells was used and the 10 nm GaAs barriers were replaced either by $\mathrm{Al}_x\mathrm{Ga}_{1-x}\mathrm{As}$, with x=0.1 or 0.2, or monolayers of $\mathrm{GaP_{0.5}As_{0.5}}$ were introduced between the 10 nm GaAs barrier and the $\mathrm{In_{0.2}Ga_{0.8}As}$ wells. The monolayers were modeled by 0.5 nm-layers of $\mathrm{GaP_{0.5}As_{0.5}}$.

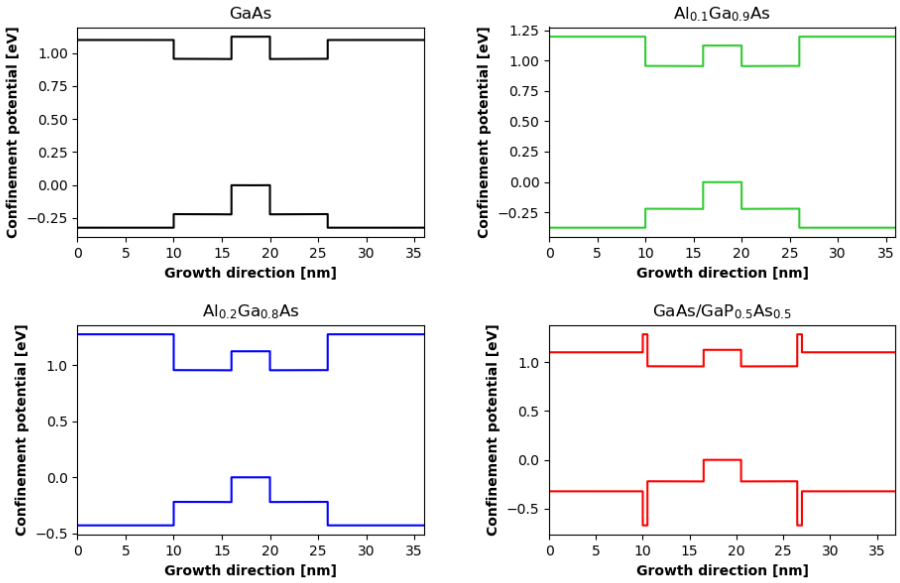

Figure 3.4: Confinement potentials of heterostructures with an active region consisting of a 4 nm wide $GaAs_{0.8}Sb_{0.2}$ well embedded in two 6 nm wide $In_{0.2}Ga_{0.8}As$ wells. The titles refer to the varying barrier materials. While GaAs, $Al_{0.1}Ga_{0.9}As$ and $Al_{0.2}Ga_{0.8}As$ refer to 10 nm of each material embedding the active region, the title $GaAs/GaP_{0.5}As_{0.5}$ refers to barriers consisting of 10 nm GaAs combined with a monolayer of $GaP_{0.5}As_{0.5}$ adjacent to each electron well.

Fig. 3.4 shows the confinement potentials for combinations of the above mentioned active region and barrier materials. In comparison to the use of GaAs barriers (black lines), the modified barriers (colored lines) introduce a larger potential difference to the confinement potential at the (InGa)As well-barrier interface and thereby increase the confinement of charge carriers in the active region.

Hence, different barrier designs result in differences in the electron-hole wavefunction overlap of the lowest states which can be seen in Fig. 3.5. Here, the lowest electron and hole wavefunctions are displayed for a sheet carrier density of $0.1{\cdot}10^{12}/\mathrm{cm}^2$ and a temperature of 300 K. Light-gray shaded areas mark the electron wells and dark-gray ones the hole wells. The shape of the electron and hole wavefunctions differ of course. While the coupled electron

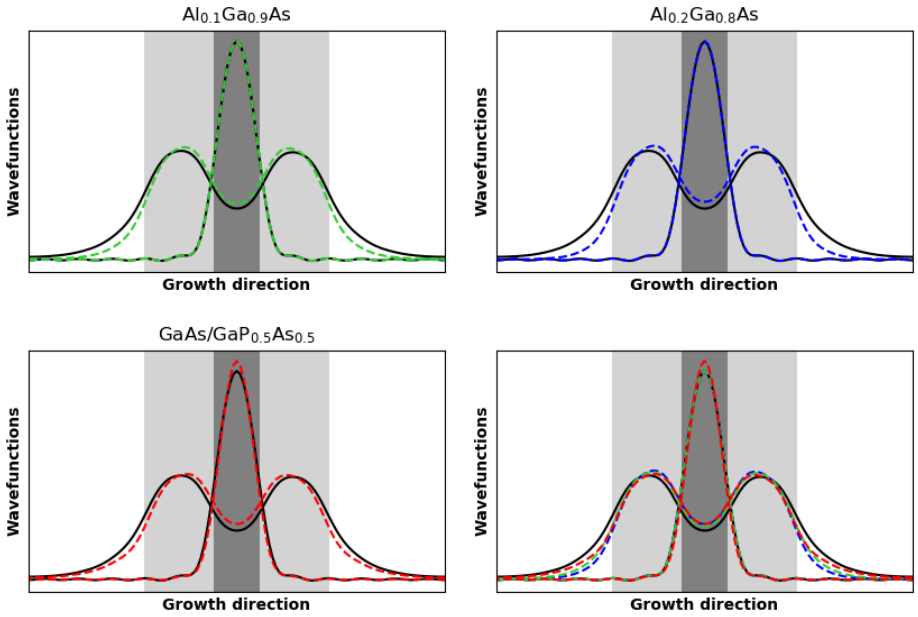

Figure 3.5: First electron and first hole wavefunctions along growth direction (centered on the hole well) at 300 K and for a sheet carrier density of $0.1{\cdot}10^{12}/\mathrm{cm}^2$. Light-gray shaded areas mark the electron wells and dark-gray areas the hole wells. The titles link the barrier material to the colors of the wavefunctions. The titles are explained in the caption of Fig. 3.4. To facilitate comparison, the lower right part shows all wavefunctions in one picture.

wavefunctions show two maxima where one is located in each electron well, with a minimum in between, the hole wavefunctions have a single maximum located in the hole well. As can be seen when comparing the heights of the electron wavefunctions minima, the probability for the electrons to be found in the Ga(AsSb)-layer is increased (dashed colored lines) for barrier materials differing from GaAs (solid black lines). Whereas in case of structures with $\mathrm{Al}_x\mathrm{Ga}_{1-x}\mathrm{As}$ barriers the hole wavefunctions (dashed green and blue lines) remain basically unchanged from the structure with GaAs barriers (black solid lines), in case of $\mathrm{GaAs/GaP}_{0.5}\mathrm{As}_{0.5}$ barriers the hole wavefunction has a slightly narrower width and a higher maximum. For easier comparison, the lower right part of Fig. 3.5 shows the wavefunctions from all structures with different barriers together in one plot. As can be

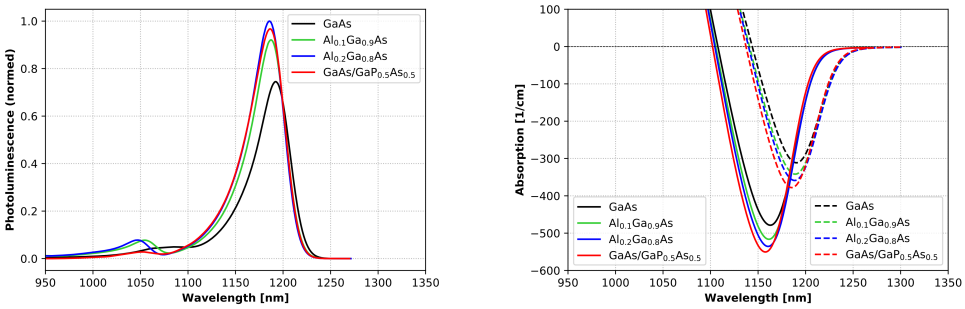

Figure 3.6: Photoluminescence (left) and absorption (right) spectra of "W"-structures with two 6 nm $In_{0.2}Ga_{0.8}As$ wells, a 4 nm $GaAs_{0.8}Sb_{0.2}$ and different barriers. The PL was calculated at 300 K for a sheet carrier density of $0.1{\cdot}10^{12}/cm^2$ and the absorption was calculated at 300 K (solid lines) and 350 K (dashed lines) for a sheet carrier density of $3.0{\cdot}10^{12}/cm^2$. The legend labels the barrier material as explained in the caption of Fig. 3.4. The PL spectra are normed to the maximum of the PL from structure '$Al_{0.2}Ga_{0.8}As$'.

seen from this, higher barriers lead to an increased wavefunction overlap. Fig. 3.6 shows the structures 300 K PL spectra at a sheet carrier density of $0.1{\cdot}10^{12}/cm^2$ along with the 300 K and 350 K gain spectra at a sheet carrier density of $3.0{\cdot}10^{12}/cm^2$. Whereas the calculated low density PL of the structure with $Al_{0.2}Ga_{0.8}As$ barriers is the strongest, the calculated gain of the structure with $GaAs/GaP_{0.5}As_{0.5}$ barriers is the strongest. The second strongest gain emission stems from the structure with $Al_{0.2}Ga_{0.8}As$ barriers. Thus, the increased wavefunction overlap increases the emission strength, as expected.

In comparison to the spectra that were calculated for the structure with GaAs barriers, the higher potential jump at the (InGa)As well-barrier interfaces of the other structures causes a slight blue-shift of the emission wavelengths and increases the emission strengths. To facilitate comparison, the emission wavelengths and the increase of the emission strengths in % are summarized in Table 3.2. Here, the increase in emission strength is given relative to the structure with GaAs barriers, for which the emission is considered to be 100%.

While the use of the higher barriers results in stronger emission strengths, in practice it is generally not possible to use arbitrarily high barriers for any laser structure and excitation conditions. E. g., for optically pumped

Structure	$\lambda_{\mathbf{PL}}^{\mathbf{300\,K}}$ [nm], **increase**	$\lambda_{\mathbf{gain}}^{\mathbf{350\,K}}$ [nm], **increase**	$\lambda_{\mathbf{gain}}^{\mathbf{300\,K}}$ [nm], **increase**
GaAs	1192.4, +0%	1190.4, +0%	1162.8, +0%
$Al_{0.1}Ga_{0.9}As$	1187.6, +24%	1189.3, +8%	1161.2, +10%
$Al_{0.2}Ga_{0.8}As$	1185.7, +34%	1188.5, +15%	1160.4, +12%
$GaAs/GaP_{0.5}As_{0.5}$	1187.0, +30%	1185.5, +21%	1157.6, +15%

Table 3.2: Emission wavelengths and increase of the emission strengths of $In_{0.2}Ga_{0.8}As/GaAs_{0.8}Sb_{0.2}$ "W"-heterostructures with different barriers. The increase in emission strength is given relative to the structure with GaAs barriers, the emission of which is considered to be 100%.

laser systems and non-resonant excitation of the carriers into barrier states, the bandgap of the (AlGa)As-barriers must be matched with the excitation energy of the pump-laser. Therefore, this can impose limitations to the Al content used in the barriers. Moreover, the carrier capture has not been modeled in the presented studies. Instead, a certain sheet carrier density in the well has been assumed. Because of this, this study does not reflect the impact of the $GaP_{0.5}As$ monolayers on the charge carrier capture.

3.1.3 Wavelength extension towards 1300 nm

With regards to optimizing the emission strength while extending the emission wavelength, the dependence of the emission strengths on the In and Sb contents in the wells was studied. For this purpose, the gain spectra of seven active regions in total with an electron well width of 6 nm, a hole well width of 4 nm and 350 K gain emission wavelengths close to 1200 nm (blue curves), 1300 nm (yellow and green curves) or 1350 nm (orange and brown curves) were calculated. Fig. 3.7 shows these gain spectra at 300 K (dash-dotted and solid lines) and 350 K (dotted and dashed lines) for a sheet carrier density of $3.0{\cdot}10^{12}/cm^2$. The percentages of In and Sb in the (InGa)As electron wells and Ga(AsSb) hole wells are given in the color coded legend. Here, the results from the structure with 20% In and Sb are the ones that have already been presented in Sections 3.1.1 and 3.1.2.
Table 3.3 lists the gain emission wavelengths together with the increase of the gain emission strengths in % relative to the lowest emission at a comparable wavelength. As can be seen from Fig. 3.7 and Table 3.3, when optimizing the gain properties it is advantageous to achieve longer wavelengths by increasing the Sb content in the Ga(AsSb)-layer rather than increasing the In content in the (InGa)As-layer.

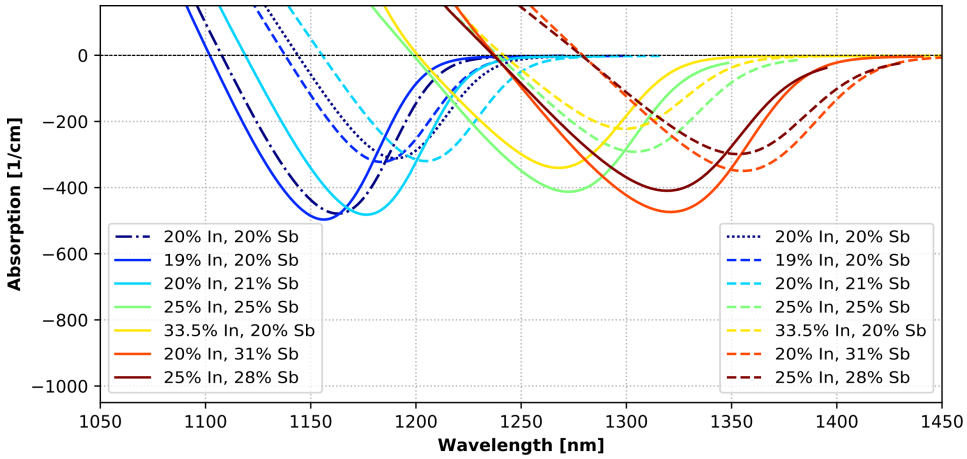

Figure 3.7: Absorption spectra of (InGa)As/Ga(AsSb) "W"-structures with a 4 nm Ga(AsSb) well embedded between two 6 nm (InGa)As wells and 10 nm GaAs barriers at a sheet carrier density of $3.0{\cdot}10^{12}/\mathrm{cm}^2$. Solid lines and the dash-dotted line show the gain spectra at 300 K. Dashed lines and the dotted line show the gain spectra at 350 K. The legend gives the percentages of In and Sb in the (InGa)As-layer and Ga(AsSb)-layer, respectively.

A) Structure	$\lambda_{\mathbf{gain}}^{\mathbf{350\,K}}$ [nm], **increase**	$\lambda_{\mathbf{gain}}^{\mathbf{300\,K}}$ [nm], **increase**
25% In, 28% Sb	1352.9, +0%	1319.3, +0%
20% In, 31% Sb	1355.3, +17%	1321.0, +16%
B) Structure	$\lambda_{\mathbf{gain}}^{\mathbf{350\,K}}$ [nm], **increase**	$\lambda_{\mathbf{gain}}^{\mathbf{300\,K}}$ [nm], **increase**
33.5% In, 20% Sb	1299.2, +0%	1267.7, +0%
25% In, 25% Sb	1304.0, +31%	1272.3, +21%
C) Structure	$\lambda_{\mathbf{gain}}^{\mathbf{350\,K}}$ [nm], **increase**	$\lambda_{\mathbf{gain}}^{\mathbf{300\,K}}$ [nm], **increase**
20% In, 20% Sb	1190.4, +0%	1162.8, +0%
19% In, 20% Sb	1183.5,+4%	1156.3,+4%
20% In, 21% Sb	1204.7, +1%	1176.5, +3%

Table 3.3: Emission wavelengths of "W"-structures with 10 nm GaAs barriers, 6 nm (InGa)As wells and 4 nm Ga(AsSb) wells together with the increase of the emission relative to the structure with the lowest emission at a comparable wavelength. The names of the structures give the percentage of In and Sb in the wells.

In practice, it has to be taken into consideration that reducing the In content is accompanied by lowering the electron well depths and that the increase of the Sb content is limited by the ability to produce high quality layers at aimed contents.

So far, the energetic locations of the confinement levels have not been considered. Layouts with 6 nm wide electron wells and 4 nm wide hole wells cause the first and second electron energy levels to be energetically very close. For the structures considered in the framework of this thesis, these well widths result in a first and second electron confinement level separation by about 10 meV. At high charge carrier densities and temperatures, this favors lasing from higher order type-II transitions. Hence, in order to guarantee lasing from the fundamental electron-hole transition, the separation of the first and second electron levels can be increased by decreasing the (InGa)As well width and subordinately the Ga(AsSb) well width.

Table 3.4 gives the distance of the first and second electron confinement

Structure	**(InGa)As well width** [nm]	**Ga(AsSb) well width** [nm]	**distance of e2 and e1 level** [meV]
Ref	6	4	8
In-1.5	4.5	4	15
In-1.5, Sb-0.5	4.5	3.5	19
In-2.5	3.5	4	20
In-2.5, Sb-0.5	3.5	3.5	23

Table 3.4: First electron and first hole confinement level distance of $In_{0.25}Ga_{0.75}As/GaAs_{0.72}Sb_{0.28}$ "W"-structures with GaAs barriers at a sheet carrier density of $0.1{\cdot}10^{12}/cm^2$ and at 300 K. The labeling of the structures is explained in the text.

levels for different electron and hole well widths at a sheet carrier density of $0.1{\cdot}10^{12}/cm^2$ and 300 K. For all calculations, $In_{0.25}Ga_{0.75}As$ electron wells and $GaAs_{0.72}Sb_{0.28}$ hole wells and 10 nm GaAs barriers have been used. In Table 3.4, structure 'Ref' has layer lengths of 6 nm for the $In_{0.25}Ga_{0.75}As$ well and 4 nm for the $GaAs_{0.72}Sb_{0.28}$ well. The naming of the other structures labels the corresponding shortened layer by indicating the (InGa)As or Ga(AsSb) well with 'In' or 'Sb', respectively, followed by a number which gives the reduction of the respective width length in nm. As can be seen in Table 3.4, the distance of the first and second electron confinement levels is primarily influenced by the width of the electron wells (see results from 'Ref', 'In-1.5' and 'In-2.5'). The thickness of the hole well noticeably affects this energy difference (compare results from 'In-1.5' and 'In-2.5' to results

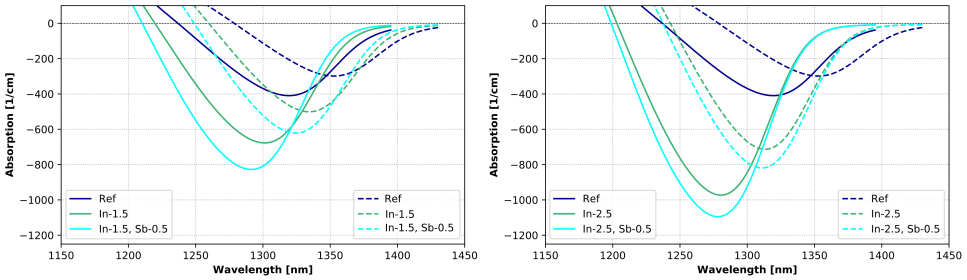

Figure 3.8: Absorption spectra of the $In_{0.25}Ga_{0.75}As/GaAs_{0.72}Sb_{0.28}$ "W"-structures from Table 3.4 at a sheet carrier density of $3.0{\cdot}10^{12}/cm^2$ and at 300 K (solid lines) and 350 K (dashed lines). The structures are grouped according to their $In_{0.25}Ga_{0.75}As$ well width (left: 6 nm and 4.5 nm; right: 6 nm and 3.5 nm). The legends label all well width as explained in the text.

from 'In-1.5, Sb-0.5' and 'In-2.5, Sb-0.5') as well.
Fig. 3.8 shows the calculated gain spectra of the structures from Table 3.4 at a sheet carrier density of $3.0{\cdot}10^{12}/cm^2$ and 300 K (solid lines) and 350 K (dashed lines). The 300 K gain spectrum of the structure with 6 nm wide $In_{0.25}Ga_{0.75}As$ and 4 nm wide $GaAs_{0.72}Sb_{0.28}$ wells ('Ref') is centered around 1319 nm, whereas the gain spectrum of the structure with the largest first and second electron confinement level distance ('In-2.5, Sb-0.5') is centered around 1278 nm at the same temperature. Hence, for an emission close to 1300 nm, the upwards shift of the fundamental transition energy needs to be compensated by adjusting the Sb and In concentrations in the wells in case of the latter structure.

Altogether, the largest effect on the emission strength can be achieved by using thin layers for the wells. This increases the first electron and first hole wavefunction overlap by forcing the charge carriers to be confined in narrower regions. Furthermore, relatively low In contents in the electron well and a large potential step at the electron well-barrier interfaces increases the wavefunction overlap and the carrier confinement in the active region and therefore the transition probability.
Apart from this, graded electron-hole well interfaces can be beneficial when optimizing the gain emission strength [[63, 64]]. The gradients can be modeled by 1 nm thick quaternary $In_xGa_{1-x}As_{1-y}Sb_y$ layers [[63]]. In doing so, one starts from the electron wells moving in the direction towards the hole well and linearly decreases the In content while the Sb content is linearly

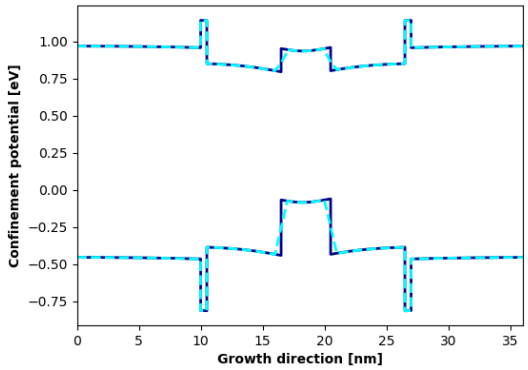

Figure 3.9: Confinement potential of 6 nm (InGa)As/4 nm Ga(AsSb) "W"-structures with GaAs barriers and $GaP_{0.5}As_{0.5}$ monolayers at 300 K and at a sheet carrier density of $3.0{\cdot}10^{12}/cm^2$. The solid lines belong to a structure with rectangular confinement potential and the dashed lines belong to a structure with graded interfaces between the electron and hole wells.

increased. More specifically, the In content decreases from the value x_e used in the $In_{x_e}Ga_{1-x_e}As$ electron well to zero while the Sb content linearly increases from zero to the Sb content y_h used in the $GaAs_{1-y_h}Sb_{y_h}$ hole well. For illustration, Fig. 3.9 shows confinement potentials of structures with (dashed light-blue lines) and without (solid blue lines) graded interfaces between the wells at 300 K and a sheet carrier density of $3.0{\cdot}10^{12}/cm^2$.
Fig 3.10 shows the 300 K and 350 K gain spectra at a sheet carrier density of $3.0{\cdot}10^{12}/cm^2$ for both previously mentioned structures (light-blue and blue curves) and two other structures (green and orange curves). The structures combine aspects of the above mentioned approaches for gain optimization.
Table 3.5 contains the layer lengths and compositions of the structures from Fig. 3.10. The spectra in Fig. 3.10 show that graded interfaces enhance the gain (compare light-blue curves to blue curves), but the strongest enhancement results from thinner wells (compare light-blue curves to green curves). While the structure 'In 4 nm, graded Sb 4 nm, $GaAs/GaP_{0.5}As_{0.5}$' which combines the use of thin wells, relatively low In content, modified barriers and graded interfaces between the wells, yields the strongest gain, the gain properties of structure 'In 3.5 nm, Sb 3.5 nm, GaAs' are remarkable as well. For the latter structure, only thinner wells were used. Comparing the 300 K gain of these two structures, the emission strength of structure 'In 4 nm,

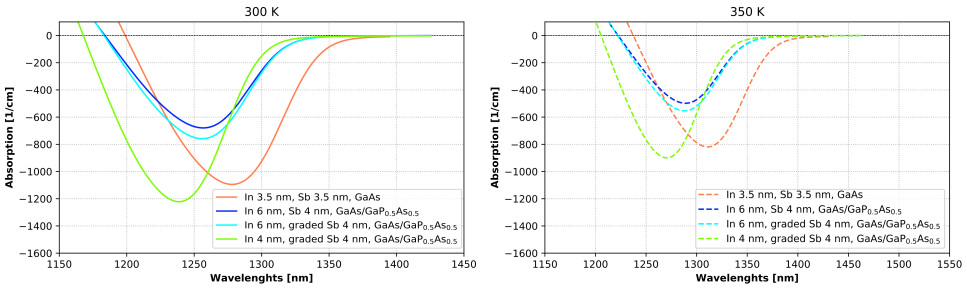

Figure 3.10: Absorption spectra of "W"-structures with emission wavelengths close to 1300 nm at 300 K (left) and 350 K (right) and for a sheet carrier density of $3.0{\cdot}10^{12}/\mathrm{cm}^2$. The legends refer to the layouts of the active regions that are specified in Table 3.5.

Structure	**(InGa)As well, % In, width**	**Ga(AsSb) well, % Sb, width**
In 6 nm, Sb 4 nm, GaAs/$GaP_{0.5}As_{0.5}$	15%, 6 nm	30%, 4 nm
In 6 nm, graded Sb 4 nm, GaAs/$GaP_{0.5}As_{0.5}$	15%, 6 nm (graded IF)	30%, 4 nm (graded IF)
In 3.5 nm, Sb 3.5 nm, GaAs	25%, 3.5 nm	28%, 3.5 nm
In 4 nm, graded Sb 4 nm, GaAs/$GaP_{0.5}As_{0.5}$	15%, 4 nm (graded IF)	30%, 4 nm (graded IF)

Structure	**Barrier, width**
In 6 nm, Sb 4 nm, GaAs/$GaP_{0.5}As_{0.5}$	GaAs, 10 nm, $GaP_{0.5}As_{0.5}$, 0.5 nm
In 6 nm, graded Sb 4 nm, GaAs/$GaP_{0.5}As_{0.5}$	GaAs, 10 nm, $GaP_{0.5}As_{0.5}$, 0.5 nm
In 3.5 nm, Sb 3.5 nm, GaAs	GaAs, 10 nm
In 4 nm, graded Sb 4 nm, GaAs/$GaP_{0.5}As_{0.5}$	GaAs, 10 nm, $GaP_{0.5}As_{0.5}$, 0.5 nm

Table 3.5: Layout of the (InGa)As/Ga(AsSb) "W"-structures used for the calculation of the gain spectra in Fig. 3.10. In this table, the word 'interface' is abbreviated as 'IF'.

graded Sb 4 nm, GaAs/$GaP_{0.5}As_{0.5}$' exceeds that of structure 'In 3.5 nm, Sb 3.5 nm, GaAs' by 12%.

The dependence of the gain on the sheet carrier density of structure 'In 4 nm, graded Sb 4 nm, GaAs/$GaP_{0.5}As_{0.5}$' was studied in more detail. Fig. 3.11 shows the gain of the structure at 300 K dependent on the sheet carrier density. The gain emission strength of this structure at a sheet carrier density of $2.0{\cdot}10^{12}/\mathrm{cm}^2$ (calculated maximum gain value: 591/cm) already exceeds that of the structure 'In 6 nm, Sb 4 nm' from Table 3.1 with 20% In and Sb at the same temperature but at a higher density of $3.0{\cdot}10^{12}/\mathrm{cm}^2$ (calculated maximum gain value: 479/cm).

Thus, combining the different approaches for gain optimization shows promise for the achievement of good gain values at low carrier densities.

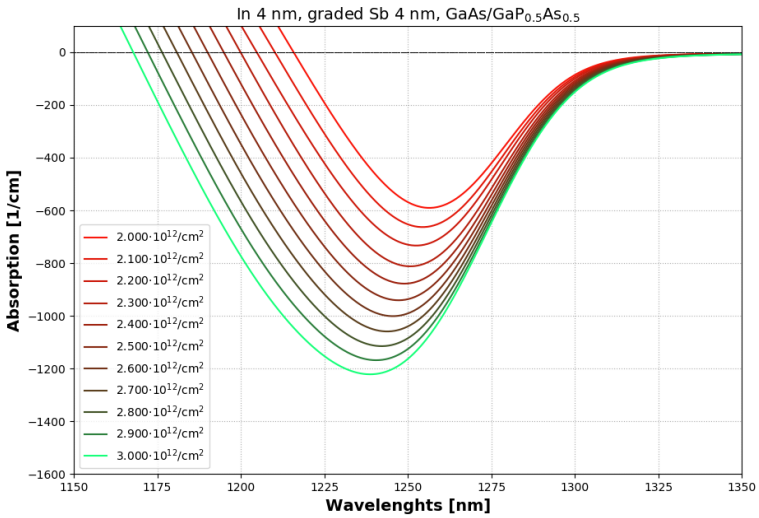

Figure 3.11: Sheet carrier density dependent absorption spectra at 300 K of structure 'In 4 nm, graded Sb 4 nm, $GaAs/GaP_{0.5}As_{0.5}$' from Table 3.5.

However, the limits of practical realization must be taken into account. For example, the theoretical consideration of a regularly graded interface between the wells is an idealized model that can hardly be met in experiments. Moreover, it can be disadvantageous for the layer-quality to achieve a certain wavelength by primarily raising the Sb content while keeping the In content low. Also, in order to achieve strong gain, it is generally preferable to use thin electron and hole wells.

As a result from further calculations that were carried out in our group and from the studies presented in this section an electrical injection laser with emission wavelengths close to 1300 nm was fabricated [[4]]. For this laser, a double "W"-layout was used where one "W" consists of 4 nm $GaAs_{0.72}Sb_{0.28}$ hole wells embedded between two 4 nm $In_{0.28}Ga_{0.72}As$ electron wells, which are adjacent to GaAs barriers.
Measurements of a 975 μm long laser bar with the above specified active region at room temperature revealed a differential efficiency of 41%, a threshold current density of 1.0 kA/cm^2 and pump-limited maximum optical output powers of 0.68 W per facet [[4]]. Furthermore, the temperature-

dependent characterization of the device showed lasing from the fundamental type-II transition up to a temperature of 373.15 K.

3.2 Charge-transfer excitons in type-II structures

Excitons are electron-hole pairs which are bound via their mutual Coulomb attraction. In a type-II heterostructure[2] in principle two kinds of excitons are possible: the direct or regular exciton in structures where also a type-I band alignment between two semiconductor layers is present, and the charge-transfer exciton (CTX). In case of the CTX, the bound electron-hole pair is extended over different layers.
In modern type-II heterostructures, the charge transport through the internal interface is crucial for their performance. The CTX in combination with experimental techniques allows to characterize properties of the internal interface that are relevant for charge transport through it on a microscopic level.
Below, aspects of a detailed experimental and theoretical investigation of the formation and decay dynamics of CTX in a type-II heterostructure [[10]] will be discussed while more detailed information can be found in the publication itself.

For studying the formation and decay dynamics of the CTX, a type-II heterostructure where the charge transfer states can be directly excited has been designed in our group. Subsequently, the type-II structure was grown according to the requirements and the resulting structure was experimentally characterized. The findings were then confirmed by theoretical calculations. For this purpose, the measured and calculated absorption spectra were compared to each other for different theoretically realized layouts. This revealed a 7.7 nm wide Ga(AsSb) well with 3.3 % Sb and a 7.7 nm wide (InGa)As well with 5.8 % In. To match the lowest calculated and measured lowest two resonances of the optical absorption, the Ga(AsSb) bandgap was increased by 3.5 meV and the (InGa)As bandgap was decreased by 5 meV [[10]]. These minor adjustments lie well within the uncertainties of the experimentally derived bandgap bowing parameters of the compounds [[10, 29]]. Fig. 3.12 shows the confinement potential of this structure. Here, the green and blue backgrounds mark the Ga(AsSb)-layer and the (InGa)As-layer, respectively, while the white areas belong to the GaAs barriers and the 1 nm GaAs-interlayer between the wells.
To allow for comparison of results, a type-I reference structure was grown using the same layout but without a Ga(AsSb) well.
Both samples were optically characterized by absorption measurements.

[2] Generally, *type-II* refers to a heterostructure where the electron and hole ground states are situated in different layers. These layers are not necessarily adjacent to each other.

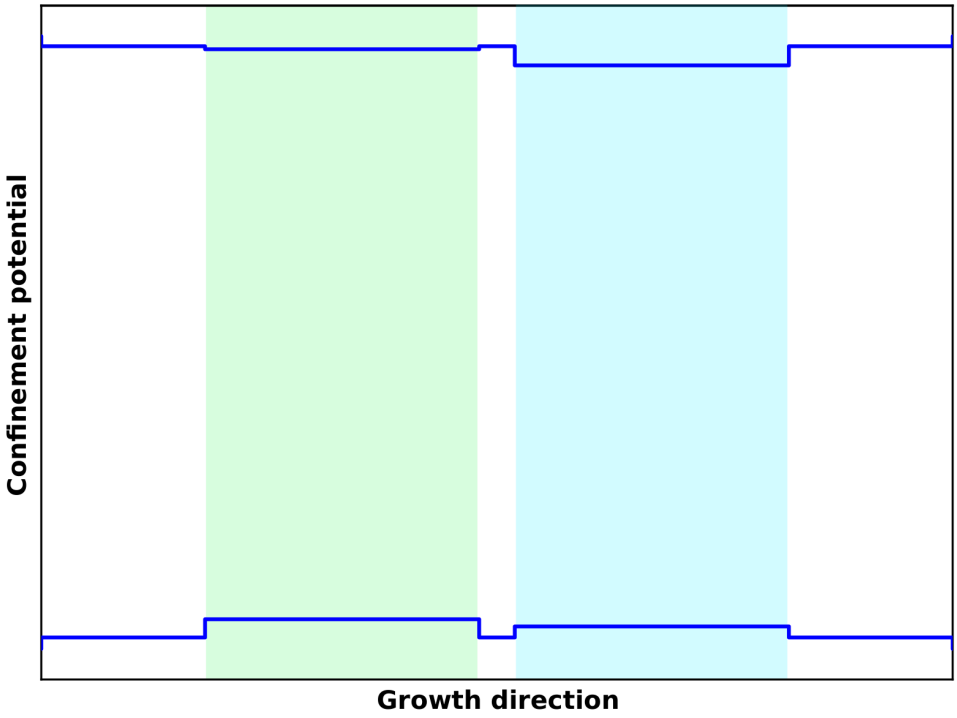

Figure 3.12: Layout of the confinement potential of the type-II Ga(AsSb)/GaAs/(InGa)As heterostructure from [[10]]. The green and blue backgrounds distinguish the 7.7 nm wide $GaAs_{0.967}Sb_{0.033}$ well (green) and the 7.7 nm wide $In_{0.058}Ga_{0.942}As$ well (blue) from GaAs.

THz-spectroscopy was used to confirm the excitonic resonances in the absorption spectra and to study the incoherent exciton dynamics. The coherent exciton dynamics were studied by four-wave mixing (FWM) measurements. All measurements were performed at 10 K.
To corroborate experimental findings and to gain further insights, the optical and THz absorbances were modeled and compared to the experimental results [[10]]. The required confinement wavefunctions, band edge energies, dipole matrix elements, confinement levels and the bandstructure were calculated with the theory presented in Section 2.2.1. The effective masses were obtained from fitting the bandstructure from the **k**·**p**-calculations.
Fig. 3.13 shows the experimental and theoretical optical absorption spectra. The experimental absorption spectrum clearly shows resonances at 1.451 eV and 1.464 eV, which are in accordance with the theoretical absorption spec-

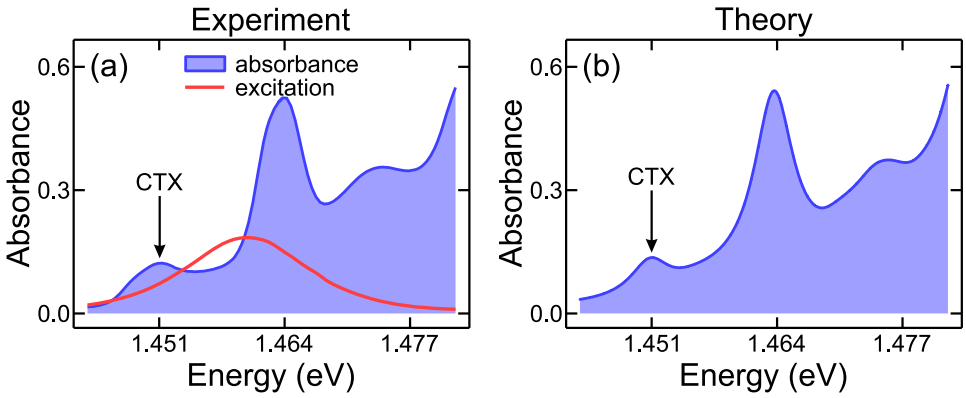

Figure 3.13: Experimental (a) and theoretical (b) optical absorption (solid blue lines) and absorbance spectra (blue area) of the Ga(AsSb)/GaAs/(InGa)As type-II heterostructure. The pump pulse is given by the red curve in (a). The arrows indicates the CTX resonance. The pictures have been taken from [[10]].

trum. These resonances are assigned to the CTX and the regular (InGa)As exciton, respectively. The energetically broad pump pulse (red curve in (a)) allows for a simultaneous excitation of direct (InGa)As and charge transfer polarizations.

The presence of the CTX and the (InGa)As exciton in the respective structures was confirmed for both kinds of excitons by THz measurements.

Fig. 3.14 shows the (a) measured and (b) computed THz absorbance for incoherent exciton populations as a function of the delay time Δt_{THz} between the optical pump pulse and the THz probe pulse and the THz photon energy $\hbar\omega_{THz}$. For this measurement, the type-II sample was resonantly excited to its direct type-I exciton. Fig. 3.14 (c) shows the type-I and CTX exciton resonance energies normed to the respective maximum of the $1s-2p$ transition energy as a function of Δt_{THz}. Both kinds of excitonic resonances were measured at comparable sheet carrier densities. The inset in (c) shows the THz absorbance of the type-I sample after the non-resonant excitation. At short delay times, the THz absorbance spectra of (a) and (b) predominantly show a Drude-like character. For longer delay times, the $1s-2p$ CTX resonance builds up and shifts towards $\hbar\omega_{THz}$=3.2 meV (arrows in (a) and (b)). The relative CTX $1s-2p$ transition energies presented in Fig. 3.14 (c) were extracted from Fig. 3.14 (a)(blue spheres for measured energies) and Fig. 3.14 (b) (red dots for calculated energies) while the direct

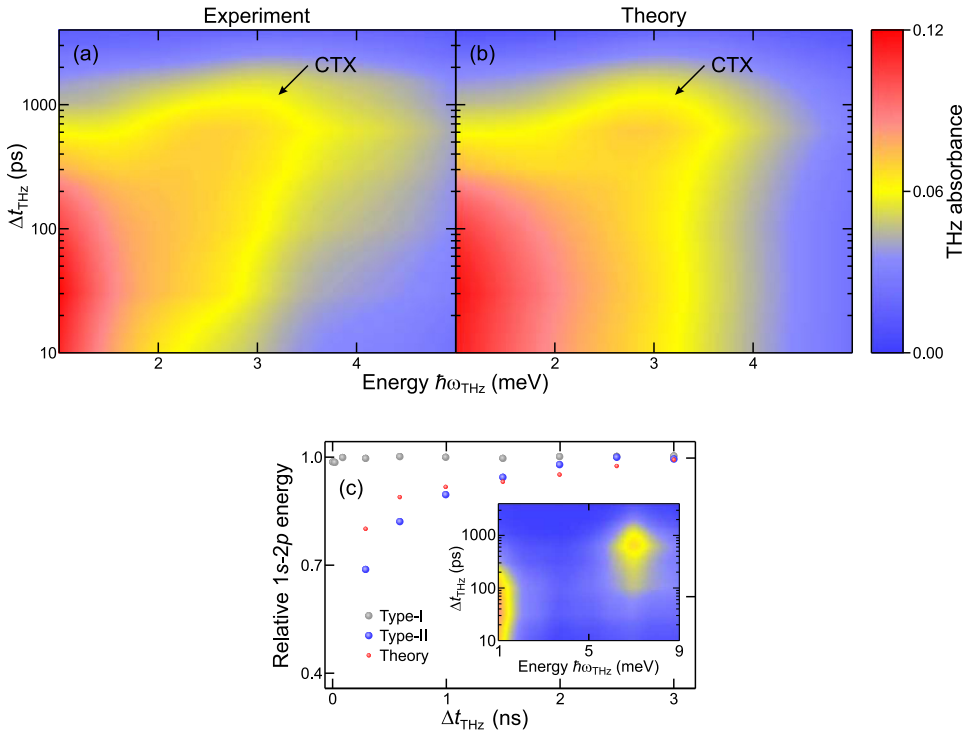

Figure 3.14: (a) Experimental and (b) theoretical THz absorbance of the type-II sample after resonant excitation to the direct exciton as a function of the delay time Δt_{THz} and the photon energy $\hbar\omega_{THz}$. (c) Shows the normed $1s-2p$ transition energies of the CTX in the type-II structure and the direct exciton in the type-I structure as a function of the delay time. Blue spheres refer to the measured CTX's transition energy while the red dots refer to the calculated transition energies of the CTX, both relative to 3.18 meV. Gray spheres refer to measured transition energies of the direct exciton relative to 6.97 meV. The inset shows the type-I structure's THz absorbance of the direct exciton after non-resonant excitation. The pictures have been taken from [[10]].

exciton's relative $1s-2p$ transition energies (gray spheres) were extracted from the measurements presented in the inset of (c). Since the phase-space filling factor increases with decreasing delay times, by plotting the relative CTX $1s-2p$ transition energies as a function of the delay time, the effect of phase-space filling on the resonance energies is illustrated. From the plot in

Fig. 3.14 (c) it can be deduced that the $1s-2p$ transition energy of the direct exciton is insensitive to carrier densities in the wells while this is not the case for the CTX. In case of the CTX, the small binding energy and large exciton Bohr radius enhance the non-bosonic characteristics of the CTX, which causes the CTX properties to be more sensitive to its fermionic substructure [[10]]. Because of this, the Coulomb attraction between electrons and holes is weakened by the repulsion between carriers of the same sign, which causes the CTX's $1s-2p$ transition energy to be smaller at shorter delay times.

In any case, neither the experimental nor the theoretical THz absorbances of the type-II structure show any distinguishable signatures of the direct exciton, even for short delay times. In accordance with this, FWM measurements of the coherent exciton dynamics revealed that the coherence of the direct exciton in the type-II heterostructure decays within the first 0.2 ps in cases where no or almost no CTX polarization is present [[10]]. Therefore, the absence of distinguishable direct exciton energies in the THz response is consistent with the fast decay of the direct exciton's coherences observed in FWM measurements only if the direct exciton polarization directly decays into a charge transfer electron-hole plasma and charge transfer exciton states.

In summary, the formation, decay, and coherence properties of the CTX have been studied experimentally and the results were theoretically analyzed using our predictive microscopic theory. The study demonstrates that valuable information on the microscopic charge transfer process can be gained by CTX spectroscopy.

Apart from the charge transport through internal interfaces, the magnitudes of the band offsets are crucial for the performance of quantum well heterostructures. The next chapter will deal with the investigation of band offsets between GaAs and Ga(AsSb) in quantum well heterostructures.

Chapter 4

Ga(AsSb)/GaAs band offsets

While the results presented in the previous chapter emphasize the benefits of using Ga(AsSb) and GaAs in light-emitting heterostructures, there is no clear consensus on the band alignment of these materials [[65–67]].
Below, two conceptually different approaches used for studying band offsets between GaAs and Ga(AsSb) in quantum well heterostructures will be presented. In Section 4.1 band offsets will be deduced from comparing experimental and theoretical results while in Section 4.2.1 and Section 4.2.2 *ab initio* calculations will be used to determine valence band offsets between GaAs and Ga(AsSb).

4.1 Experiment-theory comparison

Since time-resolved photoluminescence spectroscopy measurements of quantum well heterostructures with Ga(AsSb)-, GaAs- and (InGa)As-layers indicated a type-I band alignment between GaAs and Ga(AsSb) [[68]], the band alignment has been further investigated. For this purpose, the experimentally determined PL spectra of two structures that were used for the time-resolved measurements in [[68]] were compared to theoretically calculated ones [[11]].
Experimentally, 5.2 nm wide (InGa)As electron wells and 5 nm wide (GaAs)Sb hole wells were grown on GaAs substrates that were separated from each other by GaAs-interlayers with different widths for different structures. For each layout, the well-interlayer combination was grown five times in total while the repetitions were separated by a 50 nm layer of GaAs to avoid coupling between the confined charge carriers from different repetitions of the wells.

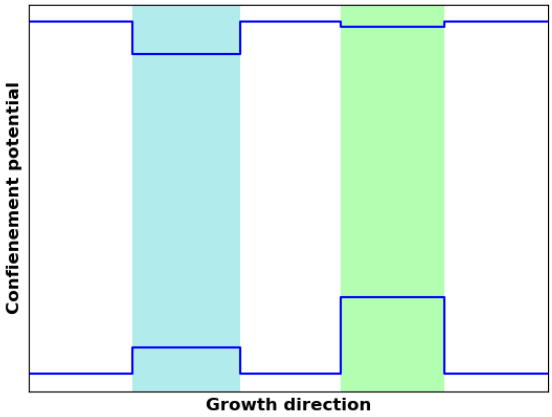

Figure 4.1: Illustration of the confinement potential of the interlayer-structures. The illustrated confinement potential belongs to structure $d_{4.8nm}$ at 100 K before including the attractive potential between spatially separated electrons and holes. The location of the Ga(AsSb) well is marked by the green background while the location of the (InGa)As well is marked by the blue background.

Out of the different structures that were characterized by measurements [[11, 68]], this study considers the structures with GaAs-interlayers of widths 3.5 nm (structure $d_{3.5nm}$) and 4.8 nm (structure $d_{4.8nm}$). For structure $d_{3.5nm}$, the measured concentrations in the (InGa)As and Ga(AsSb) well were 21.0±1.5% In and 23.8±1.5% Sb while for structure $d_{4.8nm}$ concentrations of 21.0±1.5% In and 23.3±1.5% Sb were measured.
The PL, confinement wavefunctions, dipole matrix elements and single-particle energies were calculated with the theory presented in Section 2.4.2 and Section 2.2.
Fig. 4.1 schematically shows the confinement potential of the structures on the example of structure $d_{4.8nm}$. To achieve good agreement between measured and calculated PL spectra, the experimentally determined concentrations were varied within the limits of the uncertainties. For structure $d_{3.5nm}$, this resulted in concentrations of 22.4% In and 23.6% Sb while for structure $d_{4.8nm}$, concentrations of 20.3% In and 23.7% Sb were used for the calculations.
To investigate the band alignment between GaAs and Ga(AsSb), a type-I

band alignment of these materials was assumed for the calculation of the PL spectra. Under this assumption, an investigation of the match between the experimental and calculated PL spectra was performed. While this was

$d_{4.8nm}$	**100 K**	**200 K**	**250 K**	**290 K**	$d_{3.5nm}$	**250 K**
Carrier temperature [K]	205	290	380	420	**Carrier temperature** [K]	265
$\mathbf{VBO_{GaAs/Ga(AsSb)}}$ [meV]	331	327	325	323	$\mathbf{VBO_{GaAs/Ga(AsSb)}}$ [meV]	324
$\mathbf{\Delta E_{HS}}$ [meV]	1014	984	967	952	$\mathbf{\Delta E_{HS}}$ [meV]	952

Table 4.1: Charge carrier temperatures (second line), GaAs/Ga(AsSb) VBO (third line) and effective bandgap (fourth line) of heterostructures $d_{4.8nm}$ and $d_{3.5nm}$ for the temperatures listed in the first line.

done for a temperature of 250 K in the case of structure $d_{3.5nm}$, for structure $d_{4.8nm}$ 100 K, 200 K and 290 K PL were used as well. To match the type-I and type-II transition energies, the band offsets were varied for each temperature. In doing so, the fraction of the bandgap difference between GaAs and Ga(AsSb) assigned to the conduction band offset (CBO) was kept constant. For both structures and all considered temperatures this resulted in a GaAs/Ga(AsSb) CBO with an absolute value of 19 meV (rounded). The experimental type-II transition energies were approached by shifting the (InGa)As conduction band edge relative to the Ga(AsSb) valence band edge. Table 4.1 contains the corresponding GaAs/Ga(AsSb) valence band offsets (VBOs) and the effective bandgaps of the heterostructures (ΔE_{HS}). ΔE_{HS} is the absolute value of the heterostructure's conduction band edge and valence band edge energy difference.

Figs. 4.2 and 4.3 show the theoretical and experimental PL of the structures. As can be seen in the two upper panels of Fig. 4.2, the theoretical and experimental transition energies are in agreement, but the theoretically calculated relative peak-heights from the type-II (lower energy peak) and Ga(AsSb) type-I (higher energy peak) transitions differ from the experimental ones. While minor deviations of the peak-positions most likely stem from slightly different concentrations in the samples, deviations of the relative peak-heights indicate that the charge carrier system is not yet in a complete quasi-equilibrium within the entire heterostructure [[11]]. To account for this state of a weak non-equilibrium, temperatures higher than the lattice temperatures have been assigned to the charge carrier distributions. Because of the weakness of the non-equilibrium state, Fermi-Dirac distributions still are a good approximation for the charge carrier distributions. In the case of structure $d_{4.8nm}$, a considerably higher effective carrier

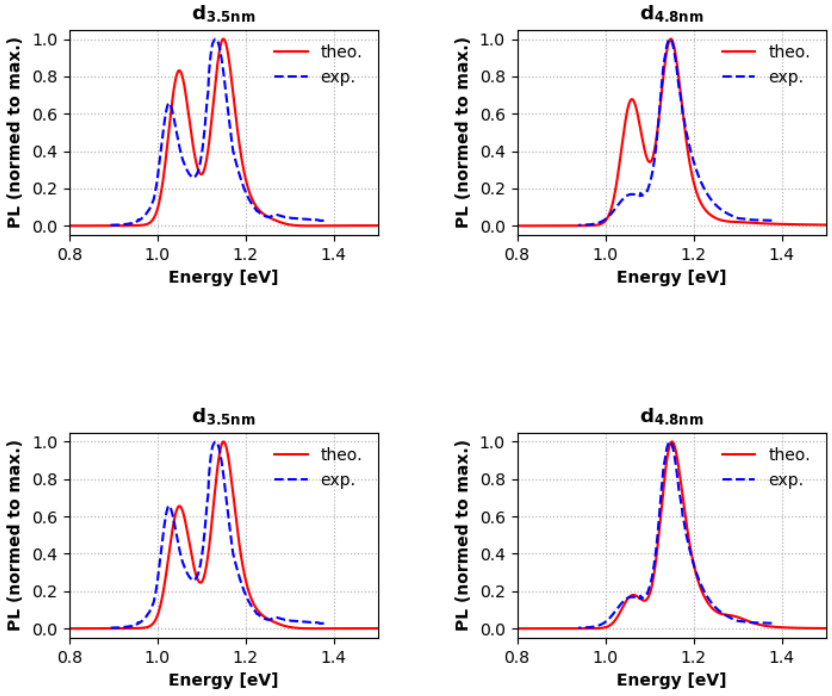

Figure 4.2: Theoretical (solid red lines) and experimental (dashed blue lines) PL of the structures $d_{3.5nm}$ and $d_{4.8nm}$ at a lattice temperature of 250 K. The upper parts show the PL of the structures for the same carrier and lattice temperatures. In the lower parts, the carrier temperatures exceed the lattice temperature. Here, for structure $d_{3.5nm}$, a carrier temperature of 265 K was used for the calculations while for structure $d_{4.8nm}$, the carrier temperature of 380 K was used. These figures wer plotted with data from [[11]].

temperature of 380 K at a lattice temperature of 250 K was necessary to match the relative peak-heights. In contrast to this, for structure $d_{3.5nm}$ a mere effective carrier temperature of 265 K at a lattice temperature of 250 K was necessary. This difference most likely originates from less efficient tunneling processes in structure $d_{4.8nm}$, since the wells of this structure

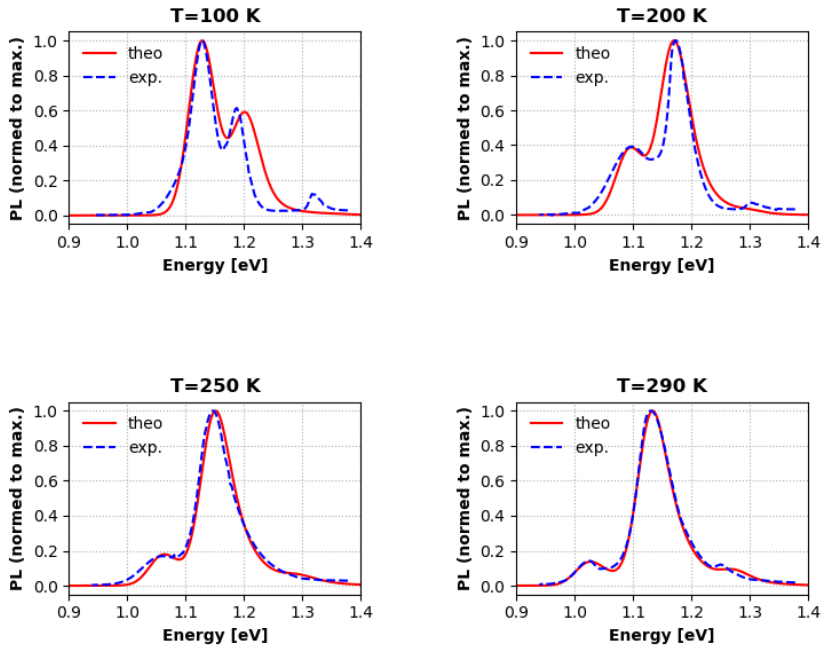

Figure 4.3: Theoretical (solid red lines) and experimental (dashed blue lines) PL of structure $d_{4.8nm}$ for lattice temperatures mentioned in the respective title and elevated charge carrier temperatures. The corresponding charge carrier temperatures can be seen in Table 4.1. These figures were plotted with data from [[11]].

are further apart. In the experiment, the charge carriers were excited non-resonantly into states which belong to GaAs. Subsequently, they relax into the (InGa)As and Ga(AsSb) quantum wells and tunnel into the respective lowest states through the GaAs-interlayer between the wells. In the case of the thicker GaAs-interlayer, the tunneling probability through the interlayer is notably lowered because of the exponential decay of the carrier wavefunctions within the interlayer. Hence, in structure $d_{4.8nm}$, it is less likely for not completely relaxed electrons and holes to tunnel into the respective lowest states in the (InGa)As and Ga(AsSb) wells than it is for electrons and

holes in structure $d_{3.5nm}$. As a result, the charge carriers in structure $d_{4.8nm}$ are at higher energies on average. Thus, they are effectively hotter during emission processes than charge carriers in structure $d_{3.5nm}$.
However, when comparing the calculated and measured spectra at different temperatures of structure $d_{4.8nm}$ in Fig. 4.3, it becomes apparent that at lattice temperatures of 100 K and 200 K, the (InGa)As type-I transition appears in the measured PL (high energy peak of the dashed blue lines) but not in the calculated one. This stems from the fact that the theoretical PL is based on non-dynamical calculations and it is assumed that all tunneling transitions took place already. Hence, in the calculations there are not enough charge carriers available in the (InGa)As well such that this transition does not appear in the theoretical PL. Moreover, a shoulder appears in the theoretical PL at a lattice temperature of 290 K which stems from the type-I (InGa)As transition. In the case of the experimental PL at 290 K, this transition cannot be clearly distinguished from the background noise [[11]].

While the presented study shows that a type-I band alignment between GaAs and Ga(AsSb) is realistic, this study is restricted to the investigated heterostructures used for the measurements.
In the following sections, the study of GaAs/Ga(AsSb) band offsets will be continued. In contrast to the study presented above which relies on experiment-theory comparisons, *ab initio* (or *first principles*) methods will be used. By this, an extended concentration range can be accessed and the resulting VBOs can be used to deduce band alignments that are not restricted to certain heterostructures.

4.2 *Ab initio* calculation of valence band offsets

The attempt of calculating band offsets from *first principles* has a long history and different approaches have been made.
For example, C. G. Van de Walle and J. Neugebauer used the energetic location of hydrogen levels within semiconductor compounds to obtain unstrained (natural) band offsets [[69]]. This resulted in band offset values with error bars of ±200 meV [[69]].
If the bandgaps of the studied materials are known, it suffices to calculate their VBO to deduce their band alignment since these two quantities implicitly determine their CBO. J. M. Bass *et al.* [[70]] used the localized density of states to determine VBOs. While this allows to obtain the VBO from a single DFT calculation, it has the disadvantage of introducing additional adjustable parameters.
The state of the art in *ab initio* calculations of VBOs is to combine bulk-like properties and information about the interface. The core-to-valence band maximum method represents such an approach and was introduced by Wei and Zunger [[71]] for the calculation of natural VBOs with DFT. Since modeling strained quantum well heterostructures requires strained VBOs, Wei and Zunger's method has been modified for this case [[12]]. This so-called *modified core-to-valence band maximum* approach yields VBOs that can be readily applied to model pseudomorphically grown heterostructures.
In Section 4.2.1, the modified core-to-valence band maximum approach will be introduced for the example of the GaAs/Ga(AsSb) interface and results for this interface will be presented.
While using this approach for the calculation of the GaAs/Ga(AsSb) VBOs, two problems emerged for certain Sb concentrations. These are diverging results for different Ga(AsSb)-layer lengths and vanishing Ga(AsSb) KS-bandgaps. In general, the problem of vanishing KS-bandgaps has been addressed with different approaches, e. g. with hybrid-functionals [[38]], the quasi-particle approach within GW [[72]] or the DFT-1/2 method [[5, 6]]. While the former two approaches are accompanied by a considerably higher numerical effort than GGA-DFT, DFT-1/2 calculations have the advantage of having the numerical complexity of the used LDA- or GGA-functional. Therefore, DFT-1/2 is a suitable choice for interface calculations in cases where other approaches are numerically prohibitive. A short introduction to DFT-1/2, which is often called the method of half-occupations, was given in Section 2.3.4. Since the self-energy correction of DFT-1/2 is vanishing for Bloch-waves, the localized states of the topmost valence band are usually corrected. This enables the use of DFT-1/2 within the modified core-to-

valence band maximum approach. In Section 4.2.2, this combination has been used to calculate the presented GaAs/Ga(AsSb) VBOs.

4.2.1 Modified core-to-valence band maximum approach

In the framework of the modified core-to-valence band maximum approach [[12]] the VBO between two materials is essentially calculated using valence band maxima (VBM) which are obtained from calculations with strained bulk cells.
The approach allows for the calculations of VBOs in heterostructures that are pseudomorphically grown on a substrate. In all studies presented in this thesis, GaAs was used as a substrate. In the calculations, the pseudomorphic growth of the materials has been taken into account by fixing the lattice constants in the plane perpendicular to growth direction (in-plane direction) to that of the substrate. These in-plane directional lattice constants have been assigned to the x- and y-directions.
However, the VBM from bulk DFT calculations are accompanied by an unknown energy offset which needs to be corrected before determining the VBO. This stems from an misalignment of the energy scales of the separate bulk calculations and stems from the fact that the average electrostatic potential in an infinite solid is an ill-defined quantity [[73]]. Because of this, a common reference energy is needed to align the energy scales from the bulk calculations.
In this way, the choice of the reference energy influences the accuracy of the results. A highly suited choice is the $1s$ electron level, because it is strongly localized and thereby only influenced by the local chemical surrounding. Hence, this energy level is used as the needed reference. For the purpose of aligning the energy scales from the DFT calculations with bulk cells, the $1s$ electron levels are calculated for each bulk cell and additionally for an interface cell, which is constructed using the bulk cells.

Overall, for the calculation of GaAs/Ga(AsSb) VBOs within the modified core-to-valence band maximum approach, the following steps were necessary for bulk and interface DFT calculations:

(i) The GaAs and Ga(AsSb) bulk cells were constructed and, in order to model growth on a GaAs substrate, the lattice constants of Ga(AsSb) were fixed to the previously obtained GaAs lattice constant in in-plane direction.

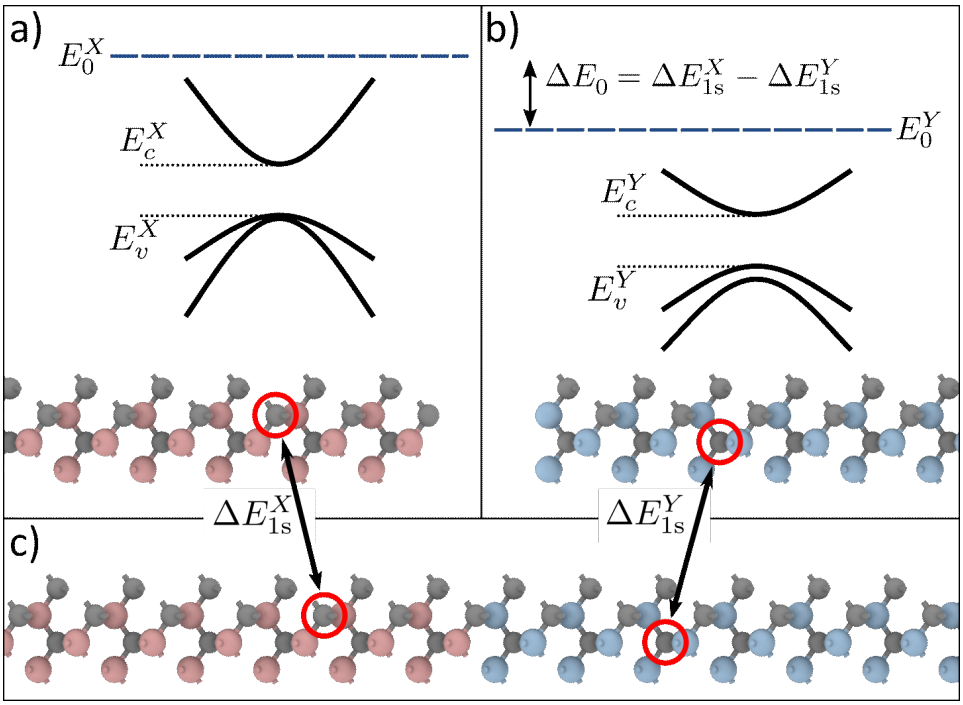

Figure 4.4: Illustration of the alignment of energy scales from two separate DFT calculations for the bulk materials X and Y. In the middles of part a) and b), schematic bandstructures of the bulk materials X and Y are shown. E_v^X and E_v^Y label the VBM of the materials while E_c^X and E_c^Y label their conduction band minima. Part c) shows an interface cell which was constructed by stacking the bulk cells onto each other. E_0^X and E_0^Y (dashed blue lines in a) and b)) are the reference energy levels that are used to align the energy scales. For this purpose we chose the $1s$ electron level. The calculation of their energy difference ΔE_{1s}^X and ΔE_{1s}^Y in bulk and interface cells with this level yields the offset of the calculations as $\Delta E_0 = \Delta E_{1s}^X - \Delta E_{1s}^Y$. This picture has been taken from [[12]] (modified version).

(ii) The bulk cells were relaxed to allow for changes in cell shapes and atomic positions. Specifically, solely the lattice constants in growth direction (z-direction) were allowed to change.

(iii) Electronic structure calculations of the relaxed bulk cells were carried out to obtain the GaAs and Ga(AsSb) VBM ($E_v^{\mathrm{Ga(AsSb)}}$ and E_v^{GaAs})

and all Ga $1s$ electron levels for each cell.

(iv) The interface cell was constructed by stacking the relaxed bulk cells onto each other in z-direction.

(v) The relaxation from (ii) was repeated for the interface cell to take corrections of the atomic structure at the interface into account.

(vi) Electronic structure calculations of the relaxed interface cell were carried out to obtain all Ga $1s$ electron levels of the interface cell.

After the DFT calculations, the energy scales of the two bulk calculations were aligned using the energy difference of the Ga $1s$ levels from the exact image atoms in bulk and interface cells. This is illustrated in Fig. 4.4, where ΔE_0 denotes the offset of the energy scales from the bulk calculations for materials X and Y. In doing so, the vicinity of the interface was excluded. Altogether, the VBO E_{VBO} was calculated as [[12]]

$$E_{\mathrm{VBO}} = \left(E_v^{\mathrm{Ga(AsSb)}} - \Delta E_{1s}^{\mathrm{Ga(AsSb)}}\right) - \left(E_v^{\mathrm{GaAs}} - \Delta E_{1s}^{\mathrm{GaAs}}\right) , \qquad (4.1)$$

were $\Delta E_{1s}^{\mathrm{GaAs}}$ and $\Delta E_{1s}^{\mathrm{Ga(AsSb)}}$ are the energy offsets of the bulk- and interface-$1s$ levels. By aligning the VBM which are obtained from bulk calculations, the modified core-to-valence band maximum method yields true bulk-like VBOs.

As mentioned in Section 2.3, for all presented VBO calculations the functional PBEsol [[44]] was used. Whereas for GaAs the cell size of $(2\times2\times2)$ unit cells was used, different cell sizes of $(2\times2\times2)$, $(2\times2\times3)$ or $(2\times2\times4)$ unit cells were used for the Ga(AsSb) cells, belonging to Ga(AsSb)-layers containing 64, 96 or 128 atoms, respectively. The Ga(AsSb)-layers were constructed using special quasi-random structures (for more details see [[74, 75]]). For cell-sizes of $(2\times2\times2)$, $(2\times2\times3)$ or $(2\times2\times4)$ unit cells, Γ-centered Monkhorst-Pack k-point grids [[76]] of $(5\times5\times5)$ in the first case and $(5\times5\times3)$ in the latter two cases were used. For the GaAs/Ga(AsSb) interface calculations, $(5\times5\times3)$ k-point grids were used in case of $(2\times2\times2)$ unit cells for Ga(AsSb) and $(5\times5\times2)$ k-point grids otherwise. For the electronic structure calculations, spin-orbit coupling was taken into account. All calculations were carried out with a kinetic energy cut-off of 368 eV[1]. These numerical settings were used for all VBO calculations with DFT that are presented in this thesis.

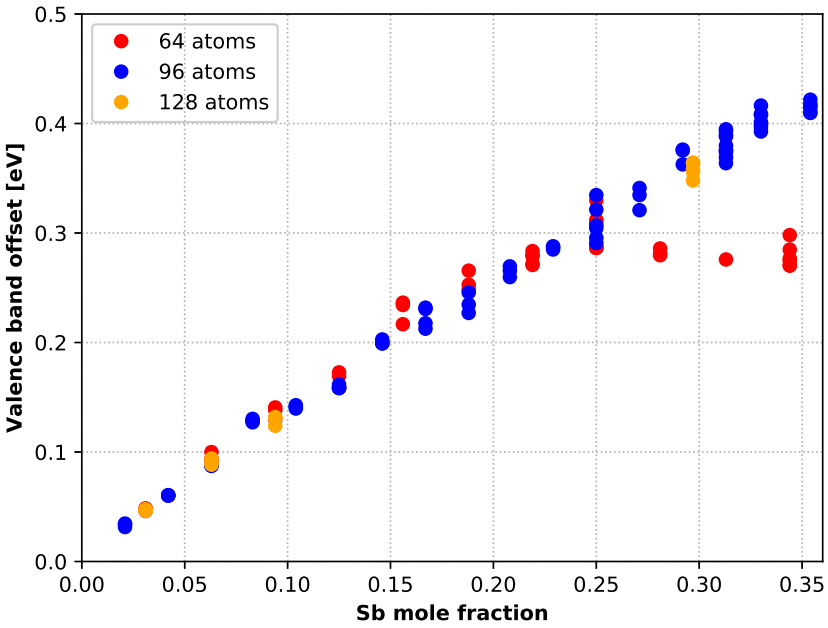

Figure 4.5: VBOs between GaAs and Ga(AsSb) dependent on the Sb mole fraction calculated within the modified core-to-valence band maximum approach. The color of the data points refers to different numbers of atoms in the Ga(AsSb)-layer, which is given in the legend. For Sb concentrations above 25% the results diverge.

Fig. 4.5 presents the GaAs/Ga(AsSb) VBO as a function of the Sb mole fraction up to a mole fraction of 0.354 Sb in Ga(AsSb). Here, the red, blue and orange dots belong to calculations with 64, 96 and 128 atoms in the Ga(AsSb)-layer, belonging to the $(2 \times 2 \times 2)$, $(2 \times 2 \times 3)$ or $(2 \times 2 \times 4)$ cells, respectively. [2] Except for the single configuration belonging to the red dot at 31.3% Sb, for all calculations at minimum three different configurations of the Ga(AsSb)-layer have been used. In case of the blue dots, additional

[1] This is the rounded value from 367.4983 eV which is the maximum value of all ENMAX-values that can be found in the used POTCAR-files multiplied by 1.3.

[2] This leads to Ga(AsSb) cell lengths in growth direction of 11.4 Å to 11.9 Å (3.1% until 34.4% Sb) for $(2 \times 2 \times 2)$ cells, 17.0 Å to 17.9 Å (2.1% until 35.4% Sb) for $(2 \times 2 \times 3)$ cells, and 22.8 Å to 23.7 Å (3.1% until 29.7% Sb) for $(2 \times 2 \times 4)$ cells.

configurations for the Ga(AsSb)-layer were added at concentrations where a considerable spread of the VBO-values was observed.
As can be seen in Fig. 4.5, up to Sb concentrations of 25%, all results agree and basically depend linearly on the Sb concentration. In contrast to this, above 25% Sb the results split into two different curves depending on the Ga(AsSb)-layer lengths. Furthermore, for Ga(AsSb) concentrations $\gtrsim$23% Sb the KS-bandgaps are smaller than 0.1 eV in many cases [[13]]. In such cases, the modified core-to-valence band maximum approach does not yield reliable results.
In order to solve this, the modified core-to-valence band maximum approach has been extended by the inclusion of DFT-1/2. More specifically, this was done in order to clearly observe a bandgap at elevated Sb concentrations and to be able to unambiguously align the VBM of GaAs and Ga(AsSb) at these concentrations. This will be discussed in the following section.

4.2.2 Half-occupation technique within the modified core-to-valence band maximum approach

In order to use the half-occupation technique within the modified core-to-valence band maximum approach, for the electronic structure calculations the pseudopotentials of the states that form the topmost valence band have been corrected with the corresponding self-energy potential V_S (compare to Section 2.3.4).
As discussed in Section 2.3.4, for the application of the half-occupation technique to solids, each self-energy potential needs to be suitably truncated before introducing it into the pseudopotential of the solid. For this purpose, the cut-off functions from Eq. (2.36) and Eq. (2.37) have been introduced where the optimized cut-off radii are obtained from bandgap maximization. Since in the present case GaAs/Ga(AsSb) interfaces are the subjects of study, both the bandgaps of GaAs and GaSb were maximized. At first it was verified that these maximizations do not lead to considerably different radii sets for Ga, for cases where Eq. (2.37) was applied. Second, the effect on the VBO results of either using Eq. (2.37) or Eq. (2.36) when trimming the self-energy potentials was tested.
Hence, for the use of Eq. (2.37) at first the cut-off radii belonging to the anions were determined from bandgap maximization of GaAs and GaSb which resulted in radii sets of 1.440 a_{Bohr} and 3.184 a_{Bohr} for As and 1.755 a_{Bohr} and 3.494 a_{Bohr} for Sb with $a_{\mathrm{Bohr}} = 0.529177 \cdot 10^{-8}$cm. Subsequently, the anion's trimmed self-energy potentials were included into the pseudopotential of the respective solid and V_S was calculated for Ga in each case.

The self-energy potential of Ga was then trimmed with various inner and outer radii combinations, the trimmed potentials were included into the GaAs and GaSb pseudopotentials, and the bandgaps were calculated for both solids. Here, the bandgap maximization of GaAs lead to the Ga-radii set of 2.15 a_{Bohr} and 3.9 a_{Bohr}, while the bandgap maximization of GaSb lead to the Ga-radii set of 2.189 a_{Bohr} and 3.933 a_{Bohr}. The difference of the cut-off radii is 0.036 a_{Bohr} for the inner radii and 0.033 a_{Bohr} for the outer radii and lies within the scope of the numerical accuracy. Hence, it should be interchangeable which of the two Ga-radii sets is used for the truncation of its self-energy potential in VBO calculations.
This was tested for the GaAs/Ga(AsSb) interface at Sb concentrations of 34.4% and 35.4%. Here, for each Sb concentration two configurations of the Ga(AsSb)-layer were used[3]. For identical GaAs/Ga(AsSb) interfaces, minor deviations were observed for the VBO results from calculations with the two different Ga-radii sets. In order to evaluate the effect on the VBO calculations, the standard deviation of the VBO results from using the two different radii sets was calculated for each interface configuration where the two sets were applied. This yielded a maximum standard deviation of 0.66 meV. Since this value is negligible in the framework of the presented VBO calculations, the interchangeability of the radii sets during the VBO calculations with Eq. (2.37) has been demonstrated. For subsequent calculations with Eq. (2.37), the radii combination of 2.15 a_{Bohr} and 3.9 a_{Bohr} for trimming of the Ga self-energy potential was used.
Furthermore, the impact of using either function Eq. (2.36) or Eq. (2.37) for trimming the self-energy potentials was tested at 34.4% and 35.4% Sb. For this purpose, the same four interfaces as mentioned above were used. In case of using Eq. (2.36), the self-energy correction was only applied to the anions as suggested in [[5]]. The used cut-off radii for the spherical trimming were 3.353 a_{Bohr} for As and 3.687 a_{Bohr} for Sb. For interfaces with identical atomic arrangements and for calculations either with Eq. (2.36) or Eq. (2.37), the VBO deviations were in the order of meV. Here, a maximum standard deviation of 2.39 meV was observed for identical interfaces.
The spread caused by different atomic arrangements in the Ga(AsSb)-layer when the same cut-off functions and radii combinations were used resulted in a minimum and a maximum standard deviation of 4.46 meV and 22.15 meV

[3]Included was an odd-configuration at 34.4% Sb, which showed an agglomeration of Sb atoms at the interface. Such a configuration where nearly all atoms can be found in adjacent layers was only observed in this case. Thus, this configuration was excluded from calculations that aim to produce realistic VBO results with and without DFT-1/2, because of being considered as being unlikely to be found in grown heterostructures.

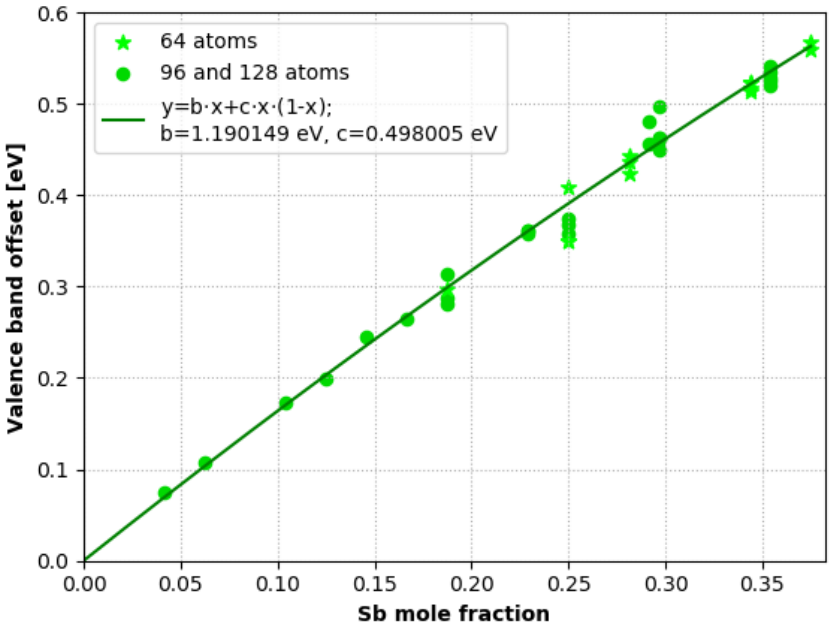

Figure 4.6: VBOs between GaAs and Ga(AsSb)as a function of the Sb mole fraction calculated with the modified core-to-valence band maximum approach combined with the half-occupation technique (green dots and stars). The stars mark short Ga(AsSb)-layer comprising 64 atoms. The data point spread for some concentrations stems from different atomic configurations in the Ga(AsSb)-layer. An analytical fit of the configurationally averaged VBO is given by the solid line. This picture has been taken from [[13]] (modified version).

at the same Sb concentration. Since this is considerably larger than the standard deviations from the above comparisons, it can be concluded that the spread of the VBO at the same Sb concentrations basically stems from different configurations in the Ga(AsSb)-layer.

However, for both GaAs and GaSb, electronegativity differences suggest a strong covalent character of the bonds, which has been confirmed by studies [[6, 77, 78]]. Thus, in case of the GaAs/Ga(AsSb) interface the bonding

electrons are considered to be shared by the bonding partners. Because of this, the spherical-shell trimming from Eq. (2.37) was used and the self-energy correction was applied to the anions and the cation. In doing so, 1/4-charges were stripped from each bonding partner to avoid a double counting of the correction when the self-energy potentials are incorporated into the pseudopotential-file of the respective solid.
For the calculations of the VBOs, already existing configurations from interface calculations for Fig. 4.5 were used. Since these calculations are computationally demanding, some configurations were omitted. This was done especially for concentrations well below 23% Sb where a much lower spread of the VBO results in comparison to higher Sb concentrations was observed. The results are presented in Fig. 4.6. Here it becomes apparent that contrary to the results from Fig. 4.5 the results from Fig. 4.6 are independent of the Ga(AsSb)-layer length and show no splitting into two branches. Therefore, the use of the half-occupation technique ensures a finite bandgap[4] in all present calculations and successfully removes the divergence of the VBO results.
As can be seen in Fig. 4.6, the spread of the VBO results strongly varies for different Sb concentrations. Here, the maximum standard-deviation from the mean value is 20 meV at 25% Sb. For the applications in material design studies, an analytical fit of the configurationally averaged VBO is provided [[13]]:

$$y = 1.190149\,\mathrm{eV} \cdot x + 0.498005\,\mathrm{eV} \cdot x \cdot (1 - x) \; . \tag{4.2}$$

Here, y is the VBO in eV and x the Sb mole fraction. In Fig. 4.6, the fit is plotted as the solid green line. While the underlying data points are fitted well by Eq. (4.2), it is considered to be strictly valid only within the concentration range which is shown in Fig. 4.6.
Altogether, the results from Fig. 4.6 agree well with the corresponding results from C. M. Jones and E. Kioupakis (compare for example to the solid lines of the lower part of the Fig. 2 in [[7]]).
Whereas the results of Jones and Kioupakis are obtained from **k**·**p**-calculations for a model-solid theory and therefore depend on prior experimental input, this is not the case for the approach used here. For 35% Sb, the authors [[7]] explicitly provide the VBO of 540 meV for the pseudomorphically strained GaAs/Ga(AsSb) interface. This value is in good agreement with the here calculated VBOs (compare to the data points in Fig. 4.6) and with

[4] Fig. 3 in the supplementary material from [[13]] shows a plot of the Ga(AsSb) bandgaps belonging to the calculations from Fig. 4.6.

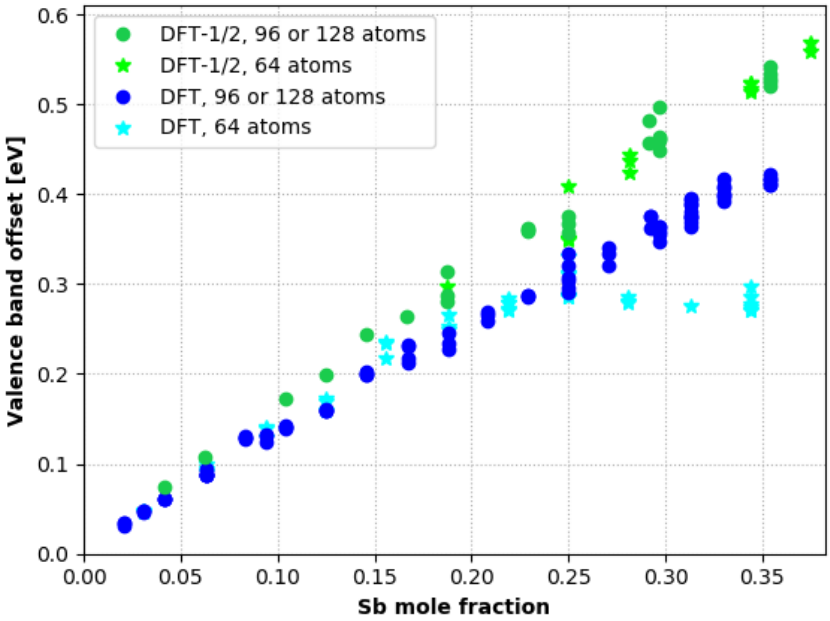

Figure 4.7: VBOs between GaAs and Ga(AsSb) calculated with the modified core-to-valence band maximum approach in combination with the half-occupation technique and (labeled as DFT-1/2 in the legend) and without this technique (labeled as DFT in the legend) as a function of the Sb mole fraction. The number of atoms in the Ga(AsSb)-layer is given in the legend.

the VBO of 529.9 meV obtained from Eq. (4.2). Moreover, S.-W. Ryu and P. D. Dapkus [[79]] obtained a VBO of 406 meV for a GaAs/Ga(AsSb) interface with 27% Sb by fitting experimental data from an (InGa)As/Ga(AsSb) "W"-structure grown on a GaAs substrate and applying the transitivity rule. Again, this value agrees well with the VBO of 419.5 meV from Eq. (4.2).

In conclusion, Fig. 4.7 shows the VBO results from the modified core-to-valence band maximum method with and without the application of the half-occupation technique. Here, the green data points refer to the results obtained with the half-occupation technique. As can be seen in Fig. 4.7, for very low Sb concentrations, the green and blue results are in agreement

with each other. Nevertheless, as the Sb content increases, the green and blue data points increasingly diverge. This is most pronounced above 25% Sb where it is not possible to clearly assign VBOs in case of the blue data points, since they split into different curves depending on the number of atoms in the Ga(AsSb)-layer. The divergence of the blue data points can be removed by inclusion of the half-occupation technique into the modified core-to-valence band maximum approach. Together with the comparison to published results from [[7, 79]] it is concluded, that combining the modified core-to-valence band maximum method with the half-occupation technique has proven to be suitable for the calculation of pseudomorphically strained GaAs/Ga(AsSb) VBOs. Furthermore, this approach has the potential to be applicable to similar semiconductor systems as well.

To compare the calculated VBO results to the results from Section 4.1, the GaAs/Ga(AsSb) VBOs at Sb contents of 23.7% Sb and 23.6% were calculated with Eq. (4.2). These are the Sb concentrations from structures $d_{4.8nm}$ and $d_{3.5nm}$. Here, the calculated VBO values exceed the ones obtained from fitting experimental data, as well as the GaAs-Ga(AsSb) bandgap differences in structures $d_{4.8nm}$ and $d_{3.5nm}$ at all temperatures. Thus, in contrast to the results obtained from fitting experimental data, a type-II band alignment follows for these structures using the modified core-to-valence band maximum approach combined with the half-occupation technique.

From $\mathbf{k}\cdot\mathbf{p}$ based calculations, C. M. Jones and E. Kioupakis [[7]] conclude that the band alignment of GaAs and Ga(AsSb) in quantum well heterostructures mainly depends on strain. While the authors observed a type-II band alignment for pseudomorphically strained layers, the band alignment changes from that to type-I at certain percentages of strain relaxation in dependence on the well width and the Sb mole fraction.

Further studies could help to clarify the discrepancy between the measured lifetimes of the PL assigned to the lowest type-I transition of the $GaAs_{0.763}Sb_{0.237}$-well from Section 4.1 and the type-II band alignment between GaAs and $GaAs_{0.763}Sb_{0.237}$, which results from the DFT calculations from Section 4.2.2.

A starting point could for example be provided by calculations analogous to the ones from Section 4.2.2, with in-plane lattice constants of the Ga(AsSb) cells that have been gradually changed from the substrates lattice constant towards the Ga(AsSb) lattice constant.

Chapter 5

Conclusion

This thesis summarizes results from the theoretical investigation of the optical and electronic properties of pseudomorphically grown quantum well heterostructures. The optical properties were calculated using the reliable microscopic many-body approaches of the semiconductor Bloch and semiconductor luminescence equations in combination with $\mathbf{k}\cdot\mathbf{p}$-calculations. Furthermore, the band alignment between GaAs and Ga(AsSb) in such heterostructures was studied using DFT.

In Chapter 3, results were presented from calculations that aim to optimize the optical properties of "W"-structures with (InGa)As and Ga(AsSb) wells pseudomorphically grown on GaAs. At first, suitable designs for emission wavelengths around 1200 nm and an experimentally realized laser structure [[9]] were presented. A strong agreement was seen between the experimentally measured and theoretically predicted spectra.

Subsequently, the effect on the optical properties caused by modifying the charge carrier confinement by using different barrier layers was theoretically investigated.

The gained findings were then used to carefully study optimized designs for "W"-structures with an emission wavelength close to 1300 nm. Furthermore, in order to favor the emission from the fundamental transition at elevated carrier densities, the variation of the energy-distance between the first and second electron confinement level with varying layer lengths was studied. Altogether, this resulted in different ways to optimize the optical properties of "W"-structures. Here, the strongest effect on the emission strength resulted from using thinner wells, which is also experimentally feasible. The presented studies and further calculations contributed to the experimental realization of an electrical injection laser with an emission wavelength close

to 1300 nm [[4]].
The last part of Chapter 3 presented aspects from the first-ever[1] combined experimental and theoretical investigation of the optical and THz properties of charge-transfer excitons [[10]]. For this study, a structure in which the (InGa)As electron well was separated by a GaAs layer from the Ga(AsSb) hole well was used. The results [[10]] are highly relevant for the non-destructive characterization and optimization of electronic transport and charge transfer processes across internal interfaces in the future.
Finally, Chapter 4 focused on the determination of band offsets between Ga(AsSb) and GaAs in strained heterostructures, which determine the material's band alignment in strained heterostructures. The first part of this chapter presented experiment-theory comparisons from which the band alignment and the band offsets between GaAs and Ga(AsSb) were deduced [[11]]. The structures used for this study comprised of an (InGa)As electron well and a Ga(AsSb) hole well that were pseudomorphically grown on GaAs and spatially separated by a GaAs-interlayer. Measurements indicated a type-I band alignment between GaAs and Ga(AsSb) and theoretical calculations showed that this is possible. The following parts of this chapter introduce approaches to calculate VBOs between pseudomorphically strained layers with DFT [[12, 13]]. For Ga(AsSb), standard DFT calculations with PBEsol resulted in vanishing Kohn Sham-bandgaps and diverging VBO results. This was corrected by introducing the half-occupation technique to the VBO calculations [[13]]. The resulting VBOs are in good agreement with calculated values (obtained from $\mathbf{k}\cdot\mathbf{p}$-calculations for a model-solid theory) and experimental results [[7, 79]]. However, for the respective antimony concentrations, the type-II band alignment between strained GaAs and Ga(AsSb) resulting from the latter DFT VBO calculations differs from the type-I band alignment deduced from fitting experimental data. Here, further studies could contribute to clarification.
In conclusion, well established microscopic many-body theories have proven their merit for predicting and characterizing optical properties of (InGa)As and Ga(AsSb) based quantum well heterostructures pseudomorphically grown on GaAs. The use of DFT in combination with the half-occupation technique enabled the determination of VBO between GaAs and Ga(AsSb) for Sb concentrations ranging between 0 and 35.4%.
Regarding optical communication, an extension of the emission wavelengths of type-II lasers is desirable. However, for the presented (InGa)As and Ga(AsSb) based "W"-structures, the emission wavelength range is limited

[1] This information refers to the time at which manuscript was written.

by the possibility to grow high quality layers at elevated Sb or In contents. Therefore, the extension of the emission wavelength of type-II "W"-structures towards wavelengths around 1500 nm could be realized by using materials that contain N or Bi in form of dilute-nitrides or dilute-bismides (see [[80]] for example). These materials could be either based on GaAs or as well on (InGa)As or Ga(AsSb), where N or Bi replaces a small fraction of As or respectively Sb (see [[81]] for example).
Returning to the VBO calculations, the discrepancy between the band alignment results from theory-experiment comparisons and the alignment using the VBO from *ab initio* calculations could be further investigated by considering the effect of strain relaxation during VBO calculations, as suggested in Section 4.2.2.

Appendix A

Numerical calculations

A.1 Symmetric heterostructures

For calculations of the properties of the symmetric heterostructures from Section 3.1, the commercial software SimuLase^{TM}, Version 2.0 was used. This software calculates the opto-electric properties of a heterostructure using the **k·p**-theory and the semiconductor Bloch and semiconductor luminescence equations.
Via the graphical user interface at the 'Design Structure'-tab, the user enters the heterostructures layer lengths and compositions. The layers are marked according to their function either as well, barrier or cladding. Further options for the calculations are entered via the 'Generate Database'-tab. Besides specifying the temperatures, sheet carrier densities and inhomogeneous broadenings that should be used, we generally choose the following options:

- √ 'Solve Poisson';
- √ 'Polarization(s): TE';
- √ 'Gain/Absorption', 'Accuracy: High', 'Calculate: Absorption';
- √ 'Model Options: Standard Model' .

The number of electron and hole subbands used during the calculations was entered via choosing 'Sub Bands' and 'Number of Subbands' in combination with entering the corresponding numbers for the electron and hole subbands. These numbers were determined by plotting the wavefunctions and including the maximum number of electron or hole subbands that leads to

wavefunctions that are sufficiently localized in the corresponding well. For this, the option to 'Show: Wavefunctions' in the 'Design Structure'-tab in combination with entering the number of subbands via 'Electron Subbands' and 'Hole Subbands' in the 'Advanced'-tab can be used. Likewise, this can be examined using test-calculations and suitable wavefunction plots.
By choosing the 'Calculate: Absorption' option, the equation of motion for the phonon-assisted polarizations is solved during the calculation of the electron-phonon scattering. In comparison to other options, by choosing 'Model Options: Standard Model' the no phenomenological dephasing times are used to describe the dephasing of the optical polarization by microscopic scattering processes. The band offsets according to [[29]] are used by the program.
For the studies presented in Section 3.1, the bulk band edges[1], single-particle bandstructures (with these the confinement levels are obtained), confinement wavefunctions, absorption spectra and photoluminescence spectra were used from the generated output.

A.2 Non-symmetric heterostructures

For calculations with the non-symmetric structures, C-code and shell scripts which belong to our group were used. The code performs both, the **k·p**-calculations for the heterostructure and the calculation of its optical properties with the semiconductor Bloch and semiconductor luminescence equations. The files are accessible in our group archive. In order to do a specific calculation, the heterostructure's layer length, layer composition as well as the numerical parameters and other options for the calculations were specified in the file input.c. The sheet carrier densities are specified in the file vals.dat. Here, it is assumed that the user uses units of $10^{12}/\mathrm{cm}^2$. After all parameters are set, the program is compiled and executed. In the framework of this thesis, the bulk band edges before and after self-consistently solving the Poisson-problem, single-particle bandstructure (with these the confinement levels are obtained), confinement wavefunctions, dipole matrix elements, and absorption and photoluminescence spectra were used from the generated output.
As stated above, for each heterostructure the numbers of electron and hole subbands that were included in the calculations were determined. This was done with test-calculations and plots of the respective wavefunctions.

[1] Available are the bulk band edges after the self-consistent solution of the Poisson-Problem.

Below, settings that were typically used to calculate the bandstructure and optical spectra of (InGa)As/Ga(AsSb)-heterostructure are given. The presented input.c file belongs to calculations for the studies presented in Section 3.2.

```
#define VERSION 01

extern char clc_filepath[]; char clc_filepath[]="x";
extern char disp_filepath[]; char disp_filepath[]="x";
extern char res_filepath[]; char res_filepath[]="x";

extern double energy_over_s; double energy_over_s=(0.81);
extern double qw_density; double qw_density=2.01;
extern double temperature_l; double temperature_l=10.01;/* lattice
temperature [K] */
extern double temperature_c; double temperature_c=10.01;/* carrier
temperature [K] */
extern double field[]; double field[]={0.0e51};
extern double dephase_2; double dephase_2=1.01;
extern double total_time; double total_time=6.0e-121;
extern double kpar_maxini; double kpar_maxini=20.01; /* maximum
k_parallel value; in k_Bohr = 2pi/a0; a0 : Bohr radius */
extern long int tetmpol; long int tetmpol=0; /* light polarization;
0: TE, 1: TM */
#define ZB_OR_WZ 01 /* crystal structure; 0: zincblende, 1: wurtzite */
#define WZ_CBVB 01
#define CALC_SE 11 /* 0: for absorption, 1: for PL and absorption */
#define INCLUDE_EX_SOURCE 11
#define N_LEVEL 01
#define Bi_LEVEL 01

#define TWO_P_THREE 01
#if( TWO_P_THREE )
 #define NO_WELLC_TWO 31
 #define NO_WELLH_TWO 81
 #if( N_LEVEL )
  #define NO_WELLC_THREE 21
 #elif( Bi_LEVEL )
  #define NO_WELLC_THREE 11
 #else
```

```
  #define NO_WELLC_THREE 1l
 #endif
 #if( Bi_LEVEL )
  #define NO_WELLH_THREE 3l
 #else
  #define NO_WELLH_THREE 3l
 #endif
 #define NO_WELLC (NO_WELLC_TWO+NO_WELLC_THREE)
 #define NO_WELLHH (NO_WELLH_TWO+NO_WELLH_THREE)
 #define FT_NODES_THREE 1l
#else
 #define NO_WELLC 2l /* number of subbands for electrons */
 #define NO_WELLHH 6l /* number of subbands for holes */
 #define NO_WELLC_TWO NO_WELLC
 #define NO_WELLH_TWO NO_WELLHH
 #define NO_WELLC_THREE (0l)
 #define NO_WELLH_THREE (0l)
#endif

#define NO_OF_KPAR 100l
#define NOOFT 30011l
#define POISSON 1l
#define MODEL 4l
#define PHON_SCATT 1l
#define ELEL_SCATT 1l
#define USE_LOWEST 0l
#define FT_NODES 265l /* number of nodes for the z and k_z grids,
must be an integer power of two */
#define KZ_PER_NODE 8l
#define GROW 0l
#define STRAIN 1l
#define SYMM_STRUCT 0l
#define SELF_CONS_MU 0l
#define OZ_OR_OO 1l
#define INCLUDE_COULOMB_INTERACTION 1l
#define K_FOURTH 0l
#define WAVEFCTN_PARTS 1l
#define IMPURITY_STATES_UNOCCUPIED 1l

extern long int big_poissonctrl;long int big_poissonctrl=8;
```

```
extern long int poisson_swon;long int poisson_swon=5;

/* material codes: 1 GaAs, 2 GaP, 3 AlAs, 4 AlP, 5 InAs, 6 InP,
7 GaSb, 8 AlN, 9 GaN, 10 InN, 11 InSb, 12 AlSb */
#define STRUCTURE 91 /* number of layers */
extern long int compound_type1[];extern long int compound_type2[];
extern long int compound_type3[];extern long int compound_type4[];
extern long int pot_slope_type[];
extern long int nary[];
extern double layer_lengths[];
extern long int type_of_layer[];
extern double layer_concentl1[];extern double layer_concentl2[];
extern double layer_concentr1[];extern double layer_concentr2[];
extern double n_konz[];extern long int n_in_layer[];
extern double Bi_konz[];
extern double band_offset[];extern double band_offset_l[];
extern double type2_off[];
/* the following four arrays define the elements in the
n-nary material systems;
the material types in columns i are in layer i */
long int compound_type1[]={1,2,1,7,1,5,1,2,1};
long int compound_type2[]={0,1,0,1,0,1,0,1,0};
long int compound_type3[]={0,0,0,0,0,0,0,0,0};
long int compound_type4[]={0,0,0,0,0,0,0,0,0};
/* from the arrays it follows:
GaAs,Ga(AsP), Ga(AsSb), GaAs, (InGa)As, GaAs, Ga(AsP), GaAs */
long int nary[]={2,3,2,3,2,3,2,3,2}; /* number of elements
in layer i */
long int pot_slope_type[]={1,1,1,1,1,1,1,1,1}; /* 1: abrupt potential
jumps, 2: linear potential slope between layers */
long int type_of_layer[]={1,2,2,2,2,2,2,2,1}; /* 2: well,
1: barrier */
extern int strain_to[];int strain_to[]={0,1,1,1,1,1,1,1,1}; /* all
layers are strained to the first one */
double layer_lengths[]=
 {2.3e-9l,19.3e-9l,4.6e-9l,7.7e-9l,1.0e-9l,7.7e-9l,
  4.6e-9l,19.3e-9l,2.3e-9l};
 /* above: 2.3 nm GaAs, 19.3 nm Ga(AsP), 4.6 nm GaAs,
    7.7 nm Ga(AsSb), 1.0 nm GaAs, 7.7 nm (InGa)As, 4.6 nm GaAs,
    19.3 nm Ga(AsP), 2.3 nm GaAs */
```

```
double n_konz[]={0.0l,0.0l,0.0l,0.0l,0.0l,0.0l,0.0l,0.0l,0.0l};
long int n_in_layer[]={0,0,0,0,0,0,0,0,0};
double Bi_konz[]={0.0l,0.0l,0.0l,0.0l,0.0l,0.0l,0.0l,0.0l,0.0l};
double layer_concentl1[]=
 {0.0l,0.054l,0.0l,0.033l,0.0l,0.058l,0.0l,0.054l,0.0l}; /* 5.4% P,
    3.3% Sb, 5.8% In, 5.4% P */
double layer_concentr1[]=
 {0.0l,0.054l,0.0l,0.033l,0.0l,0.058l,0.0l,0.054l,0.0l};
double layer_concentl2[]=
 {0.0l,0.0l,0.0l,0.0l,0.0l,0.0l,0.0l,0.0l,0.0l};
double layer_concentr2[]=
 {0.0l,0.0l,0.0l,0.0l,0.0l,0.0l,0.0l,0.0l,0.0l};
double band_offset[]=
 {0.6042l,0.6042l,0.1411l,0.1411l,0.6339l,0.6339l,0.6042l,0.6042l};
 /* above: fraction of the bandgap difference that is assigned to
    the conduction band offset between adjacent layers */
double band_offset_l[]={0.0l,0.0l};
double type2_off[]={0.0l,0.0l,0.0l};

#if( TWO_P_THREE )
 extern long int bulk_layer_no;
 long int bulk_layer_no=0l;
#endif
```

Generally, for the calculations, the layers next to the wells are marked as wells instead of as barriers. This is done in order to carry out quantized calculations for this layers as well. The first and the last layers are marked as barriers. In practice, the specification of a layer either as well- or barrier-material is done by entering 2 (for well) or 1 (for barrier) in the array type_of_layer[]. Here, column i belongs to layer i. When declaring a multinary compound, the order of binary semiconductors in the columns of the arrays long int compound_typeM[] (where M$\in \{1,2,3,4\}$) can generally not be arbitrary. Valid input can be derived by examining the function:

double parameter_e_c[4][((long int)STRUCTURE)], double conc1, double conc2),

which can be found in the file kpparame_2010−05.c. This function calculates the unstrained bandgaps. Here, the bandgap calculations are generally not implemented for all possible orders of elements in a compound. This

function was also used to adjust the bandgaps that were used for calculations in the studies presented in Section 3.2. For this purpose, the bandgap calculation in the conditional statement of:

```
else if( compound_type1[layer]==7 && compound_type2[layer]==1 )
```

was replaced.

For the (InGa)As, Ga(AsSb) and GaAs based heterostructures from Section 4.1, using #define FT_NODES 128l was sufficient. Except for this, the same numerical parameters were used in input.c. In this study, the bandgaps were not varied.

A.3 VBO calculations with DFT

For the DFT calculations, VASP 5.4.4 was used. In order to model pseudomorphically grown materials an adjusted version of VASP 5.4.4 was used during the relaxation calculations. This z-relaxation version allows only for changes of the lattice constant in z-direction, while the lattice constants perpendicular to the z-direction remain unchanged. The VASP z-relaxation version was compiled with an adjusted constr_cell_relax.F file. In this file, all components of the matrix that contains the forces on the supercell (the respective matrix is called FCELL) were set to zero except for the z-component on the diagonal of the matrix.
The calculations from Section 4.2.1 were carried out using Python-code which belongs to our research group and was programmed by J. O. Oelerich. This code enables an efficient set up of VASP calculations. It uses different functions from the *Atomic Simulation Environment* [[82]] code and generates special quasi-random structures using the mcsqs-code from the *Alloy Theoretic Automated Toolkit* [[75]]. The code is accessible in our group archive.
Below, generally used settings in the INCAR-files during relaxation and electronic structure calculations are given. Information on the used cell sizes and and the corresponding KPOINTS-files can be found in Section 4.2.1. These INCAR-files were automatically generated with the above mentioned Python-code, to which the user-input was passed.

```
INCAR for relaxation calculations
 ENCUT = 367.498300
 EDIFF = 1.00e-04
 EDIFFG = -2.00e-02
 SIGMA = 0.050000
```

```
 POTIM = 0.500000
 AMIN = 0.010000
 GGA = PS
 ALGO = fast
 PREC = normal
 NSW = 150
 IBRION = 1
 NELM = 250
 ISYM = 1
 ISIF = 3
 ISMEAR = 0
 NFREE = 10
 ADDGRID = .TRUE.
 LREAL = Auto

INCAR for electronic structure calculations
 ENCUT = 367.498300
 EDIFF = 1.00e-04
 SIGMA = 0.050000
 AMIN = 0.010000
 GGA = PS
 ALGO = fast
 PREC = normal
 ISTART = 0
 NELM = 250
 ISYM = -1
 ISMEAR = 0
 ICHARG = 2
 LMAXMIX = 4
 ICORELEVEL = 1
 LVHAR = .TRUE.
 LSORBIT = .TRUE.
 LVTOT = .TRUE.
 LREAL = Auto
```

Depending on the cluster on which the calculations were carried out, different setting for NPAR or NCORE were used.

Bibliography

[1] E. Murphy, "Enabling optical communication", Nature Photonics **4**, 287–287 (2010).

[2] J. R. Meyer, C. L. Felix, W. W. Bewley, I. Vurgaftman, E. H. Aifer, L. J. Olafsen, J. R. Lindle, C. A. Hoffman, M.-J. Yang, B. R. Bennett, B. V. Shanabrook, H. Lee, C.-H. Lin, S. S. Pei, and R. H. Miles, "Auger coefficients in type-II InAs/$Ga_{1-x}In_xSb$ quantum wells", Applied Physics Letters **73**, 2857–2859 (1998).

[3] J. R. Meyer, C. A. Hoffman, F. J. Bartoli, and L. R. Ram-Mohan, "Type-II quantum-well lasers for the mid-wavelength infrared", Applied Physics Letters **67**, 757–759 (1995).

[4] C. Fuchs, A. Brüggemann, M. J. Weseloh, C. Berger, C. Möller, S. Reinhard, J. Hader, J. V. Moloney, A. Bäumner, S. W. Koch, and W. Stolz, "High-temperature operation of electrical injection type-II (GaIn)As/Ga(AsSb)/(GaIn)As "W"-quantum well lasers emitting at 1.3 µm", Scientific Reports **8**, 1422 (2018).

[5] L. G. Ferreira, M. Marques, and L. K. Teles, "Approximation to density functional theory for the calculation of band gaps of semiconductors", Physical Review B **78**, 125116 (2008).

[6] K.-H. Xue, J.-H. Yuan, L. R. Fonseca, and X.-S. Miao, "Improved LDA-1/2 method for band structure calculations in covalent semiconductors", Computational Materials Science **153**, 493–505 (2018).

[7] C. M. Jones and E. Kioupakis, "Effect of strain on band alignment of GaAsSb/GaAs quantum wells", Journal of Applied Physics **122**, 045703 (2017).

[8] J. C. Slater and K. H. Johnson, "Self-Consistent-Field Xα Cluster Method for Polyatomic Molecules and Solids", Physical Review B **5**, 844–853 (1972).

[9] C. Fuchs, C. Berger, C. Möller, M. Weseloh, S. Reinhard, J. Hader, J. V. Moloney, S. W. Koch, and W. Stolz, "Electrical injection type-II (GaIn)As/Ga(AsSb)/(GaIn)As single "W"-quantum well laser at 1.2 µm", English, Electronics Letters **52**, 1875–1877(2) (2016).

[10] M. Stein, C. Lammers, P.-H. Richter, C. Fuchs, W. Stolz, M. Koch, O. Vänskä, M. J. Weseloh, M. Kira, and S. W. Koch, "Dynamics of charge-transfer excitons in type-II semiconductor heterostructures", Physical Review B **97**, 125306 (2018).

[11] S. Gies, M. J. Weseloh, C. Fuchs, W. Stolz, J. Hader, J. V. Moloney, S. W. Koch, and W. Heimbrodt, "Band offset in (Ga,In)As/Ga(As,Sb) heterostructures", Journal of Applied Physics **120**, 204303 (2016).

[12] J. O. Oelerich, M. J. Weseloh, K. Volz, and S. W. Koch, "*Ab-initio* calculation of band alignments for opto-electronic simulations", AIP Advances **9**, 055328 (2019).

[13] M. J. Weseloh, J. O. Oelerich, and S. W. Koch, "Half-occupation approach for the *ab initio* calculation of strained Ga(AsSb)/GaAs valence band offsets", AIP Advances **10**, 045207 (2020).

[14] J. F. Klem, O. Blum, S. R. Kurtz, I. J. Fritz, and K. D. Choquette, "GaAsSb/InGaAs type-II quantum wells for long-wavelength lasers on GaAs substrates", Journal of Vacuum Science & Technology B: Microelectronics and Nanometer Structures Processing, Measurement, and Phenomena **18**, 1605–1608 (2000).

[15] M. Kira and S. W. Koch, "Many-body correlations and excitonic effects in semiconductor spectroscopy", Progress in Quantum Electronics **30**, 155–296 (2006).

[16] H. Haug and S. W. Koch, *Quantum Theory of the Optical and Electronic Properties of Semiconductors, fifth edition* (World Scientific Publishing Co., Jan. 2009).

[17] F. Bloch, "Über die Quantenmechanik der Elektronen in Kristallgittern", Zeitschrift für Physik (1929) **52**, 555–600.

[18] E. Wigner and F. Seitz, "On the Constitution of Metallic Sodium", Physical Review **43**, 804–810 (1933).

[19] J. C. Slater and G. F. Koster, "Simplified LCAO Method for the Periodic Potential Problem", Physical Review **94**, 1498–1524 (1954).

[20] P. Y. Yu and M. Cordona, *Fundamentals of Semiconductors* (Springer-Verlag Berlin Heidelberg, 2010).

[21] J. M. Luttinger, "Quantum Theory of Cyclotron Resonance in Semiconductors: General Theory", Physical Review **102**, 1030–1041 (1956).

[22] J. Hader, N. Linder, and G. H. Döhler, "**k**·**p** theory of the Franz-Keldysh effect", Physical Review B **55**, 6960–6974 (1997).

[23] P. Löwdin, "A Note on the Quantum-Mechanical Perturbation Theory", The Journal of Chemical Physics **19**, 1396–1401 (1951).

[24] G. Bastard, *Wave Mechanics Applied to Semiconductor Heterostructures* (Les Éditions de Physique, Les Ulis Cedex, France, 1988).

[25] R. Winkler and U. Rössler, "General approach to the envelope-function approximation based on a quadrature method", Physical Review B **48**, 8918–8927 (1993).

[26] G. E. Pikus and G. L. Bir, "Effect of deformation on the hole energy spectrum of germanium and silicon", Soviet Physics - Solid State (1960).

[27] W. W. Chow and S. W. Koch, *Semiconductor-Laser Fundamentals* (Springer-Verlag Berlin Heidelberg, 1999).

[28] Y. P. Varshni, "Temperature dependence of the energy gap in semiconductors", Physica **34**, 149 –154 (1967).

[29] I. Vurgaftman, J. R. Meyer, and L. R. Ram-Mohan, "Band parameters for III-V compound semiconductors and their alloys", Journal of Applied Physics **89**, 5815–5875 (2001).

[30] D. Ahn and S. L. Chuang, "Model of the field-effect quantum-well laser with free-carrier screening and valence band mixing", Journal of Applied Physics **64**, 6143–6149 (1988).

[31] K. O. Jensen, "Local density calculation of positron annihilation in metals", Journal of Physics: Condensed Matter **1**, 10595–10602 (1989).

[32] S. K. Saha, U. V. Waghmare, H. R. Krishnamurthy, and A. K. Sood, "Phonons in few-layer graphene and interplanar interaction: A first-principles study", Physical Review B **78**, 165421 (2008).

[33] D. R. Hamann, "Generalized Gradient Theory for Silica Phase Transitions", Physical Review Letters **76**, 660–663 (1996).

[34] P. Hohenberg and W. Kohn, "Inhomogeneous Electron Gas", Physical Review **136**, B864–B871 (1964).

[35] W. Kohn and L. J. Sham, "Self-Consistent Equations Including Exchange and Correlation Effects", Physical Review **140**, A1133–A1138 (1965).

[36] C. Fiolhais, F. Nogueira, and M. A. L. Marques, eds., *A Primer in Density Functional Theory* (Springer-Verlag Berlin Heidelberg, 2003).

[37] J. P. Perdew, K. Burke, and M. Ernzerhof, "Generalized Gradient Approximation Made Simple", Physical Review Letters **77**, 3865–3868 (1996).

[38] A. D. Becke, "A new mixing of Hartree–Fock and local density-functional theories", The Journal of Chemical Physics **98**, 1372–1377 (1993).

[39] M. S. Miao, P. E. Van Camp, V. E. Van Doren, J. J. Ladik, and J. W. Mintmire, "An LDA calculation of the conformation and electronic structure of polytetrafluoroethylene", International Journal of Quantum Chemistry **64**, 243–246 (1997).

[40] A. Marini, G. Onida, and R. Del Sole, "Plane-wave DFT-LDA calculation of the electronic structure and absorption spectrum of copper", Physical Review B **64**, 195125 (2001).

[41] A. van de Walle and G. Ceder, "Correcting overbinding in local-density-approximation calculations", Physical Review B **59**, 14992–15001 (1999).

[42] J. P. Perdew, "Density functional theory and the band gap problem", International Journal of Quantum Chemistry **28**, 497–523 (1985).

[43] D. C. Langreth and M. J. Mehl, "Beyond the local-density approximation in calculations of ground-state electronic properties", Physical Review B **28**, 1809–1834 (1983).

[44] J. P. Perdew, A. Ruzsinszky, G. I. Csonka, O. A. Vydrov, G. E. Scuseria, L. A. Constantin, X. Zhou, and K. Burke, "Restoring the Density-Gradient Expansion for Exchange in Solids and Surfaces", Physical Review Letters **100**, 136406 (2008).

[45] J. F. Janak, "Proof that $\frac{\partial E}{\partial n_i} = \epsilon$ in density-functional theory", Physical Review B **18**, 7165–7168 (1978).

[46] L. G. Ferreira, M. Marques, and L. K. Teles, "Slater half-occupation technique revisited: the LDA-1/2 and GGA-1/2 approaches for atomic ionization energies and band gaps in semiconductors", AIP Advances **1**, 032119 (2011).

[47] `https://departments.icmab.es/leem/siesta/Pseudopotentials/Code/downloads.html`, Accessed: 2019-09.

[48] C. Schlichenmaier, "Modeling of Optical Properties of Semiconductor Heterostructures", Dissertation (Philipps-Universität Marburg, 2005).

[49] J. Hader, S. Koch, and J. Moloney, "Microscopic theory of gain and spontaneous emission in GaInNAs laser material", Solid-State Electronics **47**, 513 –521 (2003).

[50] B. Pasenow, "Optische Erzeugung außergewöhnlicher Ladungsträgerverteilungen in Halbleiterstrukturen", Dissertation (Philipps-Universität Marburg, 2006).

[51] G. Kresse and J. Hafner, "*Ab initio* molecular dynamics for liquid metals", Physical Review B **47**, 558–561 (1993).

[52] G. Kresse and J. Hafner, "*Ab initio* molecular-dynamics simulation of the liquid-metal–amorphous-semiconductor transition in germanium", Physical Review B **49**, 14251–14269 (1994).

[53] G. Kresse and J. Furthmüller, "Efficiency of *ab-initio* total energy calculations for metals and semiconductors using a plane-wave basis set", Computational Materials Science **6**, 15 –50 (1996).

[54] G. Kresse and J. Furthmüller, "Efficient iterative schemes for ab initio total-energy calculations using a plane-wave basis set", Physical Review B **54**, 11169–11186 (1996).

[55] P. E. Blöchl, "Projector augmented-wave method", Physical Review B **50**, 17953–17979 (1994).

[56] G. Kresse and D. Joubert, "From ultrasoft pseudopotentials to the projector augmented-wave method", Physical Review B **59**, 1758–1775 (1999).

[57] J. A. Zuclich, D. J. Lund, and B. E. Stuck, "Wavelength dependence of ocular damage thresholds in the near-ir to far-ir transition region: proposed revisions to MPES", Health Physics **92**, 15–23 (2007).

[58] D. O. Caplan, "Laser communication transmitter and receiver design", Journal of Optical and Fiber Communications Reports **4**, 225–362 (2007).

[59] K. Mathur, *Fundamentals of Fiber Optics Communications* (ZORBA Books, 2018).

[60] J. Hader, J. V. Moloney, and S. W. Koch, "Microscopic evaluation of spontaneous emission- and auger-processes in semiconductor lasers", IEEE Journal of Quantum Electronics **41**, 1217–1226 (2005).

[61] B. N. Zvonkov, N. S.M., V. O.V., and D. N.V., "Emission properties of heterostructures with a (GaAsSb-InGaAs)/GaAs bilayer quantum well", Semiconductors **47**, 1219–1223 (2013).

[62] M. Kuznetsov, "VECSEL Semiconductor Lasers: A Path to High-Power, Quality Beam and UV to IR Wavelength by Design", in *Semiconductor disk lasers* (John Wiley & Sons, Ltd, 2010) Chap. 1, pp. 1–71.

[63] C. Berger, "Microscopic Theory of Semiconductor Laser Material Systems", Dissertation (Philipps-Universität Marburg, 2016).

[64] X. He and S. Srinivasan, *Quantum well laser with a composition-graded interface at the quantum-well*, United States Patent, Patent Number: 6,091,752, 2000.

[65] J.-B. Wang, S. R. Johnson, S. A. Chaparro, D. Ding, Y. Cao, Y. G. Sadofyev, Y.-H. Zhang, J. A. Gupta, and C. Z. Guo, "Band edge alignment of pseudomorphic $GaAs_{1-y}Sb_y$ on GaAs", Physical Review B **70**, 195339 (2004).

[66] S. R. Johnson, S. Chaparro, J. Wang, N. Samal, Y. Cao, Z. B. Chen, C. Navarro, J. Xu, S. Q. Yu, D. J. Smith, C.-Z. Guo, P. Dowd, W. Braun, and Y.-H. Zhang, "GaAs-substrate-based long-wave active materials with type-II band alignments", Journal of Vacuum Science & Technology B: Microelectronics and Nanometer Structures Processing, Measurement, and Phenomena **19**, 1501–1504 (2001).

[67] C. E. Pryor and M.-E. Pistol, "Band-edge diagrams for strained III–V semiconductor quantum wells, wires, and dots", Physical Review B **72**, 205311 (2005).

[68] S. Gies, B. Holz, C. Fuchs, W. Stolz, and W. Heimbrodt, "Recombination dynamics of type-II excitons in (Ga,In)As/GaAs/Ga(As,Sb) heterostructures", Nanotechnology **28**, 025701 (2016).

[69] C. G. Van De Walle and J. Neugebauer, "Universal alignment of hydrogen levels in semiconductors, insulators and solutions", Nature, 626–628 (2003).

[70] J. M. Bass, M. Oloumi, and C. C. Matthai, "A method for determining band offsets in semiconductor superlattices and interfaces", Journal of Physics: Condensed Matter **1**, 10625–10628 (1989).

[71] S. H. Wei and A. Zunger, "Calculated natural band offsets of all II-VI and III-V semiconductors: chemical trends and the role of cation d orbitals", Applied Physics Letters **72**, 2011–2013 (1998).

[72] M. S. Hybertsen and S. G. Louie, "First-Principles Theory of Quasiparticles: Calculation of Band Gaps in Semiconductors and Insulators", Physical Review Letters **55**, 1418–1421 (1985).

[73] A. Baldereschi, S. Baroni, and R. Resta, "Band Offsets in Lattice-Matched Heterojunctions: A Model and First-Principles Calculations for GaAs/AlAs", Physical Review Letters **61**, 734–737 (1988).

[74] S.-H. Wei, L. G. Ferreira, J. E. Bernard, and A. Zunger, "Electronic properties of random alloys: Special quasirandom structures", Physical Review B **42**, 9622–9649 (1990).

[75] A. van de Walle, P. Tiwary, M. de Jong, D. Olmsted, M. Asta, A. Dick, D. Shin, Y. Wang, L.-Q. Chen, and Z.-K. Liu, "Efficient stochastic generation of special quasirandom structures", Calphad **42**, 13 –18 (2013).

[76] H. J. Monkhorst and J. D. Pack, "Special points for Brillouin-zone integrations", Physical Review B **13**, 5188–5192 (1976).

[77] G. Merad, H. Aourag, and B. Khelifa, "The valence and conduction band edges charge densities under high pressure for GaSb", Physica Scripta **45**, 454–457 (1992).

[78] D. Benson, O. F. Sankey, and U. Häussermann, "Electronic structure and chemical bonding of the electron-poor II-V semiconductors ZnSb and ZnAs", Physical Review B **84**, 125211 (2011).

[79] S.-W. Ryu and P. D. Dapkus, "Optical characterization and determination of conduction band offset of type-II GaAsSb/InGaAs QW", Semiconductor Science and Technology **19**, 1369–1372 (2004).

[80] C. A. Broderick, S. Jin, I. P. Marko, K. Hild, P. Ludewig, Z. L. Bushell, W. Stolz, J. M. Rorison, E. P. O'Reilly, K. Volz, and S. Sweeney, "$GaAs_{1-x}Bi_x/GaN_yAs_{1-y}$ type-II quantum wells: novel strain-balanced heterostructures for GaAs-based near- and mid-infrared photonics", Scientific Reports **7**, 46371 (2017).

[81] B. Chen, "Optical gain analysis of GaAs-based InGaAs/GaAsSbBi type-II quantum wells lasers", Optics Express **25**, 25183–25192 (2017).

[82] A. H. Larsen, J. J. Mortensen, J. Blomqvist, I. E. Castelli, R. Christensen, M. Dułak, J. Friis, M. N. Groves, B. Hammer, C. Hargus, E. D. Hermes, P. C. Jennings, P. B. Jensen, J. Kermode, J. R. Kitchin, E. L. Kolsbjerg, J. Kubal, K. Kaasbjerg, S. Lysgaard, J. B. Maronsson, T. Maxson, T. Olsen, L. Pastewka, A. Peterson, C. Rostgaard, J. Schiøtz, O. Schütt, M. Strange, K. S. Thygesen, T. Vegge, L. Vilhelmsen, M. Walter, Z. Zeng, and K. W. Jacobsen, "The atomic simulation environment—a Python library for working with atoms", Journal of Physics: Cond. Mat. **29**, 273002 (2017).